

DISSERTATION

ACTION POTENTIAL INITIATION MECHANISMS: ANALYSIS AND NUMERICAL
STUDY

Submitted by

Ahmed A. Aldohbeyb

School of Biomedical Engineering

In partial fulfillment of the requirements

For the Degree of Doctor of Philosophy

Colorado State University

Fort Collins, Colorado

Spring 2022

Doctoral Committee:

Advisor: Kevin L. Lear

Jozsef Vigh

Ashok Prasad

Karan Venayagamoorthy

Copyright by Ahmed A. Aldohbeyb 2022

All Rights Reserved

ABSTRACT

ACTION POTENTIAL INITIATION MECHANISMS: ANALYSIS AND NUMERICAL STUDY

Action potentials (AP) are the unitary elements of information processing in the nervous system. Understanding AP initiation mechanisms is a fundamental step in determining how neurons encode information. However, variation in neuronal response is a characteristic of mammalian neurons, which further complicate the analysis of neuronal firing dynamics. Several studies have associated the variation in AP onset with the type and densities of voltage-gated ion channels, diversity in synaptic inputs, neuron intrinsic properties, cooperative Na⁺ gating, or AP backpropagation. But the mechanisms that underlie the response variability remain unclear and subject to debate. Even though all these studies tried to answer the same question, the definition of AP onset and rapidity differs between them, highlighting the need for a more systematic and consistent method to quantify AP onset features, and hence analyzing the variation in AP onset.

Two novel methods were developed to quantify AP rapidity. The proposed methods have lower relative variation, higher ability to classify neuron types, and higher sensitivity and specificity to voltage-gated Na⁺ channels parameters than current methods. AP rapidity was used to analyze different factors impacting the AP activation mechanism. However, the prior rapidity quantification methods are subjectively based on the researcher's judgment, which complicates the comparison between different studies. Thus, we proposed a more systematic and consistent method based on the full-width or half-width at half the rising phase peak of the membrane potential's second-time derivative (\ddot{V}_m). First, using an HH-type model, we showed that the peak width methods are sensitive to changes in the Na⁺ channel parameters and conductance and minimally impacted by changes in the K⁺ channel parameters compared to the phase slope, the standard quantification method. Second, we compared the peak width methods to the two prior

methods, phase slope and error ratio, using recordings from cortical and hippocampal pyramidal neurons, hippocampal PVBCs, and FS cortical neurons found in online databases. The results showed that the new methods have the lowest variation between neurons within a specific type while significantly differentiating several neuron types. Together, the two studies showed that the peak width methods provide another sensitive tool to investigate the mechanisms impacting AP onset dynamics and provide a better tool to study Na^+ channels kinetics and AP onset features.

A conductance-based model that includes dynamics of ion concentration and cooperative Na^+ channels was developed to investigate the mechanisms responsible for observed neuronal response variation. Random response variability has previously been observed in spike trains evoked from individual neurons by the same DC stimulus, but we observed systematic variation. The first APs' in a burst had attributes that were comparable regardless of the stimulus strength, while the subsequent APs' attributes monotonically change during bursts, and the magnitude of change increases with stimulus strength. These two spike train features were observed in three different neuron types ($n = 51$), indicating a shared mechanism is responsible for the spike train pattern. Various existing computational models fail to replicate the monotonic variation in AP attributes. We proposed incorporating ion concentration dynamics and cooperative gating to account for the missing behavior. A model with dynamic reversal potential but without cooperative Na^+ channel gating reproduces the AP attribute's variation during bursts, but not the first APs' attributes. The first APs' attributes were reproduced only in the presence of a fraction of cooperative Na^+ channels. Cooperative gating also enhanced the magnitude of modeled variation of some AP attributes to better match the electrophysiological recordings. Therefore, we conclude that changes in ion concentration dynamics could be responsible for the monotonic change in some AP's attributes during normal neuronal firing, and cooperative gating can enhance this effect. Thus, the two mechanisms contribute to the observed variability in neuronal response, especially the variation in AP rapidity.

ACKNOWLEDGMENTS

I would like to express my sincere gratitude to Dr. Kevin Lear for giving me the opportunity to work with him, for his patience, guidance, encouragement, and support, invaluable help of constructive comments and suggestion without which this dissertation would not be completed. I would like to thank Dr. Jozsef Vigh for introducing me to the world of neuroscience and for his invaluable insight and advice through my PhD journey. Also, I would like to thank my other committee members, Dr. Ashok Prasad and Dr. Karan Venayagamoorthy, for their assistance and help.

I would like to thank my father, my mother, and all my family members for their continuous support. I would never be here without their encouragement and support. I extend my sincere thanks to my wife, Lamar Alnughmishi, and my son, Malik, for the endless efforts and support during my study, and for enduring a busy husband/father. I'm thankful to them for their patience, support, and motivation.

Finally, I would like to thank the Saudi government and King Saud University for their financial support and cooperation for giving me the privilege of pursuing a PhD degree in Biomedical Engineering at Colorado State University.

TABLE OF CONTENTS

ABSTRACT	ii
ACKNOWLEDGMENTS	iv
LIST OF TABLES	ix
LIST OF FIGURES	x
1 INTRODUCTION	1
1.1 MOTIVATION	1
1.2 DISSERTATION ORGANIZATION	4
2 LITERATURE REVIEW	5
2.1 GENERAL VIEW OF ACTION POTENTIAL INITIATION	5
2.2 Na⁺ channels inactivation mechanism	7
2.3 Na⁺ channel activation mechanisms	8
2.4 Ion concentration dynamics in neurons	11
2.5 Models of cooperative Na⁺ channel gating	12
Naundorf et al. model [2]	13
Huang et al. model [5].....	14
Öz et al. model [6].....	15
3 NEW METHOD TO ANALYZE THE RAPIDITY OF ACTION POTENTIAL INITIATION	17
3.1 Introduction	18
3.2 Methods	20
Data Source for AP Recordings	20
Quantification of the Rapidity of the AP onset	21
HH model for cortical neurons.....	22
3.3 Results	24

Measuring the impact of α_i and β_i parameters on the rapidity of AP onset.....	24
The rapidity of AP onset in recorded primary somatosensory cortical neurons	28
3.4 Discussion.....	32
Variation of HH α_i and β_i parameters to assess the quantification methods	32
Advantages of the FWHM and HWHM methods	33
3.5 Conclusions.....	34
4 NEW METHODS FOR QUANTIFYING RAPIDITY OF ACTION POTENTIAL ONSET DIFFERENTIATE NEURON TYPES.....	35
4.1 Introduction.....	36
4.2 Methods.....	38
Data source for AP recordings	38
Quantification of rapidity of AP onset	40
Other AP parameters	42
Statistical analysis	42
4.3 Results	43
Comparison between the AP rapidity quantification methods.....	43
Impact of sampling rate and interpolation method.....	47
Impact of phase slope criterion level.....	49
Impact of data selection limits on error ratio method	51
Classification of neuron types based on AP rapidity	52
4.4 Discussion.....	56
The AP rapidity quantification methods	57
Factors affecting AP onset rapidity	58
The second derivative peak width methods for neuron classification	60
Sodium channel parameters affect modeled rapidity	62
4.5 Conclusions.....	63
5 THE IMPACT OF DYNAMIC REVERSAL POTENTIAL AND COOPERATIVITY ON THE EVOLUTION OF RAPIDITY AND OTHER ACTION POTENTIAL ATTRIBUTES DURING SPIKE TRAINS	65
5.1 Introduction.....	66
5.2 Methods.....	70
AP parameters	70
Data source for AP recordings	70

Computational models.....	71
5.3 Results	75
Neurons alter AP parameters during continuous firing.....	75
Ion concentration changes dictate monotonic variation in AP attribute	78
Cooperativity and DPR replicates the spike patterns observed in intracellular recordings	82
Cell volume and pump strength effect on AP attributes	84
5.4 Discussions	87
Factors influencing neuronal variability	88
Ion concentration impact on spike train is enhanced with cooperative gating.....	89
5.5 Conclusions.....	90
6 CONCLUSIONS	91
6.1 Two novel methods for AP rapidity quantification methods.....	91
6.2 AP rapidity as a tool to classify neuron types.....	92
6.3 Mechanisms underlying AP variation in intracellular recordings.....	93
6.4 Future works	95
AP rapidity measured at the single-channel level	95
Improvement in Na ⁺ concentration modeling	96
Cooperativity model that accounts for channels spacing and their influence on conduction velocity	97
REFERENCES.....	98
APPENDIX A: SUPPORTING INFORMATION FOR NEURON CLASSIFICATION (PUBLISHED).....	107
APPENDIX B: SUPPORTING INFORMATION FOR NEURON CLASSIFICATION (NOT PUBLISHED)	111
Error ratio Quantification	111
Impact of the data selection on the error ratio.....	112
Differences among hippocampal pyramidal neurons.....	114
AP onset potential quantification methods.....	115
Outliers' detection methods	117
Relationship between the <i>V</i> peak width and the integrated area.....	119
Hippocampal Interneurons.....	121
Differences in onset rapidity between CA1 hippocampal interneurons.....	125

APPENDIX C: SUPPORTING INFORMATION FOR SPIKE TRAIN PATTERNS (INTEND TO PUBLISH)	127
APPENDIX D: COMPARISON AND ANALYSIS OF THE MODELS USED TO REPLICATE SPIKE TRAIN PATTERNS	130
Cooperative gating increases AP onset rapidity	130
Ion concentration impact with weak stimulus	136
The combined effect of cooperativity and ion concentration on average AP parameters.....	138
APPENDIX E: MATLAB CODES	142
AP extraction and interpolation code	144
AP analysis code	145
The combined model code	149
APPENDIX F: NUMERICAL ANALYSIS AND DATA SOURCE	158
Electrophysiological recordings sources	160

LIST OF TABLES

TABLE 2.1: COMPARISON BETWEEN THREE COOPERATIVE Na^+ CHANNELS MODELS	12
TABLE 3.1 RATE CONSTANTS EQUATIONS. NOMINAL VALUES FOR A, B, AND C ARE SHOWN AS DESCRIBED IN [79].	23
TABLE 3.2: VALUES CORRESPONDING TO INCREASING VGSCs	28
TABLE 3.3: VALUES CORRESPONDING TO INCREASING VGKCs	28
TABLE 4.1: ELECTROPHYSIOLOGICAL PROPERTIES USING CONVENTIONAL MEAN AND STANDARD DEVIATION	45
TABLE 4.2: THE MEAN AND STANDARD DEVIATION OF RAPIDITY FOR RS HIPPOCAMPAL NEURONS USING POOLED STATISTICS	49
TABLE 4.3: COMPARISON BETWEEN ELECTROPHYSIOLOGICAL PROPERTIES OF FOUR NEURON TYPES USING CONVENTIONAL STATISTICS	54
TABLE 4.4: COMPARISON BETWEEN SINGLE-COMPONENT AND DOUBLE-COMPONENT APs	56
TABLE 4.5: TWO-TAILED P-VALUE FROM THE T-SCORE BETWEEN THE IFWD ² VALUES FROM DIFFERENT NEURON TYPES, AND COHEN’S D EFFECT SIZE (IN PARENTHESES). GREEN CELLS INDICATE A P-VALUE BELOW 0.05	62
TABLE 5.1: MODEL PARAMETERS AND VALUES	73
TABLE 5.2: AP ATTRIBUTES OF 7 FS CORTICAL NEURONS IN RESPONSE TO 5 CURRENT STEPS (MEAN \pm SD)	77
TABLE 5.3: AP ATTRIBUTES OF 27 RS CORTICAL NEURONS IN RESPONSE TO 5 CURRENT STEPS (MEAN \pm SD).	77
TABLE 5.4: AP ATTRIBUTES OF 17 RS HIPPOCAMPAL NEURONS IN RESPONSE TO 5 CURRENT STEPS (MEAN \pm SD).	78

LIST OF FIGURES

FIGURE 2.1: STATE TRANSITION SCHEME OF THE SINGLE SODIUM CHANNEL MODEL.	14
FIGURE 3.1: COMPARISON BETWEEN AP QUANTIFICATION METHODS..	21
FIGURE 3.2: VARIATION OF AP SHAPE WITH CHANGES IN THE RATE CONSTANTS' PARAMETERS IN THE HH MODEL..	25
FIGURE 3.3: COMPARISON OF THE RAPIDITY QUANTIFICATION METHODS' SENSITIVITY TO CHANGES IN THE α_m AND β_m PARAMETERS.....	26
FIGURE 3.4: COMPARISON OF THE QUANTIFICATION METHODS' SENSITIVITY TO CHANGES IN THE α_h AND β_h PARAMETERS.	26
FIGURE 3.5: COMPARISON OF THE QUANTIFICATION METHODS' SENSITIVITY TO CHANGES IN THE α_n AND β_n PARAMETERS.....	27
FIGURE 3.6: THE AVERAGE AND STANDARD DEVIATION OF THE RAPIDITY OF AP ONSET IN 11 NEURONS.	29
FIGURE 3.7: VARIATION IN NEURONAL RESPONSE BETWEEN INDIVIDUAL NEURONS.....	30
FIGURE 3.8: THE COEFFICIENT OF VARIATION OF THE RAPIDITY OF AP ONSET IN NEURONS	30
FIGURE 3.9: NEURONS EVOKED DIFFERENT AP WAVEFORMS.....	31
FIGURE 4.1: THE AP RAPIDITY QUANTIFICATION METHODS.	41
FIGURE 4.2: THE AP RAPIDITY CALCULATED USING THE FOUR QUANTIFICATION METHODS FOR CORTICAL NEURONS.....	44
FIGURE 4.3: THE AP RAPIDITY CALCULATED USING THE FOUR QUANTIFICATION METHODS FOR HIPPOCAMPAL NEURON.....	46
FIGURE 4.4: COMPARISON OF THE IMPACT OF THE PHASE SLOPE CRITERION LEVEL BETWEEN A HIPPOCAMPAL PYRIMIDAL NEURON AND A HIPPOCAMPAL PVBC.	50
FIGURE 4.5: COMPARISON OF THE ELECTROPHYSIOLOGICAL PROPERTIES OF ALL THE NEURONS ANALYZED IN THIS STUDY.....	61
FIGURE 5.1: CHANGES IN AP ATTRIBUTES FROM WHOLE-CELL INTRACELLULAR RECORDINGS OF A TYPICAL RS AND A TYPICAL FS SOMATOSENSORY CORTICAL NEURON.....	76
FIGURE 5.2: AP ATTRIBUTE EVOLUTION IN SPIKE TRAINS RESULTING FROM DIFFERENT HH-TYPE MODELS.	79
FIGURE 5.3: MEMBRANE POTENTIAL (V) AND REVERSAL POTENTIALS (E_{Na^+} AND E_{K^+}) CHANGE DURING TWO CURRENT PULSES	81
FIGURE 5.4: COMPARISON BETWEEN AP ATTRIBUTES IN DIFFERENT MODELING CONDITIONS AND EXPERIMENTAL RECORDING.....	84
FIGURE 5.5: IMPACT OF THE INTRACELLULAR TO EXTRACELLULAR VOLUME RATIO ON AP THRESHOLD AND RAPIDITY.	85
FIGURE 5.6: IMPACT OF THE Na/K PUMP STRENGTH ON AP THRESHOLD AND RAPIDITY	86
FIGURE 5.7: IMPACT OF THE Na/K PUMP STRENGTH ON ION CONCENTRATIONS AND REVERSAL POTENTIAL.....	86

1 INTRODUCTION

1.1 MOTIVATION

Action potentials (APs) initiation is a key process of neural communication and information encoding. Our understanding of AP generation was shaped by Hodgkin and Huxley's (HH) pioneering work in the giant squid axon [1]. However, APs elicited in central mammalian neurons are sharper than those in the squid giant axon. Such a notable difference was the center of debate in the past two decades. Some studies attributed the sharp AP onset to the location of AP initiation, neuron geometry, dendritic size, while other studies suggested a new theory based on cooperative gating of sodium channels [2]–[7]. Although all these studies tried to answer the same question, the definition of AP rapidity differs across them, complicating the comparison between the results between studies.

In prior literature, the rapidity of AP onset was measured using the phase slope and the error ratio methods. The phase slope is the standard approach which calculates the slope on a phase space plot at a criterion level (ranging from 5 to 70 mV/ms) [2], [7], [8]. The second method is the error ratio method, which was suggested to differentiate between slow and fast AP onset. The error ratio method defines rapidity as the ratio of the mean-square errors for two fitting functions (exponential and piecewise linear fit) of the initial portion of the AP in the phase plot [9]. However, the two existing quantification methods are affected by the researcher's judgment in defining the criterion level or the AP portion selected for fitting. Furthermore, other studies have associated the slope of the rising phase of the membrane potential (V) or the maximum value of the first-time derivative (\dot{V}) to Na^+ channels kinetics [10]–[12]. Nonetheless, these methods could not reveal any significant difference between the kinetics of Na^+ channels activation in different neuron types.

Therefore, the subjectivity of current rapidity quantification methods highlights the need for a more systematic and consistent method to quantify AP rapidity. Furthermore, determining the methods' sensitivity and specificity to Na^+ channels is crucial since the whole debate around the sharp AP onset in cortical neurons was either to support or oppose the cooperative sodium channel opening theory [2], [3]. However, to our knowledge, no prior study has investigated the sensitivity and specificity of the rapidity quantification methods to Na^+ channels, which control the generation of neuron signals.

Individual neurons might generate a variety of responses even to the same stimulus. The variability of neuronal response could reflect several aspects of the variation between neurons of the same type and brain regions, such as the diversity in voltage-gated ion channel types and densities, synaptic inputs, or the neuron's intrinsic properties [13]–[15]. Furthermore, cooperativity between neighboring Na^+ was proposed as a mechanism that accounts for the threshold variation and rapid AP initiation observed in cortical neurons [2]. In recent years, several studies have supported the cooperativity hypothesis [16]–[19]. For instance, one study has found that neighboring Na^+ channels physically interact, consistent with cooperativity theory [17]. Furthermore, Na^+ channels are localized in a cluster at the axon initial segment [20], which is a prerequisite for cooperative gating [21]. Channel clustering and coupled gating also imply that more considerable ion concentration changes occur during neuronal activity. Channel clustering can cause higher changes in local ion concentration during, compared to uniformly distributed channels, and the magnitude of concentration change can increase due to coupled gating. However, although fluctuation in K^+ and Na^+ concentrations were observed in cortical neurons [22]–[25], local accumulation and depletion of ions in the vicinity of ion channels are usually overlooked when modeling normal neuronal electrical behavior. Thus, most computational models treat the

ionic reversal potential as a constant. While such an assumption could be valid in the squid giant axon, its validity in mammalian neurons is subject to debate [26]. These studies together have suggested that mammalian Na^+ channel kinetics might deviate from the canonical HH model, and there is a need to reevaluate the role of Na^+ channel kinetics and ion concentration dynamics in biophysical models.

This dissertation focuses on studying and modeling AP initiation mechanisms in central mammalian neurons. First, two novel methods were proposed to quantify AP rapidity. The two methods measure the full-width (FW) or half-width (HW) of the rising phase of the membrane potential second-time derivative (\ddot{V}), which is well-defined and is not affected by the research judgment. The inverse of the FW (IFWd^2) and HW (IHWd^2) define the rapidity in units of 1/time, which are the units usually used for quantifying AP rapidity. Then, the sensitivity and specificity of AP rapidity methods to Na^+ channel kinetics were analyzed using an HH-type model, showing that the proposed methods are more sensitive and specific to Na^+ channel kinetics compared to the phase slope method. The new methods were used to analyze AP rapidity in intracellular recordings from four neuron types. The IFWd^2 rapidity was less variable within a specific neuron type while significantly differentiating neuron types. Hence, properly quantified AP rapidity can be used as a cell classification parameter. Finally, a single-compartment model was constructed to replicate recurring spike train patterns shown across different neuron types. The attributes of the first spikes in the train have comparable values across different cells despite the stimulus strength. In contrast, the average (or last) AP attributes monotonically change during bursts, and the magnitude of parameters tilt increases with stimulus strength. The proposed single-compartment model successfully replicates these two observed experimental patterns only if dynamical reversal potential was implemented and the effect is enhanced with cooperative Na^+ gating.

1.2 DISSERTATION ORGANIZATION

This dissertation consists of six chapters that include three studies focused on the AP onset dynamic, followed by several appendices. The first chapter is an introductory chapter with two sections, the research motivation and the dissertation organization. The second chapter contains the literature review. The third chapter contains the development and analysis of two novel methods proposed to quantify the rapidity of AP onset. The sensitivity and specificity of the two novel onset rapidity methods to Na⁺ channels kinetics was analyzed and compared to the existing method using the original HH model. The third chapter was published in the *Biomedical Sciences Instrumentation* journal [27]. The fourth chapter contains the analysis and comparison of applying the AP rapidity quantification to publically available electrophysiological recordings from four different mammalian neuron types, where the results were used to classify neuron types. The fourth chapter was published in the *PLOS ONE* journal [28]. Then, a conductance-based model that includes both cooperativity between Na⁺ channels and dynamical reversal potential was constructed in the fifth chapter. The proposed model was used to replicate spike train trends during bursts (the third study). The sixth chapter contains the conclusion of this dissertation and suggests future works. Finally, the appendices contain the supporting information from each study. Appendix A and B contains the supporting information for the second paper. Appendix C and D contains the supporting information for the third paper. Appendix E contains the MATLAB code for the combined model used in the third paper and Appendix F contains the numerical methods used in this dissertation and a table describing various neuroscience databases.

2 LITERATURE REVIEW

2.1 GENERAL VIEW OF ACTION POTENTIAL INITIATION

Voltage-gated ion channels (VGICs) are transmembrane proteins responsible for neuronal electrical signals. Understanding the VGIC gating mechanism is vital to determine how neurons process information. More precisely, the VGIC gating mechanism leads to action potential (AP) initiation [12]. The classical description of AP initiation is based on Hodgkin and Huxley's landmark work in 1952 [1]. In their five-paper series, Hodgkin and Huxley explicated the concept of ion channels [29]. They presented a novel mathematical model that can replicate the experimental recording in the squid giant axon. The voltage-gated Na^+ and K^+ channels were represented by a fixed reversal potential and a variable ionic conductance, which is controlled by independent gating variables, each of which are governed by a first-order differential equation in time. The parameters of those equations depend only on the membrane potential. Despite its relatively simple nature, the Hodgkin–Huxley (HH) model can replicate the APs elicited from more complex neurons, such as central mammalian neurons, with simple parameter changes. Because of this remarkable property, the HH model is still one of the most commonly used computational neuronal models [29], [30]. Although a growing body of evidence in central mammalian neurons has indicated a discrepancy between experimental data and the HH model [2], [5], [6], [31], [32], most of the proposed models incorporate the basic functions and equations from the HH model [33], [34].

The nature of VGIC gating has been extensively researched. Contrary to the HH model assumptions, coupled gating has been observed in various VGICs [21]. The coupling between neighboring channels can be either positive or negative, and the process could be natural or caused

by diseases [21]. Positive cooperativity (i.e., the opening of one channel of a particular type increases the probability of the opening of neighboring channels of the same type) has been observed in cardiac Na⁺ channels [17], [35], K⁺ channels [36], and Ca²⁺ channels [37], [38]. Negative cooperativity (i.e., the opening of one channel inhibits the opening of other channels) is, however, less observed compared to positive cooperativity [21], and has mainly been observed in Na⁺ channels [39], [40].

Negative cooperativity was observed in Na⁺ channels. Neumcke and Stampfl altered Na⁺ conductance in the frog nerve nodal membrane using tetrodotoxin (TTX) while varying the holding membrane potential [40]. They reported an increase in the channel conductance after blocking some of the Na⁺ channels, thereby indicating negative cooperativity between the channels at the nodal membrane [40]. Negative cooperativity was also found in neuroblastoma cells. Iwasa *et al.* analyzed voltage-clamped recordings from a neuroblastoma cell membrane patch that contained two toxin-modified Na⁺ channels to determine whether these two channels are independent and identical [39]. They noted a negative interaction between the two channels. Although both studies found negative cooperativity between the Na⁺ channels, their results are unrelated [39]. Neumcke and Stämpfli reported that negative cooperativity occurs only where channels are located in high density and is based on substantial depletion of number of available ions through a cluster of channels. Also, the mechanism described by Iwasa *et al.* is based on a slower opening rate for a channel when an adjacent channel is open. Regardless of the different views, negative interaction, although rare, was detected between Na⁺ channels in different cell types.

2.2 Na⁺ channels inactivation mechanism

Rosalie C. Hoyt made one of the earliest attempts to apply coupled gating in 1963. Hoyt assumed that Na⁺ activation and inactivation are coupled. Thus, in her work, the gating of Na⁺ was represented by a single variable instead of using two independent gating variables as in the HH model [41], [42]. As compared to the HH model, the first Hoyt model provided better agreement with experimental data from the squid giant axon, although the differences between the two models were marginal [41]. Furthermore, in 1970, Hoyt and Adelman reported that the coupled gating model fits the squid axon data better than the HH model for the early part of the Na⁺ inactivation process [43]. While one major criticism of the Hoyt model was the uncompensated series resistance, Goldman and Schauf demonstrated that the coupled Na⁺ channel gating mechanism was still valid after adding series resistance, which provided a good fit to the *Myxicola* axon data [44]. Altogether, even though they are less famous than the independent gating models, different models based on coupled gating mechanisms have been propounded. These early studies on coupled gating have led to the current view of the Na⁺ channel inactivation process, where it is not considered voltage-dependent and is promoted by the activation process [45], [46].

The work on the Na⁺ channel inactivation process had led to the development of the ball-and-chain model. In 1973, Bezanilla and Armstrong developed a new signal averager that allowed them to make the first measurement of Na⁺ gating current [47]. A few years later, Bezanilla and Armstrong, using the voltage-clamp technique and the pronase enzyme to remove the inactivation, postulated the ball-and-chain model [48], [49]. The ball blocks the Na⁺ channel and the inactivation gain its voltage-dependence from the channel activation gate. Moreover, with the advances in Na⁺ current single-channel recording, multiple studies have confirmed the coupling between the activation and inactivation of Na⁺ channels [50]–[52], which brought more evidence that the Na⁺

gating mechanism deviates from the HH model. In addition, it inspired a new set of models that used the allosteric mechanism for Na⁺ channel gating [53], [54].

2.3 Na⁺ channel activation mechanisms

Na⁺ activation was another source of discrepancy when applying the original HH model to central mammalian neurons [2], [3], [46]. The exponent of the Na⁺ channel activation gate (m) varies according to the depolarization strength from 2, for small depolarization, to 4, for large depolarization [55]. By contrast, Baranauskas and Martina affirmed that the activation delay observed in several central mammalian neurons was markedly less than that predicted using the HH model [56]. These cumulative studies over the years have confirmed that mammalian Na⁺ and K⁺ channels' kinetics deviate from the canonical HH model, and thus, there exists a need to reevaluate the role of Na⁺ and K⁺ channel kinetics in biophysical models [57].

Cooperativity between neighboring Na⁺ channels is a relatively new idea [2] and a subject of heated debate. In 2006, Naundorf *et al.* published their controversial paper on unique features of APs in cortical neurons. Specifically, they observed two unique features in electrophysiological recordings of somatic APs in cortical neurons: rapid AP initiation and variability of AP onset potential [2]. The researchers failed to replicate these features in a single-compartment HH model, indicating that the HH model cannot account for these salient features. Therefore, they proposed a theory of cooperative Na⁺ channels, which assumes that each Na⁺ channel is functionally coupled to adjacent channels. The opening of one channel facilitates the opening of neighboring channels to shift the cumulative activation curve to more polarized (negative) values [2]. The proposed model replicates experimental data when modeling Na⁺ channels with strong cooperative activation, voltage-dependent inactivation from closed states, and slow deinactivation [2].

However, the debate continues about the validity of the cooperative Na⁺ channels activation hypothesis due to the lack of direct experimental evidence.

The cooperative gating theory engendered opposing opinions. Some studies described the theory as radical, unconventional, and even unnecessary [3], [30], [46], [58]. In opposition to the cooperative gating hypothesis, some studies attributed the sharp AP onset to compartmentalization. The somatodendritic compartment acts as a current sink for sodium current propagating from the AP initiation site at the axon, causing a sharp somatic AP [7], [59]. However, the most notable opposition came from McCormick *et al.* In their response to Naundorf *et al.*, McCormick *et al.* asserted that the HH model used in the former's analysis did not include the spike initiation site [30]. They showed that using the original HH model that AP backpropagation from the axon initial segment (AIS), where the spike initiated, caused the somatic AP initiation to be sharp, while the AP at the AIS was smooth [38]. These results agreed with the onset recordings from injury-induced cortical neurons [3].

However, the AP backpropagation arguments have two main criticisms. First, the axonal recordings were obtained from injury-induced swellings of cut axons on the slice surface [3]. The bleb caused by the injured axon destroys the sub-membrane network that integrates Na⁺ channels into the supramolecular machinery of the normal AIS [60]. Thus, the smooth AIS AP onset could be due to the disorganized state of the injured axon [60]. Second, Na⁺ channel density in the axon was higher than the AIS's suggested density [6], [61], [62]. Thus, after modifying the Na⁺ channel density, more studies investigated the sharp AP onset in multicompartment models. These studies concluded that AP backpropagation partially accounts for the sharp initiation of APs observed in cortical neurons. However, it is not sufficient to replicate the experimental data alone, and

including cooperative Na⁺ channel gating in addition is necessary to mimic the sharp AP initiation in computational models [6], [62]–[64].

In the past decade, the cooperative Na⁺ gating hypothesis has gained some momentum in the computational neuroscience field. In 2010, Baranauskas *et al.* used multicompartment models to find the active and passive parameters to replicate cortical neuron recordings [63]. They found that AP backpropagation elicited by the classical and modified HH models with fast onset kinetics did not necessarily cause sharp somatic AP onset, and hence other factors are required to explain these features [63]. Huang *et al.* investigated what fraction of cooperative Na⁺ channels were needed to reproduce sharp AP onset in cortical neurons [5]. They constructed a conductance-based neuron model in which the Na⁺ gating mechanism was varied from fully independent, like in the HH model, to fully cooperative. They found that with a small fraction of strongly coupled Na⁺ channels (5%–15%), the model generated the most rapid onset, produced a biphasic AP waveform, and enhanced the neuron's ability to phase-lock their firing to high-frequency input fluctuation [5]. Another modeling study also showed that cortical neurons could phase-lock their firing to signals with frequencies up to 400 Hz and respond within 2 ms to small changes in the input signal, which was reproduced using a multicompartment model with a fraction of AIS cooperative Na⁺ channels [64]. Furthermore, cooperative gating was proposed to induce memory. Pfeiffer *et al.* showed that clusters of cooperative Na⁺ channels could form bistable conductances, causing short-term memory [65]. Therefore, cooperative gating might cause faster neuronal response and regulate neuronal activity.

In recent years, several studies have shown more biological evidence supporting the cooperativity of Na⁺ channels. In 2014, a study showed using Na⁺ channel's crystal structure that the β 3-subunits can bind to multiple sites of Nav1.5 α -subunits [16]. Another study found that the

Na⁺ channels' α -subunits physically interacted and identified the protein-mediated coupled gating [17]. Clatot *et al.*'s findings supported Naundorf *et al.* Na⁺ cooperative model results. Furthermore, channel cooperativity was linked to Na⁺ channel mutation. A study showed that the dominant negative effect of mutant Na⁺ channels is due to trafficking deficiency and cooperative gating impairment [18], and uncoupling Na⁺ channel dimers can rescue the pain caused by Nav1.7 channel mutation [19]. The growing body of biological evidence on the role of cooperative Na⁺ gating indicates that Na⁺ channel kinetics diverges from conventional paradigms. Thus, a more realistic biophysical model needs to be developed that can explain the experimental data.

2.4 Ion concentration dynamics in neurons

Ion movement through VGICs underlies neuronal signaling. Yet, ion concentration change is ignored when modeling neuronal normal electrical behavior, assuming that the total number of ions flowing through channels is too small to cause any significant change. This, however, might not be true in vertebrate neurons. For example, increases in the level of extracellular K⁺ concentration in cortical neurons were associated with physiological stimuli [22] and periodic fluctuations during sleep [23]. Also, spontaneous and ultraslow fluctuation in Na⁺ concentration was observed in neonatal neurons, making the cell more vulnerable to seizures, which diminish after blocking AP generation [24], [25]. In addition, increasing intracellular Na⁺ concentration was shown to facilitate seizure termination [66]. However, although changes in ion concentration are observed in normal and pathological neuronal states, computational models with dynamic ion concentration were used mainly to study abnormal neuronal activities. Cressman *et al.* constructed a conductance-based neuron model with Na⁺ and K⁺ concentration dynamics. Their study showed that changes in ion concentration led to seizure-like events [26], [67]. Tagluk and Tekin also studied the influence of ion concentrations on neuronal dynamical behavior [68]. They concluded

that while the Na^+ concentration had a slight impact on amplitude, it had a smaller influence on other AP attributes, whereas the K^+ concentration significantly impacted almost all aspects of the AP generation [68]. In contrast, other studies emphasized the critical role of changes in Na^+ concentration on electrical activity. Zylbertal *et al.* (2015) showed that intracellular Na^+ concentration's prolonged dynamics control the persistent neuronal activity in mitral cells using electrophysiological recordings, imaging, and computational modeling [69]. Furthermore, in another computational study, Zylbertal *et al.* showed that the dynamic of Na^+ concentration in three neuron types, including cortical pyramidal neurons, has a significant impact on neuron-bursting activity [70]. These studies indicate the importance of dynamical ion concentration on neuronal activities in both normal and abnormal neuronal activities.

2.5 Models of cooperative Na^+ channel gating

This section contains three cooperative Na^+ channel models proposed since 2006. These models include; the Naundorf *et al* model, the Huang *et al* model, and the Öz *et al* model. Table 2.1 shows a comparison between three Na^+ channels cooperative models.

Table 2.1: Comparison between three cooperative Na^+ channels models

Cooperative model (Based on*)	Ion channels	Na^+ current (coupling)	Notes
Naundorf et al (2006) (Aldrich et al (1983))	Leak Na^+	$\bar{g}_{\text{Na}^+} o(V_{\text{Na}}^+) (E_{\text{Na}^+} - V)$ $V_{\text{Na}}^+ = V + KJo$	<ul style="list-style-type: none"> • one gating parameter - $o(V_{\text{Na}}^+)$ • All Na^+ channels are cooperative • No K^+ channels
Huang et al (2012) (Wang-Buzsaki (1991))	Leak K^+ Na^+	$\bar{g}_{\text{Na}^+} (m_c^x (V_{\text{Na}}^+) h) (E_{\text{Na}^+} - V)$ $V_{\text{Na}}^+ = V + KJm^x h$ $x = 1-3$	<ul style="list-style-type: none"> • Neglects activation delay, $m = m_\infty$ • Fraction of Na^+ channels are cooperative

Öz et al (2015) (Huang et al (2012))	Leak K ⁺ Na ⁺	$\bar{g}_{Na^+}(m_c^3(V_{Na^+}^+)h)(E_{Na^+} - V)$ $V_{Na^+}^+ = V + KJm^3h$	<ul style="list-style-type: none"> • Neglects activation delay, $m = m_\infty$ • Fraction of Na⁺ channels are cooperative • Varying \bar{g}_{Na^+} values • Includes AP backpropagation
---	---	--	--

* Note that Aldrich and WB models are based on HH model with some simplification.

Naundorf et al. model [2]

In 2006, Naundorf *et al.* proposed a cooperative Na⁺ channels model that can replicate two unique features observed in cortical neuron recordings: variability of AP onset and fast onset rapidity [2]. They used a single channel model since the two features occur in the AP initial part. Hence, the features are dependent only on Na⁺ channels. Therefore, K⁺ channels are excluded from the model and replaced by a large leakage conductance [2]. Naundorf *et al.* based his model on Aldrich *et al.* (1983) single channel model, in which the channel can be in three states, as shown in Figure 2.1 [51]. The transition between open and closed states is voltage-dependent, whereas channel inactivation is as a state-dependent from the open state. To make Na⁺ channels activate cooperatively, Naundorf *et al.* introduced a coupling strength (J) for a number of neighboring channels (K) that shift the activation voltage toward more polarized (negative) values. Thus, by varying the coupling strength value, Na⁺ channels activation can be independent when $J=0$, and cooperative when $J>0$. AP generation dynamics, including the fraction of open Na⁺ channels (O), and the fraction of available Na⁺ channels (H) is described by the following equations:

$$C \frac{dV}{dt} = g_L(E_L - V(t)) + g_{Na^+}O(t)(E_{Na^+} - V(t)) + I_{app}$$

$$\frac{dO}{dt} = \alpha_o(V(t) + KJO(t))(H(t) - O(t)) - \left(\tau_I^{-1} + \beta_o(V + KJO(t)) \right) O(t)$$

$$\frac{dH}{dt} = \alpha_c(V)(1 - H(t)) - \beta_c(V)(H(t) - O(t)) - \tau_I^{-1}O(t)$$

Where g_i is the maximum conductance, E_L is the channel reversal potential, and I_{app} represents the applied current. α_i and β_i represent the rate constant functions and τ_I is the inactivation time constant.

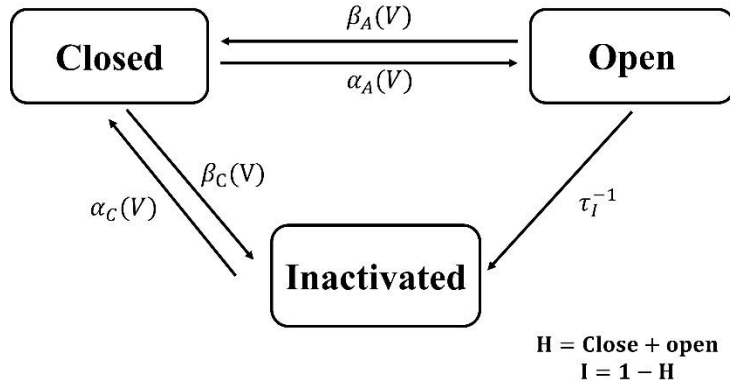


Figure 2.1: State transition scheme of the single sodium channel model. H is the fraction of available channels and I is the fraction of inactivated channels. τ_I^{-1} is the transition rate between closed and open states. The transitions between closed and open states and between inactivated and closed states occur with rates $\alpha_A(V)$ (opening), $\beta_A(V)$ (closing) and $\alpha_C(V)$ (de-inactivation), $\beta_C(V)$ (inactivation), respectively. The figure is reproduced as in Naundorf et al., 2006.

Huang et al. model [5]

In 2012, Huang *et al.* introduced their cooperative model to answer two questions: (1) Does the cooperative Na^+ channels model influence neuronal populations' encoding properties? (2) Can a fraction of cooperative Na^+ channels reproduce the characteristic properties reported in previous theoretical studies? To answer these questions, Huang *et al.* developed a conductance-based model where they continuously varied the coupling strength and fraction (p) of Na^+ channels exhibiting cooperativity. They showed that with a small p and a strong cooperativity, AP rapidity and threshold variability increase together, and the AP exhibits a two-component waveform, similar to electrophysiological recordings. Moreover, they showed that the presence of a small fraction of cooperative Na^+ channels significantly enhanced the neuronal ability to phase-lock their firing to high-frequency input fluctuation, similar to experimental data [5].

The AP dynamic was based on an HH-type neuron model, the Wang-Buzsaki (WB) model [71]. The WB model is described as the following:

$$C \frac{dV}{dt} = I_{Leak} + I_{K^+} + (1 - p)I_{Na^+} + pI_{Na_c^+} + I_{app}$$

Where all variables and constants are as described in the original HH model except for the new term $I_{Na_c^+}$, which represents the cooperative Na⁺ channels current, which is defined as:

$$I_{Na_c^+} = \bar{g}_{Na^+} (m_c^x h) (E_{Na^+} - V(t))$$

$$m_c(V) = m_c(V + KJm_c(V)h(V))$$

where x is the exponent of the activation function ($x = 3$ in the original HH model), J is the coupling constant, K is the number of coupled adjacent channels, and m_c is the cooperative Na⁺ channels activation variable, m is the same for the conventional (independent) Na⁺ channels, and h is the inactivation variable for both the cooperative and conventional channels.

Öz et al. model [6]

In 2015, *Öz et al.* compared the impact of cooperative and independent Na⁺ channels in the AIS on AP initiation. They developed a conductance-based model that includes a multi neuronal compartment from a dendrite compartment to a bleb after the first node of Ranvier compartment [6]. In this model, only a fraction of the AIS Na⁺ channels were activated cooperatively, while the channels in the other compartments exhibited independent gating. The main findings of *Öz et al.* were that only the cooperative model reproduced the abrupt AP onset observed in cortical neurons, and the cooperative model was able to reproduce the sharp somatic AP with the AIS Na⁺ channels density only 3-fold to 10-fold higher than the soma [6]. Also, they found that the coupling strength and the fraction of cooperative Na⁺ channels were ineffective on the localization of action potential

initiation, but crucial for increasing AP rapidity. The Öz *et al.* model was similar to the Huang *et al.* model where only a fraction (p) of the Na^+ channels exhibit cooperative gating, but cooperative gating is only implemented in the axon initial segment compartment (independent Na^+ channel gating elsewhere).

3 NEW METHOD TO ANALYZE THE RAPIDITY OF ACTION POTENTIAL INITIATION

Preface

This chapter was published in the *Biomedical Science Instrumentation* journal in April 2020 and was co-authored by Aldohbeyb, Vigh, and Lear. Ahmed A. Aldohbeyb's contributions were writing the MATLAB codes for the HH model, obtaining the electrophysiological recordings from publicly available databases, calculating the AP attributes, testing the sensitivity and specificity of AP rapidity quantification methods to Na⁺ channels, analyzing the data, identifying and describing prior related work, discussing all aspects of the research, conceptualizing many figures and creating all of them, writing the original manuscript, editing text and figures based on feedback from the other co-authors, and corresponding with the publisher. This chapter is the same as the published paper, except for minor formatting edits to follow CSU Graduate School formatting and submission guidelines (citation style and tables designs).

Abstract

Recent studies show a kink at action potential, AP, onset in some cortical and retinal neurons. Several papers have quantified the rapidity of AP onset, i.e., how kinked the AP initiation is, and found the rapidity to be faster than predicted by the Hodgkin-Huxley model (HH) and conclude the HH model is missing critical biophysics. However, these works typically define AP onset rapidity subjectively, often using an arbitrary value of \dot{V}_m , the first time derivative of the membrane potential. Therefore, we propose more systematic methods to analyze the AP initiation using the full width at half maximum (FWHM) and half width at half maximum (HWHM) of the onset peak in \ddot{V}_m , the second time derivative. The maximum \ddot{V}_m occurs when the Na⁺ current changes fastest. Hence, the FWHM and HWHM of \ddot{V}_m are well-defined and intuitive measures of

onset rapidity. To examine the proposed methods, we have varied the rate constant parameters in the HH model and numerically calculated the resultant FWHM and HWHM of \ddot{V}_m alongside previously published approaches. The results show that both the FWHM and HWHM methods are more sensitive to changes in HH parameters, giving a wider range of onset rapidity while remaining minimally affected by other aspects such as the AP width. Furthermore, we used the methods to analyze the onset rapidity in somatosensory cortical neurons. The results from FWHM and HWHM methods show a low variation between the neurons analyzed here while exhibiting relatively high variation in neurons with high AP shape variability compared to the widely used phase slope method. Our results indicate that the FWHM and HWHM methods are more sensitive and specific to measure the AP onset dynamics. Thus, quantifying the rapidity of AP onset using the FWHM and HWHM methods provides a systematic tool to analyze the AP onset dynamics and allow direct comparison between experimental data.

3.1 Introduction

The work of Hodgkin and Huxley (HH) has been a cornerstone in forming our current understanding of the mechanism of neuron firing. Their work on the giant squid axon has led to the development of their famous mathematical model [1]. This simplified model captures the overall features of neurons' firing dynamics and predicts that once the membrane potential, V_m , exceeds a certain threshold potential, V_m rises smoothly and an action potential (AP) is generated. However, recent studies in the cortex and some retinal neurons have shown that the initial AP depolarization might be faster than predicted by the classical HH model [2], [64]. In these cells, the onset of the AP appeared as a sharp kink as opposed to the gradual rise predicted by the HH model. As a result, several studies have focused on examining and analyzing the AP onset in these neurons [2], [30], [62]. The results from these studies are controversial; some researchers have

suggested alternative models while others emphasize that such a rapid onset can be explained with a multicompartment HH model [2], [3], [6], [30], [62]–[64], [72].

However, the definition of AP onset and onset rapidity differ from one study to another and many definitions involve arbitrary AP thresholds. The most common definition of AP onset is when the rate of V_m change equals some value and further defines the rapidity of AP onset as the slope of a fitting line that is tangent to that point [2], [3], [8], [73], [74]. Each of these works typically defined AP onset rapidity subjectively as they used different onset values (e.g., 10 mV/ms in [2]; 15 mV/ms in [30]; 20 mV/ms in [64]; 50 mV/ms in [75]). Other studies defined the AP onset as the value at which the membrane potential's second or third derivative reaches its maximum value [12], [76], [77]. However, determination of when onset occurs does not provide a measure of the rapidity of onset. The wide variety of these definitions – particularly the use of arbitrary constants – causes potential confusion, complicates comparison of different models and data sets, and may obscure underlying commonalities. Therefore, we propose a more systematic and consistent method to analyze AP onset rapidity using the full width at half max (FWHM) and the half width at half max (HWHM) of the rising phase of the membrane potential's second time derivative (\ddot{V}_m). The maximum value of \ddot{V}_m indicates the highest acceleration of V_m reflecting the fastest change in Na^+ current. Thus, the HWHM of \ddot{V}_m measures the length of time needed to reach the fastest change in Na^+ current starting from a time when the rate of change is only half that fast. Likewise, the FWHM of \ddot{V}_m indicates the length of time needed to transition from half the maximum rate, through the maximum, and back down to half the maximum rate of change in Na^+ current. Together, the FWHM and HWHM of \ddot{V}_m provide a robust measure of the rapidity of AP onset. Further, as will be shown below, these methods are more sensitive to small changes in the HH rate constant parameters affecting AP onset rapidity than the commonly used

first derivative methods. Beneficially, the FWHM and HWHM measures of onset rapidity are minimally influenced by other aspects of the AP that extend beyond onset such as the AP width. Moreover, when these methods are used to analyze current clamp recordings from mice somatosensory cortex neurons, the HWHM method has the lowest variation across pyramidal regular-spiking cortical neurons, is least impacted by backpropagation signals, and shows higher relative variation in neurons that have high AP shape variability. Thus, the HWHM method is more sensitive and specific to measure the AP onset dynamics.

3.2 Methods

Data Source for AP Recordings

Electrophysiological recordings were obtained from the GigaScience Database. The experimental procedures and recording are found in da Silva Lantyer *et al.*, 2018 [78]. The recordings we used were current clamp recordings from pyramidal regular-spiking neurons in primary somatosensory cortex of adult female mice. The recordings were obtained from 11 pyramidal regular-spiking neurons from 8 mice ranging from 165 to 282 days old. The data analyzed here was obtained and uploaded to the database by Angelica da Silva (AL) and were found to be the cleanest recordings with the lowest noise in that database. The recording labels in the database are given in da Silva Lantyer *et al.* Supporting Information [78].

We analyzed the AL-series recordings that satisfied the following criteria. Each current step recording had to contain at least 2 APs. Each AP had to be separated by at least 30 ms from the preceding AP to exclude the variability caused by the incomplete deinactivation of the sodium channels as described in Naundorf *et al.*, 2006 [2]. For each AP that fulfilled the above criteria,

\dot{V}_m and \ddot{V}_m are computed using MATLAB's *diff* function and then interpolated to a resolution of $\Delta t = 1 \mu\text{s}$ using MATLAB's spline function (MATLAB V9.5 (R2018b)).

Quantification of the Rapidity of the AP onset

The rapidity of AP onset was determined using two novel methods, the FWHM method and the HWHM method, and one existing method, the slope of the curve in the AP phase plot [2], [3]. First, the rapidity of AP onset was quantified using the FWHM of the rising phase of \ddot{V}_m . After computing \ddot{V}_m as described above, the initial portion of \ddot{V}_m vs time was selected from 3 ms before the peak up to the point when \ddot{V}_m drops to zero after peaking. Then, the FWHM was determined to be the time difference between when \ddot{V}_m rises past half the maximum value (Fig. 3.1C dotted line) and when it decays below it. The HWHM was calculated in a similar manner, except the HWHM was defined as the time it takes \ddot{V}_m to rise from half its maximum value to its maximum value. The inverse of the FWHM and HWHM is used to measure the rapidity of AP onset in units of 1/time. For the slope method, \dot{V}_m was plotted against V_m to yield the phase plot. A tangent line to the plot at the vertical coordinate of $\dot{V}_m = 10 \text{ mV/ms}$ is determined as in Naundorf *et al*, 2006 [2] (Fig. 3.1D). The slope of that tangent line, or equivalently the slope of the phase curve at that point, is defined as the rapidity of a AP onset [2], [3], [63].

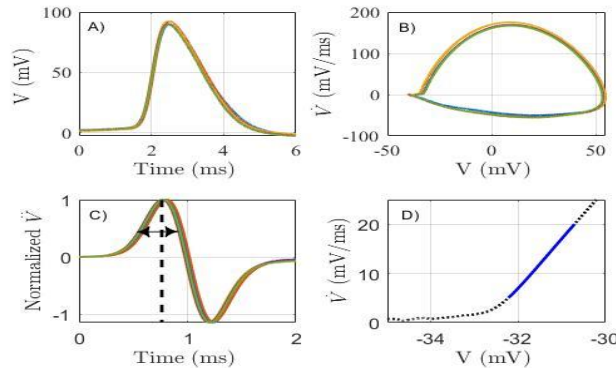


Figure 3.1: Comparison between AP quantification methods. A) \dot{V}_m plots of 5 overlapped APs elicited by a 240 pA current step for 0.5 s. B) Phase plots of the same APs in A, C) The second-time derivative of the APs in A. The double arrowheads indicate the FWHM and the dashed line indicates the maximum value, so, the HWHM is measured

from the left arrowhead to the dashed line. The dashed line and the double arrow are for illustration purposes and not exact. D) The slope of the line (blue trace) fitting one of the AP's phase plot (black dashed trace) in B. The blue trace indicates the tangent at 10 mV ms^{-1} .

HH model for cortical neurons

The model used here is a single compartment HH model [79]. In this model, the membrane potential dynamically follows the equation:

$$C \, dV/dt = -\bar{g}_{Leak}(V - E_{Leak}) - I_{Na^+} - I_{DK^+} - I_{NK^+} - I_{inj} \quad (\text{Eq. 1})$$

where V is the membrane potential; $C = 1 \mu\text{F}/\text{cm}^2$ is the specific membrane capacitance; $\bar{g}_{Leak} = 0.0045 \text{ mS}/\text{cm}^2$ is the leakage maximum conductance, and $E_{Leak} = -80 \text{ mV}$ is the leak reversal potential. I_{Na^+} is the voltage-gated sodium channels' (VGSCs') current. I_{DK^+} and I_{NK^+} are the voltage-gated delayed-rectifier potassium channels' (VGdKCs') current and the non-inactivating potassium channels' (VGnKCs') current, respectively. I_{inj} is the injected stimulus current.

The VGSCs', VGdKCs', and VGnKCs' current densities as described in Destexhe *et al.*, 1999 [79] are governed by the following dynamical equations:

$$\begin{aligned} I_{Na^+} &= \bar{g}_{Na^+} m^3 h (V - E_{Na^+}) \\ I_{DK^+} &= \bar{g}_{K^+} n^4 (V - E_{K^+}) \\ \frac{dm}{dt} &= \alpha_m (1 - m) - \beta_m m \\ \frac{dh}{dt} &= \alpha_h (1 - h) - \beta_h h \\ \frac{dn}{dt} &= \alpha_n (1 - n) - \beta_n n \\ \frac{dp}{dt} &= \alpha_p (1 - p) - \beta_p p \quad (\text{Eq. 2}) \end{aligned}$$

Where \bar{g}_{Na^+} is VGSCs' maximum conductance ($\bar{g}_{Na^+} = 120 \text{ mS/cm}^2$ unless stated otherwise). $E_{Na^+} = 40 \text{ mV}$ is the VGSC reversal potential. m and h are the activation and inactivation variables of the VGSCs. VGdKCs' maximum conductance is $\bar{g}_{K^+} = 36 \text{ mS/cm}^2$ unless stated otherwise [2]. $E_{K^+} = -95 \text{ mV}$ is the VGdKCs reversal potential. n is the activation variable of the VGdKCs. $\bar{g}_{NK^+} = 0.005 \text{ mS/cm}^2$ is VGnKCs maximum conductance. p is the activation variable of the VGnKCs. α_i and β_i are the rate constants functions for each ion channel gate. The equations of α_i and β_i are shown in Table. 3.1.

Table 3.1 Rate constants equations. Nominal values for a, b, and c are shown as described in [79].

Type	Gate	α_i	β_i
VGSCs	m	$\frac{-0.32(V - V_T - 13)}{\exp\left(\frac{V - V_T - 13}{4}\right) - 1}$	$\frac{0.28(V - V_T - 40)}{\exp\left(\frac{V - V_T - 40}{5}\right) - 1}$
	h	$0.128 \exp\left(-\frac{V - V_T - V_S - 17}{18}\right)$	$\frac{4}{1 + \exp\left(\frac{V - V_T - V_S - 40}{5}\right)}$
VGdKCs	n	$\frac{-0.032(V - V_T - 15)}{\exp\left(\frac{V - V_T - 15}{5}\right) - 1}$	$0.5 \exp\left(-\frac{V - V_T - 10}{40}\right)$
VGnKCs	p	$\frac{0.0001(V + 30)}{1 - \exp\left(-\frac{V + 30}{9}\right)}$	$\frac{-0.0001(V + 30)}{1 - \exp\left(\frac{V + 30}{9}\right)}$

The rate constants parameters (Table 3.1) are chosen as the best values to fit the experimental data [80], [81]. Thus, these equations influence many aspects of the AP's shape such as the spike width, onset potential, and the rapidness of AP onset. Therefore, we examined the sensitivity of onset rapidity, as quantified by each of the methods, to changes in the rate constant parameters. Each rate constant's equation has three parameters. For example, Eq. 3 shows the equation for VGSCs' activation gate, m , and we called the constant multiplying the equation a ,

the constant subtracted from the membrane potential b , and the constant dividing the membrane potential c . Then, we varied the values of a , b , or c from half the nominal HH values to one and a half the nominal HH values for each parameter. All the rate constants equations were treated in the same manner. Parabolic and linear fits were used to determine the maximum and half maximum values, respectively. Special care was taken to ensure that the membrane potential has a normal dynamic behavior.

$$\alpha_m = -a(V - V_T - b) / \exp\left(\frac{V - V_T - b}{c}\right) - 1 \quad (\text{Eq. 3})$$

3.3 Results

Measuring the impact of α_i and β_i parameters on the rapidity of AP onset

We varied the three parameters – a , b , and c – of each α_i and β_i rate constant from 0.5 to 1.5 of the parameter’s original value in the normal HH model, a_{HH} , b_{HH} , and c_{HH} . All the results presented here are for stable numerical solutions. If, at a given parameter value, the membrane potential is not stable or an AP is evoked before the stimulus current is injected, the result from that simulation is considered unrealistic and is not included in the analysis. All the results from the parameter variations presented here are from APs that maintain the general features of APs from the original HH model.

To test the robustness of FWHM and HWHM methods in quantifying the rapidity of AP onset, first we applied them to APs generated by the HH model and compared the resulting rapidity to that provided by the phase plot slope method. Using the three methods, we quantified the rapidity of AP onset as a function of each a , b , and c parameter in the stable range. The nominal values of rapidity for each of the three methods was obtained from the neocortical pyramidal neuron HH model [79], and the normalized values of rapidity were defined as the ratio of rapidity

to the normal value of rapidity obtained from the original HH model. Different rate constants' parameters lead to different effects on the AP shape such as changing the AP width and onset rapidity (Fig. 3.2). Rapidity determined using the FWHM and HWHM methods is generally more sensitive to changes in the rate constant parameters of VGSCs' activation and inactivation gates compared to the phase slope method. For example, the largest changes in the FWHM and HWHM rapidity occur when varying the a parameter in α_m . Varying a in the range $0.75 < a/a_{HH} < 1.5$ yields 60% change in the FWHM or HWHM rapidity while it produces less than 13% change using the phase slope method (Fig. 3.3). Higher sensitivity of the FWHM and HWHM methods to parameters can be observed in 11 out of 12 VGSCs' parameters (Fig. 3.3-3.4) with the exception being the c parameter for VGSCs activation.

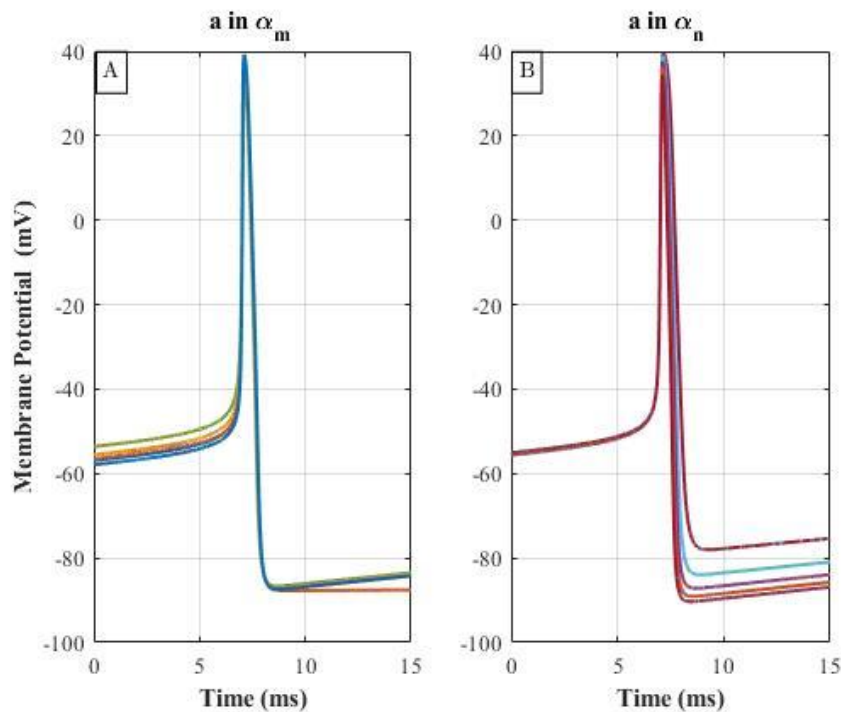


Figure 3.2: Variation of AP shape with changes in the rate constants' parameters in the HH model. A) APs when varying the parameter a in α_m . B) APs when varying the parameter a in α_n .

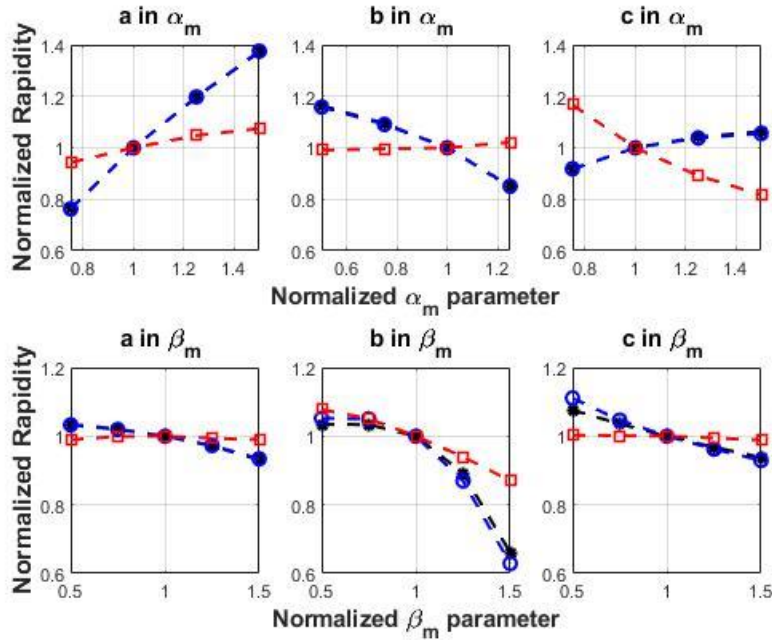


Figure 3.3: Comparison of the rapidity quantification methods' sensitivity to changes in the α_m and β_m parameters. The horizontal axis represents the parameter value normalized to the nominal value in the HH model, and the vertical axis represents the rapidity of the AP onset normalized to the rapidity of the AP onset at the nominal HH value. Black asterisks represent the values obtained by the FWHM method. Blue open circles represent the values obtained by the HWHM method and frequently fall directly on top of the black asterisks. Red squares represent the values obtained by the phase space slope method.

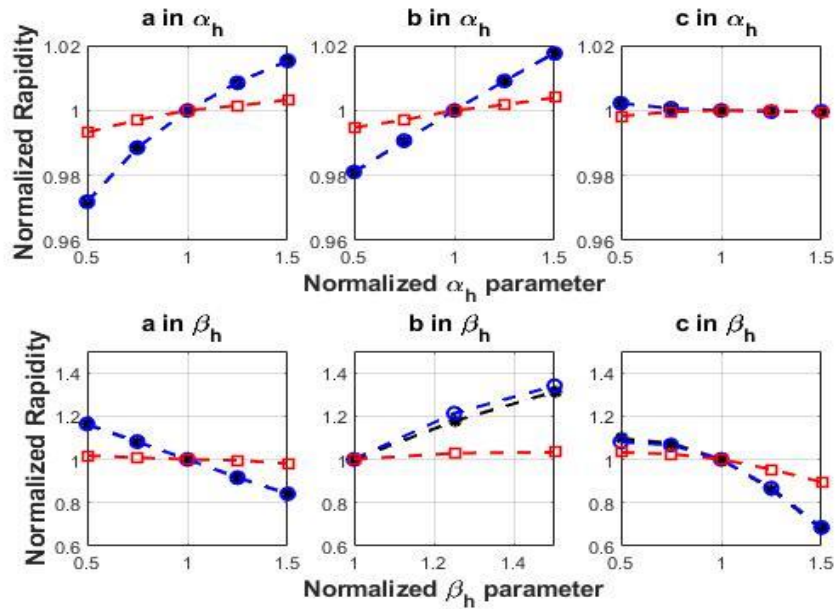


Figure 3.4: Comparison of the quantification methods' sensitivity to changes in the α_h and β_h parameters. The horizontal axis represents the difference in the parameter value compared to the value in the original HH model, and the vertical axis represents the rapidity of the AP onset normalized to the rapidity from the original HH values. Black asterisks represent the values obtained by the FWHM method. Blue circles represent the values obtained by the HWHM method. Red squares represent the values obtained by the phase slope method.

Next, we analyzed the results from varying the rate constant parameters of VGdKCs' activation gates. Contrary to the results from varying the rate constants parameters of VGSCs' activation and inactivation gates, the phase slope method is more sensitive to VGdKCs' rate constant parameter variation. Varying the value of a in β_n causes around 9 % change in the rapidity of AP onset using the phase slope method while it only altered the rapidity of AP onset by less than 2.6 % using the other methods introduced in this paper (Fig. 3.5). Thus, the analysis of the variation of rate constants parameters reveals that the FWHM and HWHM methods have a higher sensitivity to changes in the VGSCs' dynamics while being minimally influenced by changes in the VGdKCs' dynamics compared to the phase slope method.

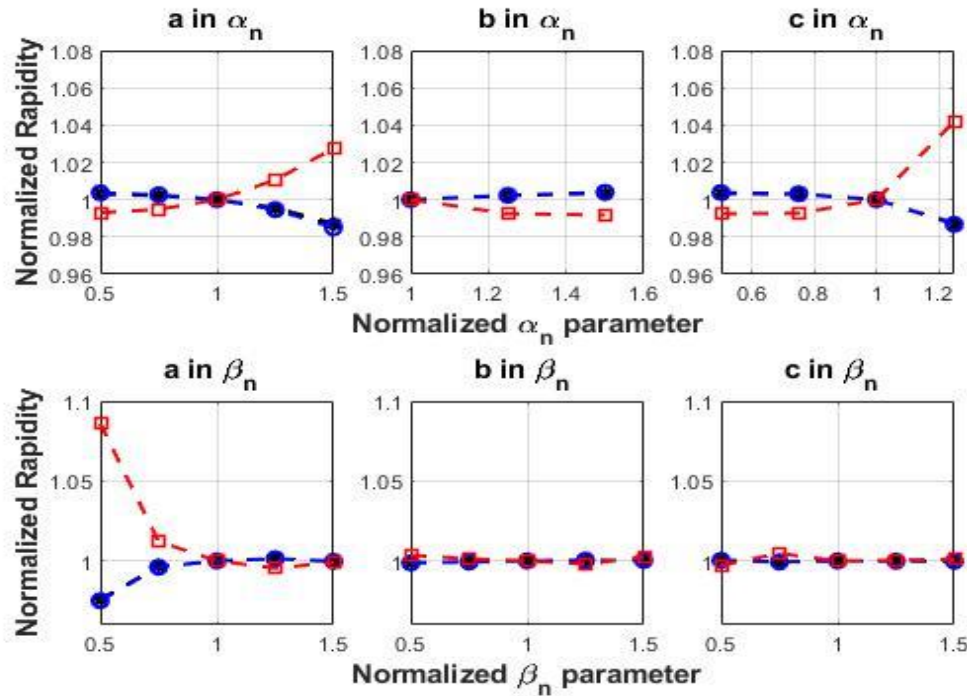


Figure 3.5: Comparison of the quantification methods' sensitivity to changes in the α_n and β_n parameters. The horizontal axis represents the difference in the parameter value compared to the value in the original HH model, and the vertical axis represents the rapidity of the AP onset normalized to the rapidity from the original HH values. Black asterisks represent the values obtained by the FWHM method. Blue circles represent the values obtained by the HWHM method. Red squares represent the values obtained by the phase slope method.

Moreover, to better understand the relation between the VGSCs, VGdKCs, and the rapidity quantification methods, we increased the VGSCs' or VGdKCs' \bar{g}_i by factors of 2 to 5

from the original values. As expected, the rapidity increased with increasing the VGSCs' maximum conductance using the three methods, but the sensitivity to such an increase is significantly different. With 5 times VGSCs' maximum conductance, the FWHM and HWHM rapidity doubled while the phase plot rapidity increased by less than 14 % (Table 3.2). On the other hand, although the variation was small with VGdKCs' conductance for the three methods, the phase slope shows higher sensitivity to VGdKCs' conductance compared to the FWHM and HWHM methods (Table. 3.3). Therefore, the FWHM and HWHM methods show a higher sensitivity and specificity to VGSCs' dynamics compared to the phase slope method.

Table 3.2: Values corresponding to increasing VGSCs

\bar{g}_{Na^+} (mS/cm ⁻²)	FWHM (ms ⁻¹)	HWHM (ms ⁻¹)	Phase slope (ms ⁻¹)	AP height (mV)	AP Width (ms)
120	14.53	21.75	3.26	93.21	0.49
240	20.21	30.12	3.47	96.49	0.59
360	24.03	35.72	3.58	97.57	0.66
480	26.98	40.01	3.65	98.21	0.71
600	29.43	43.55	3.71	98.66	0.76

Table 3.3: Values corresponding to increasing VGKCs

\bar{g}_{K^+} (mS/cm ⁻²)	FWHM (ms ⁻¹)	HWHM (ms ⁻¹)	Phase slope (ms ⁻¹)	AP height (mV)	AP Width (ms)
36	14.53	21.74	3.26	93.21	0.49
72	14.48	21.66	3.29	91.66	0.41
108	14.42	21.55	3.32	90.30	0.37
144	14.36	21.44	3.35	89.01	0.34
180	14.23	21.22	3.43	87.27	0.32

The rapidity of AP onset in recorded primary somatosensory cortical neurons

Current clamp recordings were obtained from Layer 2/3 regular spiking neurons (n = 11) in the adult female mice primary somatosensory cortex, as detailed in da Silva Lantyer *et al.*, 2018

[78]. Each recording has between 59 and 221 APs, with higher injected currents generating higher firing frequency and thus more APs. The mean and standard deviation of onset rapidity across all the APs in each recording are shown in Fig. 3.6. The HWHM method shows the lowest relative variation with less than 9 % difference between neurons ($4.1 \pm 0.4 \text{ ms}^{-1}$). The FWHM method shows a slightly higher relative variation with 12% difference between neurons ($2.2 \pm 0.3 \text{ ms}^{-1}$). On the other hand, the phase slope exhibits the highest relative variation between neurons with 18 % difference ($7.2 \pm 1.3 \text{ ms}^{-1}$).

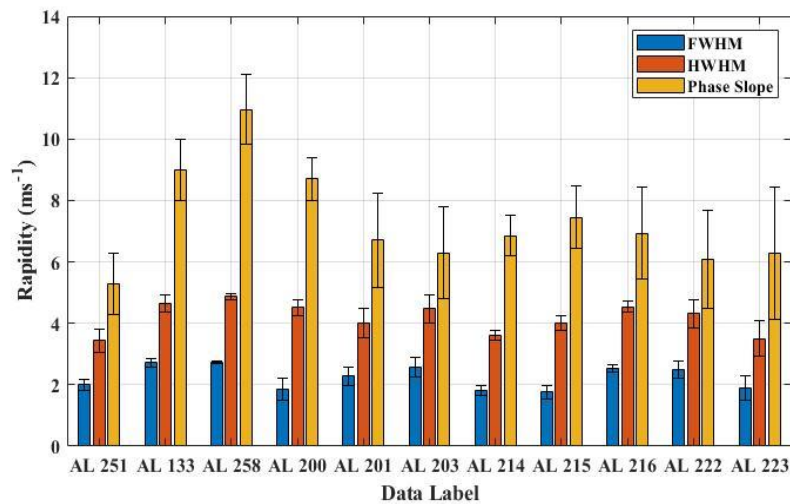


Figure 3.6: The average and standard deviation of the rapidity of AP onset in 11 neurons. The horizontal axis shows the recording labels for individual neurons in the database from da Silva Lantyer et al., 2018 [78]. The FWHM and HWHM give a smaller mean and standard deviation values than the phase slope.

In cortical neurons, the stimulus strength can alter the shape of the APs [10]. The difference in the APs' shape was observed in some of the neurons analyzed here. Such neurons show higher variabilities in the AP width, height, and the rapidity of AP onset. For example, two neurons, AL 258 and AL 223, with respectively high and low variabilities in AP shape are compared in Fig. 3.7. In the neuron with high AP shape variability, the amplitude and width have a range from 49.4 to 93.6 mV and 1.75 to 3.25 ms. In contrast, the other neuron shows low variability with only a range from 69.7 to 78.5 mV in amplitude and a range from 1.42 to 2.03 ms in width. Such a

variation in AP shape influences the rapidity of AP onset. In this case, all the onset rapidity quantification methods exhibit a relative higher variation for neurons with high AP shape variability. Nevertheless, the HWHM method yields the lowest relative variation in AP onset rapidity across different pyramidal regular-spiking cortical neurons as shown in Fig. 3.8.

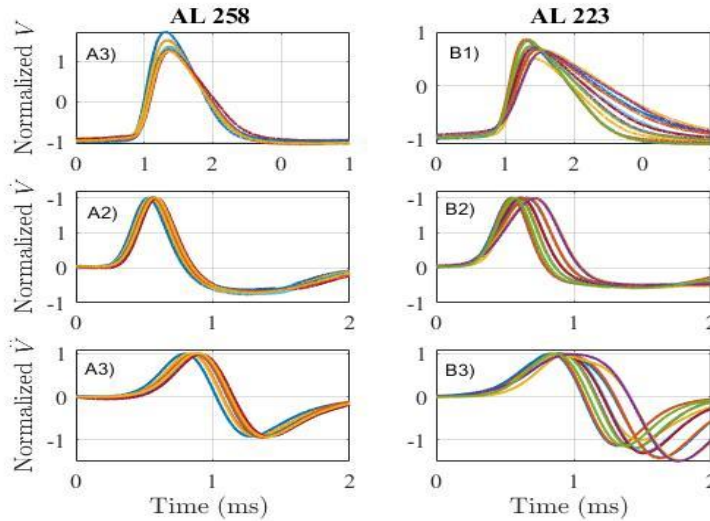


Figure 3.7: Variation in neuronal response between individual neurons. A1) Normalized APs of a neuron that exhibited low AP variability with changes in stimulus strength. B1) Normalized membrane potential of a neuron that exhibited high AP variability with changes in stimulus strength. A2) The rate of membrane potential change for APs shown in A1. B2) The rate of membrane potential change for APs shown in B1. A3) Acceleration of membrane potential for APs shown in A1. B3) acceleration of membrane potential for APs shown in B1. AL 258 & AL 223 are the labels of the neurons recorded in the database from da Silva Lantyer et al., 2018 [78].

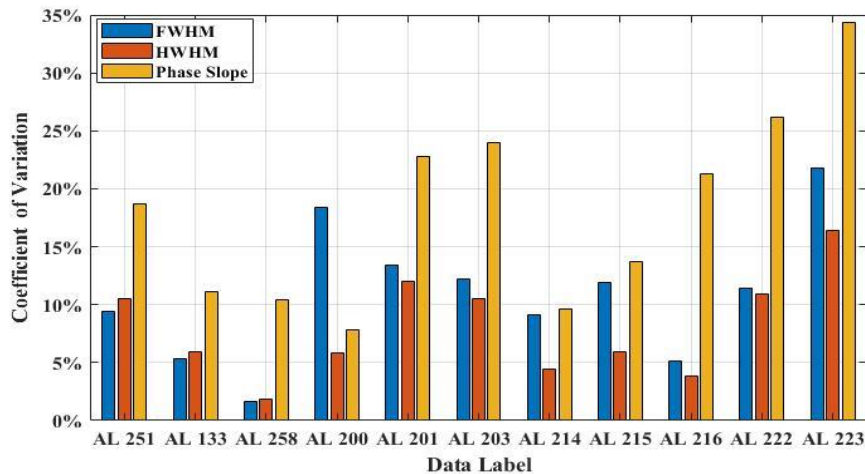


Figure 3.8: The coefficient of variation of the rapidity of AP onset in neurons. The coefficient of variation is the standard deviation divided by average. The horizontal axis shows the recordings label for individual neurons in the database from da Silva Lantyer et al., 2018 [78].

In some of the neurons analyzed here, the somatic recordings exhibited a different AP waveform which can be shown clearly in the \dot{V} plots as double peaks and two humps in the phase plot (Fig. 3.9). The double peak in the second derivative plots indicates two processes contribute to the AP's rising phase. The double peak is characteristic of AP backpropagation from an initiation site in the axon to the soma [3], [9]. Such APs contain two components, somatic AP, and axonal backpropagation AP. Moreover, no significant difference in the AP onset dynamics of cortical neurons was found between single and double component APs [9]. However, in the two neurons that have a two clear AP components APs (labeled AL 200 and AL 215), both the FWHM and phase slope method show high sensitivity to the backpropagation signal. The HWHM method, however, did not show any significant impact (Fig. 3.9). These results indicate that the HWHM method can quantify the rapidity of APs onset more reliably than the other methods.

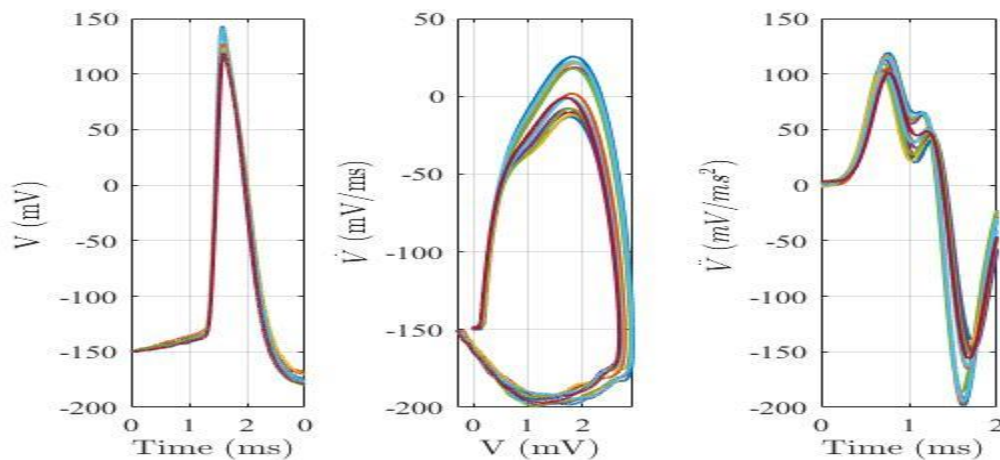


Figure 3.9: Neurons evoked different AP waveforms. A) APs recorded from the neuron labeled AL 200 from da Silva Lantyer et al., 2018 [78]. B) phase plots of the APs in A. C) Second derivative plots of the APs in A.

Finally, we looked at the correlation between the three methods and the AP amplitude and width. Previous work had shown that in cortical neurons AP height decreases are correlated with wider APs and lower phase slope, which indicate a high degree of VGSCs inactivation [10].

Therefore, here we demonstrate that the HWHM method shows a lower variation from one neuron to another, while exhibiting a high relative variation in neurons that have high AP shape variability.

3.4 Discussion

Variation of HH α_i and β_i parameters to assess the quantification methods

The voltage-dependent rate constants in the HH model play an essential role in reproducing APs with shapes similar to the ones for experimental recordings of cortical neurons. Although α_i and β_i functions are obtained by fitting the experimental data, they still effectively reflect the overall dynamics of AP generation in neurons [1], [79], [82]. Thus, varying the parameters in α_i and β_i functions affect some AP features such as the rapidity of the AP onset and the AP width [2]. For instance, variation of α_i and β_i parameters of VGSCs' activation and inactivation gates has a higher impact on the rapidity of AP onset than VGdKCs' parameters since VGSCs are responsible for AP initiation (Fig. 3.2A). In contrast, VGKCs are responsible for repolarizing the AP, and hence, variation of α_i and β_i parameters of VGKCs activation gates will have a significant impact on the AP hyperpolarization but a minimal impact in the rapidity of AP onset as shown in (Fig. 3.2B).

Our findings show that the FWHM and HWHM methods for quantifying onset rapidity are more sensitive than phase slope when the VGSCs' parameters are altered, but less sensitive to changes in the VGKCs' parameters, consistent with the general expectations for the roles of sodium and potassium channels. Therefore, varying the α_i and β_i parameters in the HH model provided a good test to examine the sensitivity and specificity of the methods to changes in HH parameters that lead to change in the rapidity of AP onset. Here we show that the FWHM and HWHM methods are better methods than the phase slope method to sense changes in the VGSCs'

activation and inactivation parameters while not being significantly impacted by VGKCs activation parameters.

Advantages of the FWHM and HWHM methods

We have used the FWHM and HWHM methods to quantify the rapidity of AP onset. The choice of these methods is supported by the following reasons. First, the points used to determine the half-width or full width of the \ddot{V} trace are clearly defined without the need for additional numeric parameters, such as the potential at which a slope is to be measured, and thus not sensitive to voltage scaling factors. Second, the FWHM and HWHM methods show a lower variation compared to the phase space slope across neurons of the same type, while showing high variation with neurons exhibiting high AP variability. Finally, since AP initiation is due to the activation of VGSCs, and VGSCs' activation dominates the rising phase of \ddot{V} , the FWHM and HWHM methods can provide a quantification tool to assist investigations into VGSCs activation mechanisms suggested to cause the fast AP onset dynamics in cortical neurons [2], [6], [64].

We showed that double components in experimental APs, which can result in two peaks in \ddot{V} , can lead to a high variation in the FWHM method and the phase space slope method, but it did not impact the HWHM method. However, it should be noted that the second peak in the \ddot{V} traces appeared after the maximum \ddot{V} value for the two AL neurons exhibiting double component AP examined here. Had the first peak not been the maximum \ddot{V} value, the HWHM model could be highly impacted by double component APs. This latter case requires further investigation and likely refinement of the HWHM method.

3.5 Conclusions

We present a novel method to quantify the rapidity of AP onset. The FWHM and HWHM methods are highly sensitive and specific to changes in the VGSCs dynamics compared to the most common method, the phase slope method. The FWHM and HWHM methods, while sensitive to changes in the neurons firing behavior, exhibit only a small variation among regular spiking somatosensory cortical neurons. Thus, the FWHM and HWHM methods can be used to quantitatively study the factors that specifically contribute to AP onset dynamics. These methods can provide a systematic tool that allows direct comparison between experimental data in addition to direct comparison between the AP onset rapidity between different neuron types.

4 NEW METHODS FOR QUANTIFYING RAPIDITY OF ACTION POTENTIAL ONSET

DIFFERENTIATE NEURON TYPES

Preface

This chapter was published in the *PLOS ONE* journal in April 2021 and was co-authored by Aldohbeyb, Vigh, and Lear. Ahmed A. Aldohbeyb's contributions were obtaining electrophysiological recordings from publicly available databases, writing the MATLAB codes, calculating the AP attributes from experimental data, testing AP attributes' ability to classify neuron types, analyzing the data, identifying and describing prior related work, discussing all aspects of the research, conceptualizing many figures and creating all of them, writing the original manuscript, editing text and figures in response to feedback from the other co-authors and outside reviewers, and corresponding with the publisher. This chapter is the same as the published paper, except for minor formatting edits to follow CSU Graduate School formatting and submission guidelines (citation style and tables designs).

Abstract

Two new methods for quantifying the rapidity of action potential onset have lower relative standard deviations and better distinguish neuron cell types than current methods. Action potentials (APs) in most central mammalian neurons exhibit sharp onset dynamics. The main views explaining such an abrupt onset differ. Some studies suggest sharp onsets reflect cooperative sodium channels activation, while others suggest they reflect AP backpropagation from the axon initial segment. However, AP onset rapidity is defined subjectively in these studies, often using the slope at an arbitrary value on the phase plot. Thus, we proposed more systematic methods using the membrane potential's second-time derivative (\ddot{V}_m) peak width. Here, the AP rapidity was

measured for four different cortical and hippocampal neuron types using four quantification methods: the inverse of full-width at the half maximum of the \ddot{V}_m peak (IFWd²), the inverse of half-width at the half maximum of the \ddot{V}_m peak (IHWd²), the phase plot slope, and the error ratio method. The IFWd² and IHWd² methods show the smallest variation among neurons of the same type. Furthermore, the AP rapidity, using the \ddot{V}_m peak width methods, significantly differentiates between different types of neurons, indicating that AP rapidity can be used to classify neuron types. The AP rapidity measured using the IFWd² method was able to differentiate between all four neuron types analyzed. Therefore, the \ddot{V}_m peak width methods provide another sensitive tool to investigate the mechanisms impacting the AP onset dynamics.

4.1 Introduction

The initiation and propagation of action potentials (APs) are key processes of neural communication. Our understanding of the generation of APs advanced greatly by using the Hodgkin and Huxley (HH) model of AP generation. It states that an AP is generated in the giant squid axon due to rapid discharging and recharging of the axon membrane by ionic sodium and potassium currents through a single type of membrane channel for each ion [1]. However, subsequent investigations, aided by continuous improvement of imaging and measurement techniques, clarified that APs recorded from neuronal somas are more complicated than those in the giant squid axon [46]. For example, typical neurons in mammals express voltage-gated ion channels (VGICs) that are permeable to calcium ions in addition to the sodium and potassium channels. Furthermore, the same neuron might express more than a single type of membrane channel for each ion; channels containing various subunits result in differences in biophysical and pharmacological properties [46], [83], [84]. The presence of various VGIC sets across different

neurons causes the shape of the AP to vary significantly in the same animal [85]. This variability in ion channels and the resultant APs adds to the complexity of understanding the role of each type of VGIC in neuronal firing behavior.

Nevertheless, the role of voltage-gated sodium channels (VGSCs) in AP generation is thought to be well defined: the depolarization-induced opening of VGSCs is a critical step in AP initiation. The gating properties of VGSCs of mammalian central neurons are considered to be similar to those in the giant squid axon, including the notion that individual VGSCs open independently upon membrane depolarization [46]. However, several studies in cortical neurons reveal that actual AP initiation appears faster than classical HH-type models predict [2], [5], [6]. Some studies suggested that a more complex gating property of VGSCs (i.e., “cooperative gating”) could be responsible for the deviation from the classic HH-type models [2], [5], [6], whereas others suggested that the discrepancies could be explained by a multicompartmental HH model in which AP backpropagation from the axon can alter the AP onset rapidity in somatic recordings [3]. Several other studies suggested that the rapidity of AP onset is influenced by resistive coupling between the axon and soma [7], [59], and by the size of the dendritic tree [4]. Nonetheless, the ongoing debate on AP initiation mechanisms demonstrates the importance of the topic [2]–[7], [30], [59], [63], [86].

Notably, the method for quantifying AP onset rapidity differs from one study to another. One common approach, the phase-slope method, evaluates the slope of the phase plot, i.e., the first time derivative of the membrane potential (\dot{V}_m) as a function of the potential (V_m), at arbitrary values of \dot{V}_m (ranging from 5 to 50 mV/ms) termed the “criterion level” [2], [7], [8]. Such arbitrary choices of criterion level can confuse and complicate the comparison between different models and experimental data across studies. Another way to analyze AP onset is the error ratio method,

which has been shown to quantitatively differentiate fast-onset APs in rats' cortical neurons from slow-onset APs in snail neurons [9]. Recently, we have shown that the full width at half maximum (FWHM) and the half-width at half maximum (HWHM) of the rising phase of the membrane potential's second-time derivative (\ddot{V}_m) provides systematic and consistent methods to quantify the rapidity of AP onset [27]. Here, we compare these \ddot{V}_m peak width methods [27] to the phase slope [2], [3], [7] and the error ratio method [9] via analysis of onsets of APs recorded from cortical and hippocampal neurons. The results suggest that the two \ddot{V}_m peak width methods of quantifying AP onset rapidity more robustly distinguish between somatosensory cortical neurons and hippocampal neurons in mice than the phase plot slope and error-ratio methods. Overall, we propose that the two \ddot{V}_m peak width methods are sensitive and robust methods to differentiate neuron types based on AP rapidity, and hence might be used as a classification parameter across APs.

4.2 Methods

Data source for AP recordings

Electrophysiological recordings were obtained from two databases. Recordings from the somatosensory cortex were obtained from the GigaScience database [78], whereas recordings from hippocampal neurons were obtained from the CRCNS database [87]. For the somatosensory cortical recordings, the experimental procedures and data are found in da Silva Lantyer *et al.*, 2018 [78]. The analyzed cortical data were from current-clamp recordings of pyramidal regular-spiking (RS) neurons (n=27) and fast-spiking (FS) neurons (n=7) in layers (L2/3) of the primary somatosensory cortex in adult mice. These recordings were obtained and uploaded to the database by Angelica da Silva Lantyer (AL) and were found to be the lowest noise recordings in that database. The recording labels in the database are given in da Silva Lantyer *et al.* Supporting Information [78]. For the hippocampal neurons, the experimental procedures and recordings are

found in Lee *et al.*, 2014 [87], [88]. These current-clamp recordings were made from adult mice hippocampal CA1 neurons. The recordings analyzed here are from 17 RS pyramidal neurons and 6 FS interneurons. The RS pyramidal neurons were further divided into two groups: neurons located in the CA1 superficial sublayer are labeled as superficial pyramidal cells (sPCs) (n=8), and neurons located in the CA1 deep sublayer are labeled as deep pyramidal cells (dPCs) (n=9). Finally, the 6 FS hippocampal interneurons were identified as 6 parvalbumin-positive basket cells (PVBCs).

Recordings included in our analysis had to satisfy criteria regarding numbers and spacing of APs: each current step must have contained at least 2 APs with an interspike interval that was at least 30 ms for RS pyramidal neurons and 12 ms for fast-spiking neurons. The 30 ms limit between RS neurons' APs was set to exclude the variability caused by incomplete deinactivation of the sodium channels [2]. This limit did not exclude many APs since RS neurons firing rate is 32 ± 7 Hz, whereas such a limit can exclude up to half the APs from FS neurons, which have a higher firing rate of 61 ± 9 Hz [89]. Thus, for FS neurons, the lower limit on the interspike interval between APs was set to be 12 ms. That value was chosen because, within the data analyzed here, it was the minimum interval between APs needed to calculate the error-ratio, which requires the AP trace to be fit starting 5 ms to 10 ms before AP onset [9]. The number of AP spikes that satisfied the interspike interval criteria ranged between 58 to 222 APs for each pyramidal cortical neuron recording, between 210 to 514 APs for each FS cortical neuron, between 103 to 182 for each pyramidal hippocampal neuron, and between 80 to 199 for each PVBC. Then, for each AP that fulfilled the above criteria \dot{V}_m and \ddot{V}_m were computed using MATLAB's *diff* function and then interpolated to a resolution of $\Delta t = 1 \mu\text{s}$ using MATLAB's *spline* function unless stated otherwise in the Results section (MATLAB V9.5 (R2019b)).

Quantification of rapidity of AP onset

The rapidity of AP onset was determined using four methods: the inverse FWHM of the \ddot{V}_m peak (IFWd²) [27], the inverse HWHM of the \ddot{V}_m peak (IHWd²) [27], the slope of the curve in the AP phase plot [2], [3], [7], and the error ratio method [9]. The first three methods measure onset rapidity in units of inverse time, while the last method yields a dimensionless value. The IFWd² and IHWd² methods were described previously in [27]. In short, the initial portion of the rising phase of \ddot{V}_m versus time was selected from 3 ms before the AP peak, although this starting point is not critical for the IFWd² and IHWd² calculation, up to the time when \ddot{V}_m drops to zero after peaking. The FWHM and HWHM quantified from the selected \ddot{V}_m portion and the width values, with units of time, were inverted to obtain rapidity. The FWHM was determined to be the time difference between when \ddot{V}_m rises past half the maximum value and when it decays below half the maximum value as shown in Fig. 4.1C. The HWHM was similarly calculated, except the HWHM was defined as the time it takes \ddot{V}_m to rise from half its maximum value to its maximum value (Fig. 4.1C). For the phase slope method, the rapidity was quantified exactly as described in previous studies [2], [3], [7]. The slope of the tangent line in the phase plot at the criterion level of $\dot{V}_m = 10$ mV/ms defines the phase slope rapidity of AP onset for this study, unless a different criterion level is stated.

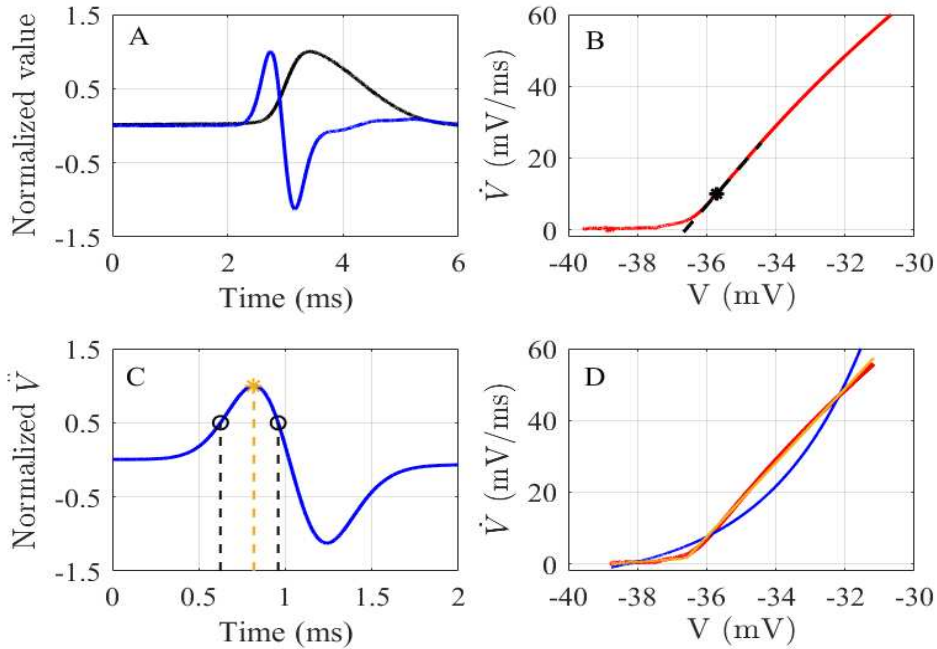


Figure 4.1: The AP rapidity quantification methods. **A)** A normalized AP from a mouse RS somatosensory cortical neuron (black), and its normalized \dot{V}_m . **B)** The initial portion of the phase plot of the same AP in A. The black asterisk indicates the criterion level (10 mV/ms), and the dashed black line represents the phase slope. **C)** The normalized \dot{V}_m of the same AP in A on a smaller time scale. The black circle indicates the points at which \dot{V}_m reaches half its maximum value before and after peaking, while the yellow asterisk represents the maximum normalized \dot{V}_m value. The time between the black dashed lines is the FWHM, and the time between the first black dashed line and the yellow dashed line is the HWHM. The IFWd² and IHWd² are defined as the reciprocal of the FWHM and HWHM, respectively. **D)** The red line shows the selected portion of the phase plot in A. The blue line shows the exponential fit, and the yellow line shows the piecewise linear fit of the selected portion of the phase plot. The error ratio is calculated as the ratio of errors of exponential fit to the piecewise-linear fit.

The final method for quantifying AP onset rapidity was the error-ratio method, which was introduced by Volgushev *et al.* [9]. It was defined as the ratio of the errors for an exponential fit to a two-segment piecewise linear fit (Fig. 4.1D). Volgushev *et al.* specified the fitted portion of the AP trace to be 5-10 ms before the AP onset to the point when either \dot{V}_m reaches 20 to 30% of its maximum value or V_m is 3 to 10 mV above the AP onset voltage. In this study, we choose the 30% \dot{V}_m maximum value as the upper limit unless stated otherwise. The 30% \dot{V}_m maximum value gives enough data points above the onset voltage to capture the upward increase of the AP trace in the phase plot before the rightwards curving of the AP trace toward the maximum value. The ratio

of the exponential fit error to piecewise linear fit error can determine if the AP onset is fast or slow. An error-ratio higher than 3 indicates a sudden, fast onset best fit by two piecewise linear segments, while a ratio below 2 indicates a slow continuous onset best fit by a smoothly increasing exponential curve. Following Volgushev *et al.*'s paper, the data were interpolated using MATLAB *spline* interpolation function. The fitting functions were implemented as described in reference [9], except all three exponential parameters were obtained from a single fitting procedure using the MATLAB *fit* function with a starting estimate for the three parameters rather than the two-step fitting process described by Volgushev *et al.*

Other AP parameters

In addition to analyzing the rapidity of each AP, the onset voltage, amplitude, and width of each AP were also analyzed. The AP onset voltage was taken to be the voltage at which \dot{V}_m reaches 10 mV/ms as defined by Naundorf *et al.* [2]. The AP amplitude was measured as the difference between the membrane voltages at AP onset and the peak voltage, and the spike width was measured as the full width at half the AP amplitude.

Statistical analysis

The mean and standard deviations of rapidity of multiple APs from multiple neurons of the same type were calculated using two statistical approaches: neuron-level pooled statistics using all APs (58-514 per neuron) meeting the selection criteria and conventional statistics on the combined first 50 APs from each neuron. Pooling combines the means or variances for each neuron of a particular type by weighting them by the number of selected APs of each neuron [90]. For conventional statistics, each neuron of a given type was effectively weighted equally in that each one contributed 50 APs to the combined sample and no mean or standard deviation was computed for individual neurons. After calculation of the pooled and conventional means and standard

deviations, the relative standard deviation (RSD), which is defined as the ratio of the standard deviation to the mean for each neuron type was calculated using the values from the two statistical approaches. Pairs of neuron types were then compared using two-tailed Student's t-tests, the Mann-Whitney U test, and effect size using two test methods; Cohen's d and common language effect size (CLES) [91]. While both the t-test's t-score and the Mann-Whitney U-test z-score are enhanced by the large AP sample sizes (hundreds of spikes), the effect size is not. Thus, the first two reflect statistical differences in the mean rapidity of neuron types, and the latter one provides an indication of the ability to classify individual neurons.

4.3 Results

Comparison between the AP rapidity quantification methods

4.3.1.1 Somatosensory cortical neurons

The recordings from cortical neurons were analyzed to determine the mean and standard deviation of AP rapidity using the four quantification methods for each RS and FS neuron's spike train; values are plotted in Fig. 4.2. When comparing the mean rapidity for each type of neuron of, the IFWd² and IHWD² methods show the lowest variation within each neuron type compared to the other methods. The cell-to-cell conventional RSD of the spike train rapidity measured using the IFWd² method was 22.2% for RS neurons and 14.7% for FS neurons. Corresponding RSDs using the IHWD² method were 18.2% and 15.7%, respectively. The phase slope method gave higher relative variation with RSDs of 33.4% and 16.7%, respectively. The error-ratio method produced yet higher variation across the same neuron type with 104% and 81.4% RSDs, respectively, for RS and FS neurons. Table 4.1 summarizes the conventional mean and standard deviation of each rapidity quantification method as well as other electrophysiological properties

for RS and FS neurons. Furthermore, the choice of either conventional or pooled statistics did not alter the basic results. Using the pooled statistics, the \dot{V}_m peak width methods still show the smallest relative variation among the AP rapidity calculations methods (Table S1).

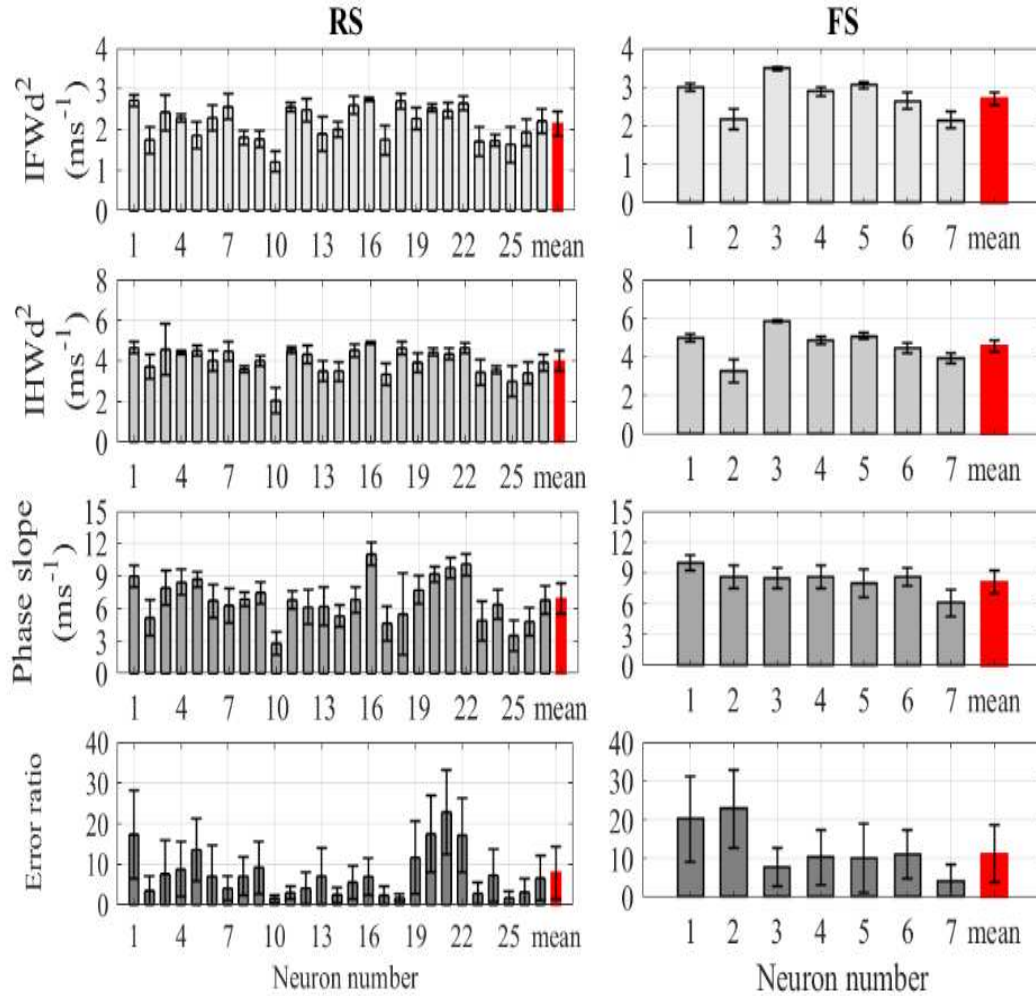


Figure 4.2: The AP rapidity calculated using the four quantification methods for cortical neurons. Comparison between the rapidity quantification methods for RS pyramidal cortical neurons (left) and FS cortical neurons (right). The units for IFWd², IHWd², and phase slope are in ms⁻¹ while the error-ratio is dimensionless. Error bars indicated standard deviations for each neuron. The red bar at the end of each figure indicates the pooled mean value for all neurons and its error bar indicates the pooled standard deviation.

Table 4.1: Electrophysiological properties using conventional mean and standard deviation

	Cortex		Hippocampus	
	RS (pyramidal)	FS	RS (pyramidal)	FS (PVBCs)
Number of neurons	27	7	17	6
IFWd² (ms⁻¹)	2.2 ± 0.5	2.9 ± 0.4	4.7 ± 0.8	6.8 ± 0.5
IHWd² (ms⁻¹)	4.1 ± 0.7	4.8 ± 0.8	7.9 ± 1.9	12.0 ± 1.1
Phase Slope (ms⁻¹)	7.1 ± 2.4	8.6 ± 1.4	70.7 ± 103.5	12.6 ± 7.7
			46 ± 19.4 ^a	13.6 ± 7.5 ^a
Error ratio (dimensionless)	8.7 ± 9.0	13.2 ± 10.8	7.7 ± 3.2	0.8 ± 0.6
			7.4 ± 3.4 ^b	8.6 ± 3.2 ^b
Amplitude (mV)	64.3 ± 12.3	61.1 ± 3.9	72.7 ± 7.1	48.3 ± 6.7
Width (ms)	1.9 ± 0.6	0.7 ± 0.1	1.3 ± 0.2	0.3 ± 0.03
Onset potential (mV)	-28.3 ± 9.9	-39.2 ± 7.1	-33.4 ± 3.4	-33.1 ± 2.4

All data expressed as mean ± SD. ^a using piecewise cubic interpolation. ^b the upper limit was set to 3 mV above the AP onset. The number of APs used to obtain the mean and SD values are 1350 for RS cortical neurons, 350 for FS cortical neurons, 850 for RS hippocampal neurons, and 300 for FS hippocampal neurons.

4.3.1.2 Hippocampal neurons

The analysis of the hippocampal neuron recordings also showed that the IFWd² and IHWd² methods had much lower RSD than either the phase slope or error ratio methods, as seen in Fig. 4.3. Also, as shown in Table 4.2, despite the slightly lower rapidity of superficial pyramidal neurons compared to the deep pyramidal neurons, none of the methods shows a statistically significant difference between superficial and deep neurons using pooled statistics. Thus, all the

hippocampal pyramidal neurons, despite their varying location, were treated as the same cell population (Table 4.1).

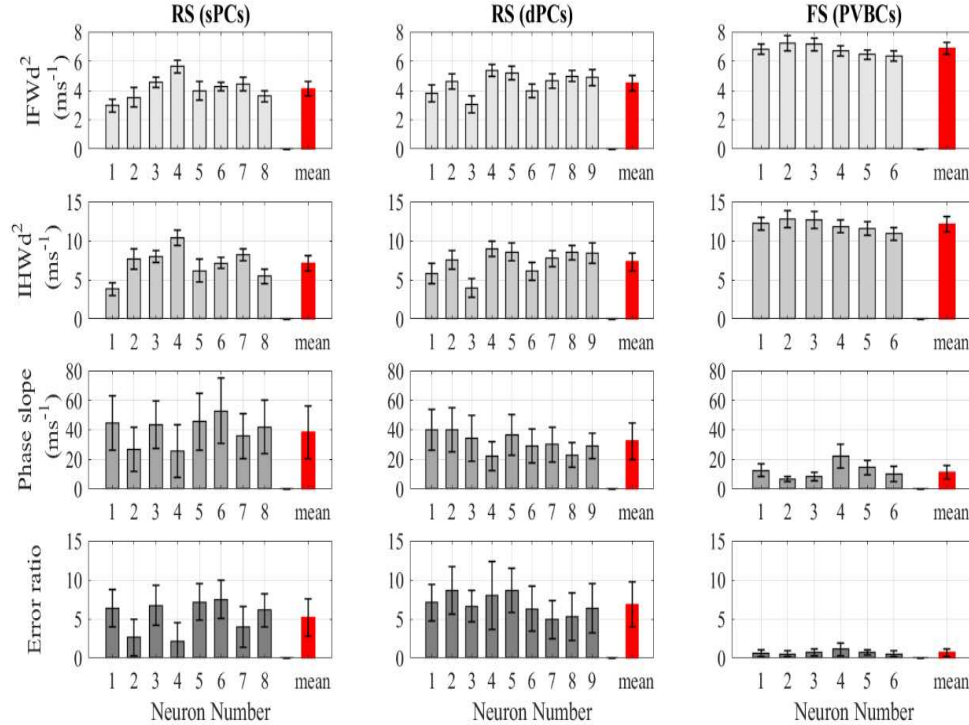


Figure 4.3: The AP rapidity calculated using the four quantification methods for hippocampal neurons. Comparison between the onset rapidity quantification methods applied to hippocampal neuron APs. All the values here are obtained using the spline interpolation function except for phase slope values, which were obtained using the pchip interpolation function.

The hippocampal neuron’s conventional RSD of the spike train rapidity measured using the IFWd² method was 17.4% for RS pyramidal neurons and 8.0% for FS PVBCs. Corresponding RSDs using the IHWd² method were 24.4% and 9.6%. The error ratio method had a high relative variation with RSDs of 42.0% and 73.3%, respectively. For the hippocampal neurons, the phase slope method produced the highest variation with 147.9% and 61.2% RSDs, respectively, for RS pyramidal neurons and FS PVBCs. Strikingly, the \ddot{V}_m peak width methods indicate that the FS PVBC have more rapid onset than the RS neurons, similar to the cortical neuron results, while the error ratio and the phase slope methods gave the opposite relation. The error ratio’s much smaller mean and SD values for FS hippocampal neurons can be attributed to the data selection, which is

discussed in a following section. Also, the high variation in the phase slope value was due to low sampling rates, motivating the adoption of a different interpolation function for further analysis using the phase slope method as discussed in the next section.

Impact of sampling rate and interpolation method

Sampling rates used during data acquisition and interpolation formulas impact AP onset rapidity, especially when quantified with the phase slope or error ratio methods. For hippocampal RS pyramidal neuron recordings, the phase slope method produced high standard deviations, which can be attributed to the sampling rate of the recordings and the interpolation function. The sampling rate for the hippocampal recordings was 10 kHz, giving one data point every 100 μ s. In contrast, the sampling rate for the cortical recordings analyzed in this paper was 20 kHz. The lower sampling rate (i.e., the longer time between consecutive samples of V_m in hippocampal recordings) results in only a few data points during the rising phase of the AP. Although such a lower sampling rate is acceptable to reconstruct most AP details with high fidelity, high precision analysis of AP onset dynamics benefits from faster sampling rates and accurate interpolation. Consequently, the choice of interpolation function can impact the value of the AP rapidity, especially when evaluating the phase slope at a specific criterion level in the phase plot.

Spline interpolation can cause significant excursions, i.e., bowing between two measured data points resulting in a huge variation in the phase slope rapidity from one AP to another in the same spike train. Such excursions were apparent in 3 pyramidal neuron recordings and caused the high standard deviation value for the phase slope method given in Table 4.2. Thus, the piecewise cubic interpolation function (the function *pchip* in MATLAB R2019b) was used to interpolate the pyramidal hippocampal neuron recordings. Table 4.3 shows a comparison of the mean and standard deviations of AP onset rapidity for the two interpolation methods in combination with

each rapidity quantification method. Using the cubic piecewise interpolation function substantially reduced both the mean and standard deviation values obtained using the phase slope method. Such a significant reduction in the phase slope values is expected since the slope is calculated at a specific criterion level (at 10 mV/ms) of the dependent (vertical axis) variable in phase space plots. As soon as an interpolated value of the dependent variable, \dot{V}_m , is at or above the chosen criterion level, the neighboring data points are used to find the tangent line (i.e. the slope) on the phase plot. This can occur prematurely if the spline interpolation reaches dependent values greater than either data point. Unlike the spline interpolation, the cubic piecewise (*pchip*) interpolation never produces an excursion beyond the data points between which it is interpolating, and hence the variation in the phase slope values decreased when *pchip* interpolation was employed. However, for the error-ratio method, *pchip* interpolation increased the mean and standard deviation of AP rapidity values by more than 40% compared to spline interpolation. This increase in the error ratio can be primarily attributed to the increase in the exponential fit error. Unlike the cubic piecewise interpolation function, the cubic spline interpolation function has a smooth transition between the points, which causes a better overlap between the interpolated AP portion and the exponential fit. Hence, the mean square error will be lower with spline interpolation than that with cubic piecewise interpolation.

In contrast, the IFWd² and IHWD² mean values are minimally affected by the choice of the interpolation function with less than a 5% difference. While changing the interpolation functions altered the standard deviation of rapidity for the IFWd² method by less than 1%, the IHWD² standard deviation roughly doubled. The higher variation in IHWD² values occurs because, in a few recordings, the peak of \ddot{V}_m can be missed and partially truncated by the piecewise cubic

function (Fig. S4). Regardless of the interpolation function, the IFWd² and IHWd² methods show consistent mean values and smaller variation across the same neuron type.

Table 4.2: the mean and standard deviation of rapidity for RS hippocampal neurons using pooled statistics

Interpolating function	Cell type	IFWd² (ms⁻¹)	IHWd² (ms⁻¹)	Phase slope (ms⁻¹)	Error ratio (dimensionless)
Spline	dPCs (n = 9)	4.5 ± 0.5	7.3 ± 1.2	43.3 ± 38.9	6.8 ± 2.9
	sPCs (n = 8)	4.1 ± 0.5	7.1 ± 1.0	53.4 ± 86.7	5.2 ± 2.4
Piecewise cubic	dPCs (n = 9)	4.3 ± 0.4	7.2 ± 1.7	32.2 ± 12.4	8.1 ± 4.0
	sPCs (n = 8)	4.0 ± 0.5	7.4 ± 2.2	38.5 ± 17.8	6.55 ± 3.8

Impact of phase slope criterion level

The rapidity determined by the phase slope method appears to depend on the criterion level at which it is calculated [7], [63]. Typically, the criterion level should be set to be in the linear region just above “the kink” and higher than the baseline noise [2], [3]. If onset is characterized by a phase plot that is linear over a wide range of \dot{V}_m values, changing the criterion level will not significantly alter the phase slope and thus the rapidity. However, if the phase plot is non-linear or has multiple linear segments just above AP onset, or the criterion level was set very close to the onset kink, then the phase slope value will depend on the chosen criterion level. For example, varying the phase slope criterion level from 10 to 40 mV/ms resulted in less than a 20% change in mean rapidity for hippocampal RS pyramidal neurons. Such a small change is expected since the phase plot is nearly linear over the chosen range, as shown in Fig. 4.4B for a typical case. However, for the hippocampal FS PVBCs, varying the \dot{V}_m criterion level caused the phase slope to increase significantly, as shown in Fig. 4.4D. The 10 mV/ms criterion level is near the transition between the baseline and the vertical rise of the phase plot. Thus, the PVBCs phase slope measured at 40

mV/ms is almost 4 times larger than the value measured at 10 mV/ms (Fig. S5). Nonetheless, when the phase slope is measured in a single linear range, for example above 25 mV/ms for the FS PVBCs, the phase slope values are more consistent. Notably, changing the criterion level reversed the relative rapidity between the hippocampal RS pyramidal neurons and the FS PVBCs (Fig. S5). In contrast, the mean rapidity of AP onset of cortical FS neurons was always greater than the mean rapidity of RS neurons as quantified by the phase slope method over the full 10 to 40 mV/ms criterion level range.

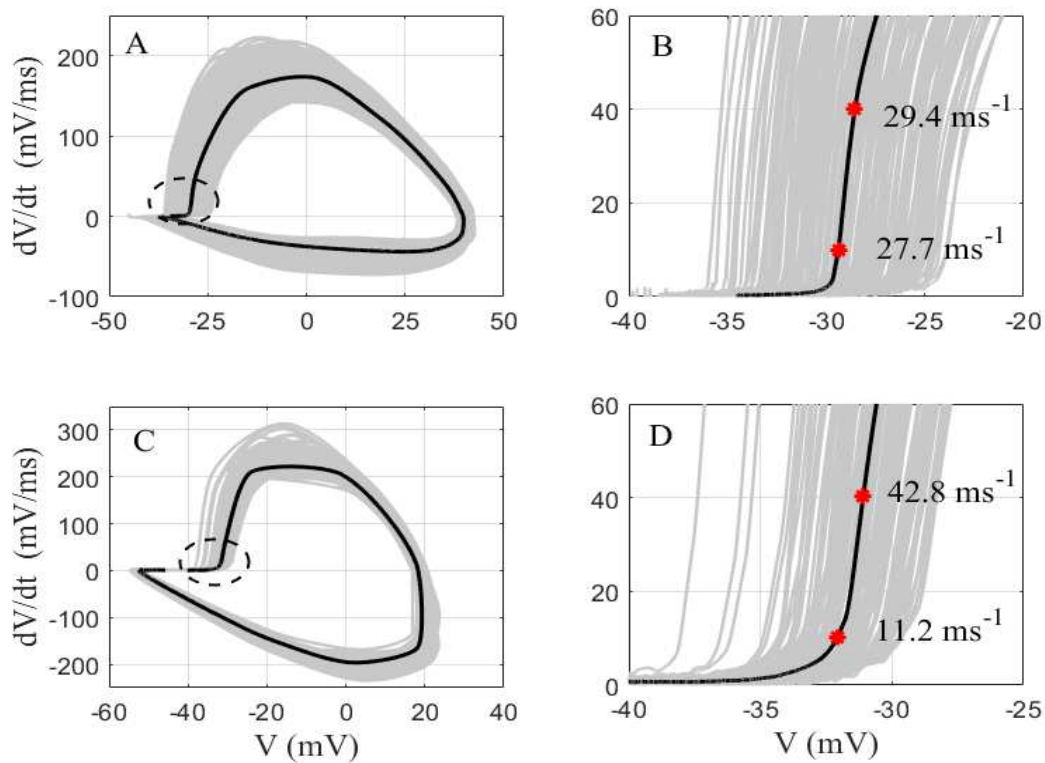


Figure 4.4: Comparison of the impact of the phase slope criterion level between a hippocampal pyramidal neuron and a hippocampal PVBC. **A:** A cumulative phase plot of the APs from a hippocampal pyramidal neuron (gray), and their average (black). **B:** The portion of the phase plot of A near onset. **C:** A cumulative phase plot of the APs from a hippocampal PVBC (gray), and their average (black). **D:** The portion of the phase plot of C near onset. The red asterisks in C and D represent the points at which the average \dot{V}_m reached 10 mV/ms and 40 mV/ms, and the values next to the asterisks are the phase slopes at those points.

Impact of data selection limits on error ratio method

Volgushev *et al.* used the error ratio to distinguish between rapid rat cortical neurons (error ratio > 3) and slow onset snail neurons (error ratio < 2), but a few percent of the neurons in their analysis would be incorrectly categorized by the error-ratio method. They found 49 cortical neurons had an average error ratio of 8.46 ± 3.87 with all neurons except one having a value above 3 [9]. In contrast, 29 snail neurons had an average error ratio of 0.96 ± 0.57 , with all neurons except two having a value below 2 [9].

Mean values similar to those obtained by Volgushev *et al.* [9] were observed in the cortical data analyzed here, as shown in Table 4.1. However, consistent with the high value of the standard deviation in this analysis, 7 of the 27 RS cortical neurons had an average error ratio below 3 as seen in Fig. 4.2, which would categorize them as having slow onsets. This low error ratio for these 7 RS cortical neurons can be attributed to the recording noise, which can bias the error ratio value lower toward one, and the selection of the range of the AP trace that is used for the fit [63]. Varying the data selection limits significantly impacts the error ratio of the neurons analyzed in this study. Changing the upper limit from 30% of \dot{V}_m maximum value to 3 to 10 mV above the onset potential increased the error ratio of the 7 previously miscategorized RS neurons, so that 6 out of the 7 have an error ratio higher than 3 using this alternative upper limit. The only neuron maintaining an error ratio below 3 after altering the upper limit is the neuron showing the slowest AP onset by all the quantification methods (RS neuron number 10 in Fig. 4.2). A comparison of the impact of the data selection limits on two neurons is shown in Fig. S3. Furthermore, similar to the results from cortical neurons, the error ratios for the FS interneurons will shift from below 1 to above 3 as the portion of the AP data selected for fitting is varied. Changing the upper limit to be 3 mV above onset changed the error ratios for PVBCs to be 8.5 ± 2.8 (All values are presented as mean \pm SD).

While the other quantification methods do not depend on the data selection limits, the error ratio value can be significantly impacted by the limits of the data selection. Thus, the subsequent classification of a neuron as having slow or fast AP onset depends on the data selection when using the error ratio method.

Classification of neuron types based on AP rapidity

4.3.1.3 Differences in onset rapidity between RS and FS neurons

Differences in the AP shapes of RS and FS cortical neurons, including quantitative features such as the AP width and amplitude, are well-known from the literature [11], [85], [89]. However, in prior studies, the AP onset rapidity has not been reported as one of the AP features used to differentiate RS from FS cortical neurons. Here, the results show that the AP onset rapidity is significantly different between RS and FS neurons, and hence provides another measure to differentiate between the two neuron classes. Based on mean rapidities of the above two populations of neurons as shown in Table 4.1 and Table 4.3, FS cortical neurons have significantly higher rapidity than RS cortical neurons using all the quantification methods. However, the IFWd² and IHWd² methods have the highest scores of all methods in Table 4.3 according to all three statistics. The nonparametric, Mann-Whitney test, indicated all the AP quantification methods show a significant difference between RS and FS cortical neurons, as reflected in a z-score > 6 (Table 4.3).

The results from hippocampal neurons show similar patterns. For example, the FS PVBCs have AP onset that is 60 % more rapid than pyramidal neurons based on analysis using the IFWd² method. However, the RS neurons mean rapidity was higher than the FS neurons mean rapidity in the hippocampus as quantified by the phase slope method using *spline* or *pchip* interpolation functions with a criterion level of 10 mV/ms and the error ratio method with the original upper

limit set to 30% of the maximum \dot{V}_m . This relationship is denoted with a negative sign on all three statistical measures in Table 4.3, and reversed from what was found in the cortex, and thus expected in the hippocampus. Changing the upper limit on data selection for the error ratio method returned the mean FS rapidity to being larger than the mean RS rapidity in the hippocampus but resulted in degrading the effect size. Cohen's d , for comparison, decreased from large effect size of 2.47 to 0.36, a medium effect size. No reversal of FS and RS rapidity between cortex and hippocampus was observed for the IFWd² and IHWd² methods regardless of the interpolation technique.

In addition to AP rapidity, Table 4.3 summarizes how well AP amplitude, width, and onset potential differentiate RS and FS neuron recordings in this study. For both cortical and hippocampal neurons, a significant difference between RS and FS neurons is observed in all the AP parameters analyzed here except the AP onset potential between RS and FS hippocampal neurons. As shown in Table 4.1, the FS neurons, on average, have smaller AP amplitude, narrower AP width, lower onset voltage, and faster AP rapidity compared to the RS pyramidal neuron.

Together, results from the cortical and hippocampal neurons indicate that AP rapidity is clearly different between RS and FS neurons using parametric and nonparametric statistical tests (Table 4.3). The differences in rapidity using the \dot{V}_m peak width methods were not only significant as indicated by p -values but also have the largest effect size. As shown in Table 4.3, the only AP properties that produced an effect size larger than the IFWd² method in any of the comparisons is AP width in the intracortical and intrahippocampal comparisons and AP amplitude in the intrahippocampal comparison. AP width is known as providing a clear difference between RS and FS neurons [11], [85]. Both IFWd² rapidity and AP width score in the large effect size range.

Therefore, the rapidity of AP onset can be used as another electrophysiological property to differentiate between these classes of neurons.

Table 4.3: Comparison between electrophysiological properties of four neuron types using conventional statistics

	Cortical FS and RS neurons			Hippocampal FS and RS neurons			Hippocampal and cortical pyramidal neurons		
	t	z	Cohen's d (CLES)	t	z	Cohen's d (CLES)	t	z	Cohen's d (CLES)
IFWd² (ms⁻¹)	24.9	20.0	1.36 (0.84)	49.6	25.3	2.77 (0.98)	79.8	39.4	3.89 (1.0)
IHWd² (ms⁻¹)	16.2 ^c	15.6	0.97 (0.75)	43.5	24.4	2.31 (0.97)	55.6	35.6	2.89 (0.97)
Phase Slope (ms⁻¹)	14.7	10.9	0.67 (0.70)	-16.0	-24.9	-0.64 (-0.71)	17.7	39.1	0.98 (0.72)
				-40.8 ^a	-24.2 ^a	-1.89 ^a (-0.94 ^a)			
Error ratio (dimensionless)	7.3	9.4	0.48 (0.62)	-59.4	-25.5	-2.47 (-0.98)	-3.8	-6.2	-0.14 (-0.54)
				5.3 ^b	6.4 ^b	0.36 ^b (0.60 ^b)			
Amplitude (mV)	-8.1	-6.3	-0.29 (-0.60)	-51.8 ^e	-25.5	-3.48 (-0.99)	20.2	16.7	0.79 (0.72)
Width (ms)	-71.4	-28.9	-2.34 (0.98)	-133	-25.8	-5.54 (-1.0)	-40.2	-36.1	-1.46 (-0.87)
Onset potential (mV)	-23.3	-18.6	-1.16 (0.81)	1.9 ⁿ	1.2 ⁿ	0.11 (0.53)	-17.6	-14.8	-0.64 (-0.69)

Student's t test and Mann-Whitney test were performed to compare neuron types, and Cohen's d and common language effect size (CLES) were used to measure the effect size. For the t-score, ^c indicates that the equal variance hypothesis was accepted, however, the unequal variance t-score was within 4% within both cases. ⁿ the difference is not significant; otherwise, the difference is significant (p<0.05). ^a using piecewise cubic interpolation. ^b the upper limit was set to 3 mV above the onset. ^c using piecewise cubic interpolation for hippocampal pyramidal neurons and cubic spline for cortical pyramidal neurons. The minus sign indicates that the RS neuron's mean was higher than the FS neuron's mean, and the cortical pyramidal neuron's mean was higher than hippocampal pyramidal neuron's mean.

4.3.1.4 Differences in onset rapidity between cortical and hippocampal pyramidal neurons

Pyramidal neurons are the most abundant excitatory neurons found in most mammalian forebrain areas such as the cerebral cortex and the hippocampus [92]. Pyramidal neurons in different areas have some family resemblance, but they vary in their morphology and behavior [93]. For example, a study showed that cortical pyramidal and CA1 hippocampal pyramidal neurons have similar Na^+ entry ratio and AP amplitude, but different AP width [94]. Therefore, differences between cortical and hippocampal pyramidal neuron AP onset rapidity, as well as the other AP parameters, are of interest.

AP onset rapidity is significantly different between cortical and hippocampal pyramidal neurons. Using the IFWd² method, the rapidity of hippocampal pyramidal neurons is more than double the rapidity of cortical pyramidal neurons. A very clear difference in rapidity is observed using all the quantification methods as shown in Table 4.3. Furthermore, comparing other electrophysiological properties revealed a significant difference between hippocampal and cortical pyramidal neurons in amplitude, onset potential, and width. The width of cortical neuron APs was more than 35% wider than those of the hippocampal neurons, which is typical [94]–[97]. Notably, the IFWd² method provided the highest significant difference among all the rapidity methods used in this analysis. Also, the \dot{V}_m peak width methods showed a significantly larger effect size compared to the other AP rapidity methods as shown in Table 4.3.

Double peaks in the rising phase of the \dot{V}_m trace, which have been associated with AP backpropagation in central mammalian neurons, were observed in a small minority of the analyzed APs and resulted in significantly lower rapidity than single-peaked \dot{V}_m traces in the rising phase. The double-component AP is characteristic of signal backpropagation from the AP initiation site [3], [9]. However, less than 7% of APs analyzed in this study had a clear shoulder or dip that

corresponded to the double-component AP as examples given by Volgushev *et al* [9]. No FS neurons in the dataset exhibited a double-component AP. The rapidity of double-component APs was statistically significantly smaller than for single-component APs. The difference in rapidity of single and double component APs was most significant using the IFWd² method (cortex: Mann-Whitney Z = 12.8, p<0.0001, CLES = 0.79, hippocampus: Mann-Whitney Z = 23.2, p<0.0001, and CLES = 0.97). Similarly, the mean double-component rapidity found using the IHWd² and phase slope methods was less than the mean rapidity for single-component APs, but the level of significance and effect size was smaller or in some cases insignificant as shown in Table 4.4.

Table 4.4: Comparison between single-component and double-component APs

Neuron type	Cortical pyramidal neuron				Hippocampal pyramidal neuron			
	single	double	Z	Cohen's d (CLES)	single	double	Z	Cohen's d (CLES)
\ddot{V}_m peaks								
IFWd ² (ms ⁻¹)	2.2 ± 0.5	1.5 ± 0.6	12.8*	1.35 (0.79)	4.6 ± 0.8	2.9 ± 0.4	23.2*	2.17 (0.97)
IHWd ² (ms ⁻¹)	4.0 ± 0.7	3.6 ± 1.7	0.95	0.58 (0.52)	7.8 ± 1.8	3.9 ± 1.3	22.4*	2.25 (0.96)
Phase Slope (ms ⁻¹)	7.0 ± 2.2	5.3 ± 2.9	6.5*	0.73 (0.65)	34.4 ± 16.9 ^a	32 ± 13.5 ^a	0.93	0.14 (0.52)

Z-score from Mann-Whitney test were used to compare AP waveform, Cohen's d and common language effect size (CLES) were used to measure the effect size. ^ausing piecewise cubic interpolation. * the difference is significant (p<0.0001).

4.4 Discussion

The results presented above not only support the \ddot{V}_m peak width methods as improvements on existing methods of quantifying AP onset rapidity, but also support their utility in categorizing

types of neurons. The \ddot{V}_m peak width methods can capture the difference in AP rapidity between different neuron types while showing smaller relative variation across the same neuron type than prior methods. Therefore, the \ddot{V}_m peak width methods can be used to classify different neuron types and hence enable quantitative analysis of factors impacting AP onset dynamics.

The AP rapidity quantification methods

The results from the IFWd² and IHWd² methods are more reliable measures of AP rapidity than the other methods for two primary reasons. First, the points at which the rapidity values are calculated are well defined and don't require arbitrary choices of parameters. The IFWd² and IHWd² are measured at specific points on the \ddot{V}_m trace, where the location of those points is defined using only their values relative to the peak value of \ddot{V}_m without requiring an arbitrary or unscaled value or being influenced by extending the range of data analyzed. Unlike the IFWd² and IHWd² methods, the phase slope is measured at an arbitrary value on the phase plot, which differs from one study to another, while the error-ratio value depends on the portion of the AP recording selected for fitting. Thus, the IFWd² and IHWd² methods provide more consistent rapidity values that simplify comparison between different studies. Second, the second derivative peak width methods provide rapidity values that are independent of the definition of AP onset. The determination of AP rapidity, AP onset voltage variability, and the relationship between them are subjects of interest and great debate in many studies [2], [59], [63], [64]. The widely used phase slope method defines the AP onset voltage and rapidity at the same value of the phase slope. Shifting the criterion level at which the slope was measured was shown to have little effect in cortical neurons but can cause a large shift in the rapidity in computational models [7], [63]. However, shifting the criterion level can alter the results when the AP has a smooth onset [63], or when the \ddot{V}_m value is in close proximity to the kink. As a result, the phase slope value tripled when

the criterion level was shifted from 10 mV/ms to 40 mV/ms. Furthermore, the comparison in Table 4.2 shows that the choice of interpolation function significantly influences the interpolated phase slope, leading to different rapidity values for many APs. While the onset voltage might not be significantly impacted by the choice of the interpolation function, the slope often is. The slope is more sensitive to excursions that can occur in the spline fit, while the onset voltage variability in this steep part of the phase space plot would be limited. As a result, the choice of the interpolation function could cause high variation in the phase slope that does not reflect the real differences in rapidity, which might in turn influence the analysis of the relationship between AP rapidity and threshold variability.

While the IFWd² and IHWd² are more reliable methods on good recordings, they are susceptible to noise, which is more pronounced when computing the second derivative. Noise can also introduce uncertainty in the peak position of the rising phase. Thus, analysis of a noisy recording requires the data to be filtered before calculating the IFWd² and IHWd². Nonetheless, the noise in the recordings analyzed here was quite small, and thus the calculation of the IFWd² and IHWd² was done without using any noise filters.

Factors affecting AP onset rapidity

APs in central mammalian neurons have sharper and more abrupt onset compared to invertebrate neuron APs. An initial proposal to explain the “kink” in cortical neuron APs was introduced by Naundorf *et al* (2006), where cooperative VGSCs gating was proposed to explain the sharp AP onset in cortical neurons. Naundorf *et al.* showed that the rapid AP onset and the variability of AP onset observed in cortical neurons can be replicated using a cooperative VGSC model instead of a canonical HH model, which failed to reproduce these two features [2]. However, an alternative explanation was introduced by Yu *et al.* (2008) showing that the two

features can be replicated using a multicompartment HH model without the need for cooperative VGSC gating, an explanation which was supported by patch-clamp recordings obtained from the soma of cortical neurons as well as from axonal bleb. They showed that the sharp somatic AP onset in cortical neurons is influenced by the distance from the axon initial segment (AIS) to the soma, with the rapidity increasing as the AP propagated away from the AIS and become biphasic [3]. Therefore, AP rapidity can indicate distance between the somatic recording site and the AP initiation site, where neurons exhibiting lower AP onset rapidity indicate that the AP was initiated closer to the soma [98]. However, double-component APs were present in only a small portion of the APs analyzed here, and in those double-component APs, the rapidity was smaller compared to single-component APs, indicating that the AP backpropagation did not lead to an increase in neuron rapidity in this study. The analysis here agrees with Volgushev *et al's* (2008) results where APs with double-components had a lower rapidity than single-component APs, although their results did not show a significant difference between the two groups in cortical neurons. While AP backpropagation can contribute to the sharpness of the somatic AP, it was found that the AP backpropagation is necessary but not sufficient alone to reproduce the observed kink in cortical neurons [63].

Subsequent to publication of the AP backpropagation and cooperative gating theory, neuron geometry was proposed to explain the sharp AP rapidity observed in central mammalian neurons. In 2013, Romain Brette demonstrated theoretically that the abrupt AP onset observed in cortical neurons could be due to a different mechanism elucidated in resistive coupling theory [59]. The theory states that Na^+ current originating in the AIS is primarily sunk by the soma, due to its large size, and subsequently exits as capacitive current. Hence, the neuron geometry significantly influences the sharpness of the AP [7], [59], [99]. Other studies similarly confirmed the role of

neuron size by demonstrating the large impact of dendritic tree size on AP rapidity [4], [100]. Eyal *et al.* (2014) showed, using computational models, that rapidity increased by 30% when the axon-to-somatodendritic conductance ratio was increased from 12 to 370, and increased by 450% when the ratio was altered in the presence of ultrafast VGSC kinetics [4], which might also indicate the importance of specific VGSC subtypes. For example, while both the somatosensory cortex and hippocampus express similar VGSC subtypes, Nav1.1, Nav1.2, Nav1.3, and Nav1.6, the level of expression differs [101], which could be one of the factors contributing to the difference in rapidity between pyramidal neurons in the two regions. Moreover, another direct explanation of the difference in rapidity can be attributed to input resistance. For instance, the slower rapidity in cortical pyramidal neurons, compared to that in hippocampal pyramidal neurons, could be attributed to the higher input resistance of cortical pyramidal neurons [102], [103]. Nonetheless, these studies indicate the complexity of factors mediating the rapidity and highlight the importance of a better and sensitive tool to measure the impact of these factors on AP rapidity.

The second derivative peak width methods for neuron classification

The ability to distinguish different neuron types is essential for understanding neuronal circuits and functions. Cortical and hippocampal neurons have been classified based on different properties such as morphology, location, and electrophysiological properties. Here, as shown in Fig. 4.5, the rapidity of AP onset can also be used to differentiate various neuron types. Analysis of the rapidity shows a significant difference between RS and FS neurons both in the somatosensory cortex and the CA1 hippocampus, and between cortical and hippocampal pyramidal neurons. These results agree with a previous study using the phase slope method that showed a significant difference in AP rapidity between two cell types, CA3 pyramidal neurons and dentate granule neurons [98]. Here, the \ddot{V}_m peak width methods provide better separation

between different cell types compared to the phase slope and the error ratio methods based on parametric and non-parametric statistical tests. The cortical and hippocampal recordings used in this study were obtained from two different research groups, and thus the recording and preparation conditions might contribute to the different rapidity between the two brain regions. However, the results from these datasets reproduced relationships of other AP parameters such as amplitude and width between cortical and hippocampal pyramidal neurons found in a previous study [94]. Carter and Bean (2009) reported that cortical pyramidal neurons had wider and slightly higher amplitude APs than those recorded from hippocampal pyramidal neurons [94]. While varying experimental conditions could influence conclusions about the relative rapidity of hippocampal and cortical pyramidal neurons, it would be expected to have a similar effect on all rapidity quantification methods. Therefore, the IFWd² method is expected to still better quantify any differences between hippocampal and cortical neuron rapidity than the other methods, as shown in Table 4.5.

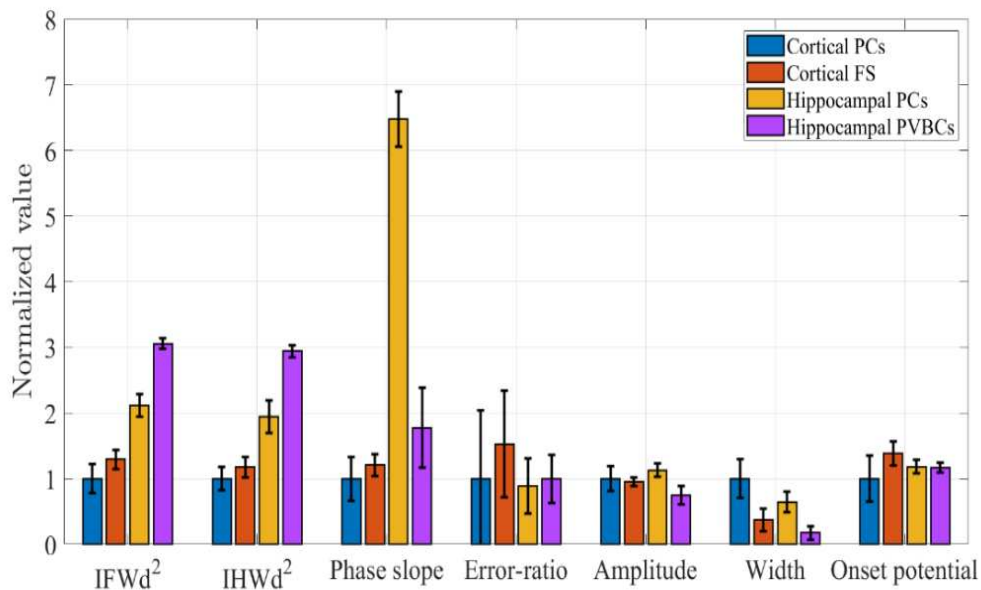


Figure 4.5: Comparison of the electrophysiological properties of all the neurons analyzed in this study. The vertical axis represents the values normalized to the mean value for cortical pyramidal neurons, and the error bar represents the RSD for each neuron population. The phase slope value for hippocampal pyramidal cells is obtained using pchip interpolation, and the error ratio value for PVBCs are obtained with the upper limit was set to 3 mV above the onset.

Table 4.5: Two-tailed p-value from the t-score between the IFWd² values from different neuron types, and Cohen’s d effect size (in parentheses). Green cells indicate a p-value below 0.05.

IFWd ²		Cortex		Hippocampus	
		PCs	FS	PCs	PVBCs
Cortex	PCs		<0.0001 (1.36)	<0.0001 (3.89)	<0.0001 (9.07)
	FS	<0.0001 (1.36)		<0.0001 (2.52)	<0.0001 (8.13)
Hippocampus	PCs	<0.0001 (3.89)	<0.0001 (2.52)		<0.0001 (2.77)
	PVBCs	<0.0001 (9.07)	<0.0001 (8.13)	<0.0001 (2.77)	

“PCs” indicates pyramidal cells, and “PVBCs” indicate parvalbumin-positive basket cells.

Sodium channel parameters affect modeled rapidity

Parameters of AP features have been correlated to differences in voltage-gated ion channel subtypes, such as the connection between VGKCs and AP width. In this study, the other AP feature that provides a good separation between the different neuron types is the AP width (Table S2). The significant difference in the AP width between all the neuron types analyzed here is consistent with a difference in the types and densities of potassium channels expressed in these neurons since the AP width is mainly determined by VGKCs [46], [94], [104]. The significant difference in AP width is evidence of the key role of different VGKCs types whose activation and inactivation control many aspects of AP waveforms [46], [104]–[106].

In contrast to the variation in VGKCs associated with AP width, the activation of VGSCs has been proposed to be similar for hippocampal interneurons and their principle counterparts, pyramidal neurons [105]. Furthermore, some investigations have even shown that the gating properties of mammalian central neurons are similar to those in the giant squid [46]. Although several studies have shed light on the differences in VGSC kinetics between different neuron types, the role of VGSC activation in AP initiation is thought to be similar since the slope factor and time course of VGSCs was comparable [107]. Such conclusions agree with other studies in cortical

neurons that show the rate of maximum rise was indistinguishable between RS and FS neurons [11], [85], indicating similar densities and behavior of sodium channel activation in both RS and FS cortical neurons. However, several other studies have argued that the fast AP onset observed in cortical neurons are due to cooperative VGSC activation, as evident by the high rapidity measured using the phase slope [2], [5], [6]. Whether the studies supported the role of VGSC activation, such as those proposing cooperative activity, or found no differences in VGSC activation, all these parameters were used to study VGSCs kinetics since the upstroke of APs is dominated by sodium current. Hence, it is reasonable to expect that the peak of the rising phase of the \ddot{V}_m trace is dominated by sodium current. Moreover, in a recent study, we showed with a computational model that the \ddot{V}_m peak width methods are more sensitive and specific to VGSC conductance and rate constant parameters than the phase slope method [27]. For instance, tripling the VGSC conductance caused a 65% increase in rapidity as quantified by the IFWd² method, but it caused only a 10% increase as quantified by the phase slope method [27]. Thus, the \ddot{V}_m peak width methods are better tools to study the potential role of VGSCs in AP onset dynamics. These improved tools showed significant differences in AP rapidity between all 4 neuron types, albeit using recordings that may have had some different experimental procedures. Future analysis of RS and FS neuron recordings acquired from the cortex and hippocampus under comparable conditions using the \ddot{V}_m peak width methods could further elucidate VGSC differences in these neurons.

4.5 Conclusions

Two novel methods, IFWd² and IHWd², are more reliable and systematic tools to quantify the rapidity of AP onset than other existing methods. These \ddot{V}_m peak width methods provide a smaller relative variation among APs from a single neuron type while still distinguishing between

different neuron types more robustly than the phase slope and error ratio methods. Using the new second derivative methods, AP onset rapidity has been demonstrated as useful for neuron classification. Thus, the IFWd² and IHWd² tools should prove valuable for studying and analyzing the kinetics of VGSCs and their role in AP dynamics, such as examining different hypotheses proposed to cause the rapid AP initiation in central mammalian neurons.

5 THE IMPACT OF DYNAMIC REVERSAL POTENTIAL AND COOPERATIVITY ON THE EVOLUTION OF RAPIDITY AND OTHER ACTION POTENTIAL ATTRIBUTES DURING SPIKE TRAINS

Preface

This chapter closely corresponds to a manuscript co-authored by Aldohbeyb, Vigh, and Lear that is intended to be submitted to a peer-reviewed computational neuroscience journal. Ahmed A. Aldohbeyb's contributions were investigating neuron firing patterns in response to multiple current pulses, identifying common firing patterns across different neuron types, writing the MATLAB codes for different neuron models, identifying and describing prior related work, modifying the models to include dynamic and cooperative gating, calculating the AP attributes from experimental data and computational models, replicating the observed firing patterns in models including the effect of cooperative gating and ion concentration dynamics, analyzing the data, identifying and describing prior related work, discussing all aspects of the research, conceptualizing many figures and creating all of them, writing the manuscript, and editing text and figures in response to feedback from the other co-authors.

Abstract

Action potentials (AP) are the basic elements of information processing in the nervous system. Understanding the AP generation mechanisms is a critical step to understand how neuron encode information. However, individual neuron fires various AP shapes even in response to the same stimulus, and the mechanisms responsible for this variability remain unclear. Therefore, we analyzed four AP attributes during bursts from three neuron types using published electrophysiology recordings. In response to consecutive step currents, the AP attributes in evoked

spike trains show two distinctive patterns across different neurons. The first APs from each stimulus always have comparable properties regardless of the stimulus strength, while the attributes of the subsequent APs during each pulse monotonically change (i.e., tilt) during the burst and the magnitude of AP attribute change during each pulse increases with increasing stimulation strength. Various conductance-based models were explored to determine if they replicated the observed AP bursts. The observed patterns could not be replicated using the classical HH-type models. However, adding ion concentration dynamics to the model reproduced the AP attribute tilt, and the magnitude of change during a pulse correlated with change in dynamic reversal potential (DRP), but the first APs attributes remained unchanged. Then, the role of cooperative Na^+ gating on neuronal firing dynamics was investigated. Cooperative gating of Na^+ channels has been proposed as the mechanisms underlying the rapid AP initiation and threshold variation in cortical neurons. Inclusion of cooperative gating restored the first APs attributes, and enhanced the magnitude of modeled tilt of some AP attributes to better agree with observed data. We conclude that this work indicates changes in local ion concentrations could be responsible for the monotonic change in APs attributes during neuronal bursts, and cooperative gating can enhance the effect. Thus, the two mechanisms could contribute to the observed variability in neuronal response.

5.1 Introduction

Neurosciences uses neuron models to seek some understanding through the complexity of neural dynamics. The choice from large variety of neurons models “follows a simple trade-off rule of what to include to make the model realistic but simple enough to implement” [108]. For this reason, a simple single-compartment model such as the Hodgkin and Huxley (HH) model, or even the simpler integrate-and-fire model, has been used for decades. Although growing evidence in central mammalian neurons indicates a discrepancy between experimental data and the HH model

[2], [5], [6], [31], [32], most of the proposed models incorporate the basic functions and equations from the HH model [33], [34]. The HH model simplifies the effect of ion concentrations assuming constant electrical gradients and neglects ion concentration change, but successfully reproduces neuronal signals' general features.

While neglecting ion concentration changes during neuronal firing could be valid in invertebrate neurons, its validity in mammalian neurons is subject to debate. Fluctuation in K^+ and Na^+ concentrations was noted in healthy cortical neurons [22]–[25] but more abundantly observed during abnormal activities such as seizure [26], [67], [109]–[113]. Thus, most computational models with dynamical ion concentration have been used to study neuronal abnormal activities. Cressman *et al.* (2009), for example, showed changes in ion concentration led to seizure-like events using a conductance-based neuron model with Na^+ and K^+ ion concentration dynamics [26], [67]. Krishnan and Bazhenov showed, in combination with electrophysiological recording and modeling, changes in K^+ , Na^+ , and Na^+/K^+ pump during seizures [66], [114]. However, ion concentration dynamics should be applied as well to understanding normal conditions [22], [23]. Using computational models that include only Na^+ and Ca^{2+} dynamics, Zylbertal *et al.* showed that the dynamic of Na^+ concentration in models of three neuron types has a huge impact on neuron bursting activity [70]. Nonetheless, the vast majority dynamical ion concentration models constructed to study the neuron pathological states, not normal neuronal behavior.

AP initiation features are another source of discrepancy between simple neuron models and experimental data. Rapid AP initiation and threshold variability are a characteristics of somatic cortical neurons APs. Among many explanations, cooperativity between neighboring Na^+ channels was proposed to account for two AP initiation features [2], and was the subject of debate [3], [4], [7], [30], [59]. A major criticism of the cooperativity model has been the absence of supporting

biological evidence. However, several studies have bridge this gap [16]–[19]. For instance, a study showed using Na⁺ channel's crystal structure that the β3-subunits can bind to multiple sites of Nav1.5 α-subunits [16]. Clatot *et al.* (2017) found that Nav1.5 α-subunits physically interact, in which their results were consistent with Naundorf *et al.* . [17]. Also, coupled gating was linked to Na⁺ channel mutations [18], [19]. These cumulative studies in recent years have made it clear that mammalian Na⁺ channel kinetics deviate from the canonical HH model, emphasizing the need to reevaluate the role of channel kinetics and ion concentration dynamics in biophysical models. A detailed model that includes cooperative gating and ion concentration dynamics should provide more insight into neuronal response to repetitive stimulus.

Understanding the AP initiation mechanisms is essential in determining how neurons process information and the variability in AP shapes. Variability in neuronal response was observed even in individual neurons in response to the same stimulus [14]. The observed variability of neuronal response could arise from several factors such as the diversity in voltage-gated ion channel types and densities, diversity in synaptic inputs, or the neuron's intrinsic such as axial resistance or the size of the soma and dendritic tree properties [3], [13]–[15]. Although neuronal response is usually studied in terms of firing rate and spike timing [14], [115], [116], i.e., the temporal position of APs, looking at the attributes of each AP's waveform, i.e., details of its shape and size, and how those attributes vary during a spike train provides another perspective on neuronal coding. While a neuron's firing pattern might has more importance than the AP shape when studying neuron behavior, and there was little correlation between them, the two cannot be clearly separated [46]. In addition, AP attributes were found to have four times larger correlation with the stimulus history than the instantaneous spike rate [10].

Our study here similarly shows variability in response but based on systematic changes in ion concentrations resulting from prior APs rather than due to randomness, such as that associated with natural stimulus. Analysis of electrophysiology recordings in public databases for three neuron types demonstrate that AP attributes including AP rapidity and threshold display recurring monotonic patterns in response to multiple current pulses, and the magnitude of change in these patterns during each pulse increases with increasing current. Despite the stimulus-dependent evolution of AP attributes during a pulse, the AP attributes of the first spikes in each stimulus pulse are strikingly similar despite the stimulus strength. A variety of existing computational models were investigated, but all failed to replicate the observed AP attribute patterns during spike trains. Thus, a novel conductance-based model that includes ion concentration dynamics and cooperative Na⁺ channels was constructed to replicate the observed patterns. Changes in the dynamical reversal potential (DRP) due to changes in ion concentration was responsible for the evolution in AP attributes during stimulus pulses but also predicted monotonic changes in AP attributes in the first AP of each sequential pulse, contrary to the analysis of neural recordings. Notably, adding cooperative Na⁺ channels to the model equalized first-AP attributes while not only retaining but enhancing the magnitude of AP attribute evolution during each pulse. Both consequences of including cooperativity, first-AP attribute equalization and increased intra-pulse evolution magnitude, resulted in better agreement with analysis of public experimental recordings. With cooperativity, the modeled magnitude of intra-pulse variation in some AP attributes, such as rapidity, approximately agrees with experimental observations, while the model still underestimates the magnitude of systematic variation for other AP attributes, in particular threshold potential. The impact of selected model parameters such as cell volume ratio were also

investigated. Our study predicts that ion concentration dynamics and cooperative Na⁺ channels could have a role on neuronal encoding by adjusting AP features during repetitive firing.

5.2 Methods

AP parameters

The AP threshold voltage, amplitude, rapidity, width of each AP were analyzed. The AP threshold was measured as the membrane potential at which \dot{V}_m exceeds 25 mV/ms. The AP amplitude was measured from the threshold potential to the peak value, and the spike width was measured as the full width at half the AP amplitude. The AP rapidity was measured using two methods: the inverse of the full width at half the maximum value of the rising phase of \dot{V}_m (IFWD² method) [27], [28], and the phase slope method [2]. The phase slope was measured as the slope of the phase plot reached a specific criterion level. The criterion level was adjusted in some cases. The reason for choosing different criterion levels is that the phase slope could be significantly impacted if the criterion level is near the transition between the baseline and the vertical rise in the phase space plot [28].

Data source for AP recordings

Experimental intracellular recordings were obtained from two databases. The somatosensory cortex recordings were from the GigaScience database [78], whereas the hippocampal neurons recordings were from the CRCNS database [87]. The experimental procedures for the somatosensory cortical recordings and data are found in da Silva Lantyer *et al.*, 2018 [78]. The data were from current-clamp recordings of pyramidal regular-spiking (RS) neurons (n=27) and fast-spiking (FS) neurons (n=7). The experimental procedures for hippocampal neurons are found in Lee *et al.*, 2014 [87], [88]. These current-clamp recordings from

the 17 RS pyramidal neurons were made from adult mice hippocampal CA1 neurons. The same APs selection criteria was used as previously described [28], except the inter-spike interval (ISI) was set to be 10 ms for all neuron types.

Computational models

All simulations presented here were done using MATLAB 2021. The dynamical equations were solved using the fourth order Runge-Kutta method with 1 μ s time step, unless stated otherwise. The model describes a single-compartment conductance-based model for different cortical neuron types. The model includes Na⁺ and K⁺ voltage-gated channels and the membrane potential is described by the following equations [82]:

$$C_m \frac{dV}{dt} = -g_{leak}(V - E_{leak}) + I_{Na} + I_{Kd} + I_{app}$$

Where V is the membrane potential, $C_m = 1 \mu\text{F}/\text{cm}^2$ is the specific membrane capacitance, g_{leak} and E_{leak} are the membrane conductance and its reversal potential. I_{Na} is the Na⁺ channels current, I_{Kd} is the "delayed-rectifier" K⁺ current. The gating variables and their rate equations were used exactly as described Pospischil *et al* (2008) [82], except for the activation of Na⁺ channels, which is described below. I_{app} is the applied (stimulus) current, which consists of 1s step pulses separated by 5s inter sweep interval, unless stated otherwise.

5.2.1.1 Cooperative sodium current

The voltage-dependent Na⁺ channels current was modified from Hodgkin and Huxley (HH) type model described by Pospischil *et al.* (2008) [82] to include a fraction of cooperative Na⁺ channels. The cooperative Na⁺ channels were described similar to Hunag *et al.* (2012), where the activation of Na⁺ channels (m) was assumed to be instantaneous, and hence it was replaced by its steady-state value m_∞ [5]. The following equations determine the dynamic of Na⁺ channels:

$$I_{Na} = (1 - p)g_{Na}m_{\infty}^3(V)h(V - E_{Na}(t)) + pg_{Na}m_{\infty}^3(V_{Na})h(V - E_{Na}(t))$$

$$m_{\infty} = \frac{\alpha_m}{\alpha_m + \beta_m}$$

$$\frac{dh}{dt} = \alpha_h(1 - h) - \beta_h h$$

$$V_{Na} = V + KJm_{\infty}^3(V_{Na})h$$

Where p represents the fraction Na^+ channels exhibiting cooperative gating and KJ is the coupling strength voltage between cooperative channels. α and β are the transition rate constants, which were adopted exactly as described in [82]. $E_{Na}(t)$ represents the Na^+ dynamic reversal potential.

5.2.1.2 Dynamical reversal potential

The model includes variable concentrations of intracellular and extracellular Na^+ and K^+ , which are used to calculate the dynamic reversal potential (DRP) for each ion channel. The evolution of K^+ concentration is determined, as described by Cressman *et al* (2009I) [26], by the following equation:

$$[K^+]_i = 140mM + (18mM - [Na^+]_i)$$

$$\frac{d[K^+]_o}{dt} = \gamma I_{K^+} - 2I_{pump} - I_{glia} - I_{diff}$$

$$I_{pump} = \left(\frac{\rho}{1 + \exp((25 - [Na^+]_i)/3)} \right) \left(\frac{1}{1 + \exp(5.5 - [K^+]_o)} \right)$$

$$I_{glia} = \left(\frac{G_{glia}}{1 + \exp((18 - [K^+]_o)/25)} \right)$$

$$I_{diff} = \varepsilon([K^+]_o - k_{o\infty})$$

Here γ is a factor to convert current density to rate-of-change of concentration. I_{pump} represents the sodium-potassium pump. I_{glia} represents the capacity of glial cells to remove excess K^+ from the extracellular space, and I_{diff} represents the diffusion of K^+ away from the local extracellular micro-environment. The remaining factors and their values are described in Table 5.1. The equation for Na^+ concentration was also adopted from Cressman *et al* (2009I). The Na^+ concentrations are given by:

$$\frac{d[Na^+]_i}{dt} = \gamma I_{Na^+} - 3I_{pump}$$

$$[Na^+]_o = 144mM - \beta([Na^+]_i - 18mM)$$

Table 5.1: model parameters and values

Parameters	Value	Description
γ	0.33	Conversion factor from current density to rate-of-change of concentration ($mM.cm^2/\mu C$)
β	7	Ratio of intracellular to extracellular volume of the cell
ρ	1.25	Pump strength (mM/s)
G_{glia}	66.67	Strength of glial uptake (mM/s)
ϵ	1.2	Diffusion constant (s^{-1})
$k_{o\infty}$	4	Steady state extracellular potassium concentration (mM)
φ	0.35	Voltage dependence parameter
E_{Leak}	-70	Leak channels reversal potential (mV)
V_T	-63	Variable to adjust spike threshold (mV)
g_{Leak}	0.15	Leak channels maximum conductance (mS/cm^2)

g_{Na}	50	Sodium channels maximum conductance (mS/cm ²)
g_{Kd}	10	Potassium channels maximum conductance (mS/cm ²)
$L = W$	61.4	Length and width of the modeled membrane area(μm)

Finally, in some cases, we assumed that the available intracellular Na⁺ concentration might differ for the channels and Na/K pump. Thus, the concentration was adjusted to be:

$$\frac{d[Na^+]_i}{dt} = \gamma I_{Na^+} - I_{Na_{diff}}$$

$$\frac{d[Na^+]_{pump}}{dt} = I_{Na_{diff}} - 3I_{pump}$$

$$I_{Na_{diff}} = \varepsilon_{Na}([Na^+]_i - [Na^+]_{pump})$$

The intracellular Na⁺ concentration adjacent to the channels would increase while channel current flows to drive ion diffusion from the channel to the locations of Na/K pump proteins. Therefore, $I_{Na_{diff}}$ represents the diffusion current of sodium ions away from the channels to the nearest pump. The Na⁺ diffusion constant, ε_{Na} , was obtained following Fick's law ($\varepsilon_{Na} = 2D_{Na}/\Delta x$), where we used $D_{Na} = 0.3 \mu\text{m}^2/\text{ms}$ [70] and Δx is the typical spacing between Na⁺ channels and the pump. Here, the pump current is governed by the extracellular K⁺ concentration and Na⁺ concentration near the pump ($[Na^+]_{pump}$), instead of intracellular Na⁺ concentration near channels ($[Na^+]_i$). Note the Na⁺ concentration was assumed to be the same for the pump and channels in most sections of the results, unless stated otherwise.

5.3 Results

Neurons alter AP parameters during continuous firing

Neurons firing patterns continuously change their during stimulation. Neuronal response variability has been studied for identical or varying stimuli and was often described in terms of spike timing, mean firing rate, or AP shape [10], [14], [89], [115]. The results in this study show a similar response, but the variability is more systematic than random. The neuronal response is shown in terms of AP attributes in three cell types: RS cortical neurons, FS cortical neurons, and RS hippocampal pyramidal neurons. All the neurons analyzed show two distinct spike train features in response to current pulse stimulation. First, quantitative AP attributes monotonically change during spike trains evoked by each current pulse. Second, the first AP evoked by each current pulse has similar AP attributes independent of the stimulation strength. Figure 5.1 shows examples of RS and FS cortical neuron burst in response to multiple-step current. The quantitative AP attributes, except threshold, are normalized to their values for it's the first spike value evoked by the first current pulse. The threshold potential is shown as the threshold for each AP minus the threshold of the first AP due to the first current pulse (Δ_{thr}), so positive threshold indicates a more depolarized threshold and negative threshold change indicates a more hyperpolarized threshold compared to the first spike. For example, the first spike evoked by the fifth (red) current step for cortical FS neuron was only 4.5% more rapid than the first spike evoked by the first (minimum) current step. In contrast, the rapidity of the last spike in the fifth current step was reduced by 45% compared to the first spike of the first current pulse. Even though a high current step depolarizes the membrane potential, and a higher AP threshold potential is expected, the onset threshold of the first spikes in all current steps was similar. The largest change in the threshold of the first APs of each step is only 4 mV, while the average threshold for the fifth spike train was 15 mV higher than

the first spike train. These spike train pattern shown in Figure 5.1 was observed in all 51 neuron recordings analyzed here.

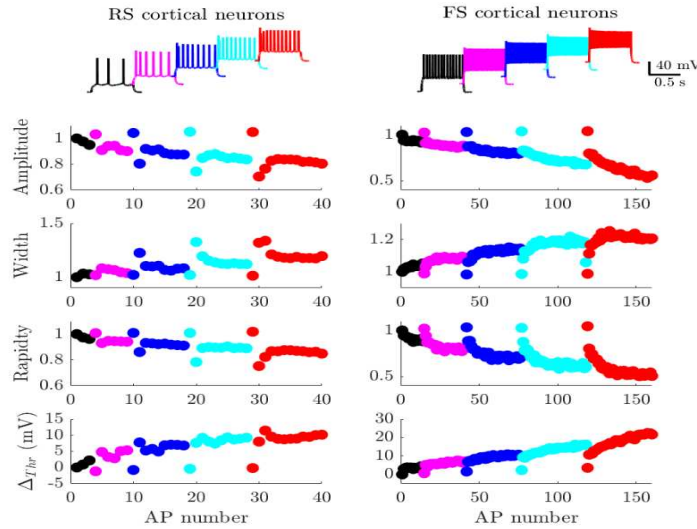


Figure 5.1: Changes in AP attributes from whole-cell intracellular recordings of a typical RS and a typical FS somatosensory cortical neuron. The color of the spike train reflects the strength of the stimulus where black traces show the spike train evoked by the minimum current step and red shows the spike trains evoked by the highest current step. Δ_{thr} is the potential difference between the onset threshold of each spike and the threshold of the first AP in black. Rapidity is calculated using the IFWd² method. The current pulses stimulation protocol included 5 steps of 0.5s long depolarization pulses (step size 40 pA and 6.5s inter-sweep interval between the pulses) For more information about the recordings, see da Silva Lantyer *et al* (2018) [78]

The magnitude of neuronal response varies between individual neurons. The first spikes' attributes are clustered around the same value as its first AP evoked by the first pulse across different cells despite the increasing stimulus strength, while the variability between individual neurons is more distinct when considering the average or final values of the AP bursts. For instance, comparing the rapidities of the first APs of the first and fifth spike train shows a slight increase but with an insignificant difference between them (FS cortical neurons, Mann Whitney $z = 0.87$, $t = 0.54$, p -value = 0.38, common language effect size, CLES = 0.41). On the other hand, comparing the average rapidity of the first and fifth spike trains shows a significant reduction (Mann Whitney $z = 2.07$, $t = 2.56$, p -value = 0.03, CLES = 0.82). Similar AP attribute patterns were observed across different neuron types. The average AP amplitude and rapidity decrease, and

the average AP threshold and width increase during the multiple step stimulation protocol. The average intra-pulse AP attribute variation also increases with each subsequent spike train. Table 5.2-5.4 summarizes the mean and standard deviation values for each of the three neuron types in response to 5 current steps. These features are robust and could not be replicated using the classical HH or cooperative models without other mechanisms. However, the model containing dynamical reversal potential (DRP) can replicate the trends in the spike patterns observed in electrophysiological recordings, which is discussed in the following sections.

Table 5.2: AP attributes of 7 FS cortical neurons in response to 5 current steps (mean \pm SD).

I_{app} Step	IFWd ² rapidity (ms ⁻¹)		Threshold (mV)		Amplitude (mV)		Width (ms)	
	1 st APs	Average	1 st APs	Average	1 st APs	Average	1 st APs	Average
1 st	3.10 \pm 0.3	2.97 \pm 0.3	-39.2 \pm 8.1	-35.2 \pm 7.0	63.0 \pm 4.9	57.5 \pm 4.2	0.66 \pm 0.1	0.66 \pm 0.1
2 nd	3.14 \pm 0.3	2.87 \pm 0.4	-40.7 \pm 8.1	-34.2 \pm 7.4	66.4 \pm 1.2	56.4 \pm 3.6	0.65 \pm 0.1	0.67 \pm 0.1
3 rd	3.17 \pm 0.3	2.77 \pm 0.4	-40.2 \pm 8.3	-32.6 \pm 8.0	66.7 \pm 1.1	54.1 \pm 3.5	0.65 \pm 0.1	0.69 \pm 0.1
4 th	3.17 \pm 0.3	2.67 \pm 0.5	-39.9 \pm 8.7	-30.5 \pm 8.9	67.1 \pm 1.3	51.3 \pm 4.1	0.65 \pm 0.1	0.70 \pm 0.1
5 th	3.19 \pm 0.2	2.56 \pm 0.5	-39.2 \pm 8.9	-28.3 \pm 10	67.3 \pm 1.2	48.2 \pm 5.3	0.65 \pm 0.1	0.72 \pm 0.1

Table 5.3: AP attributes of 27 RS cortical neurons in response to 5 current steps (mean \pm SD).

I_{app} Step	IFWd ² rapidity (ms ⁻¹)		Threshold (mV)		Amplitude (mV)		Width (ms)	
	1 st APs	Average	1 st APs	Average	1 st APs	Average	1 st APs	Average
1 st	2.84 \pm 0.3	2.57 \pm 0.3	-34.5 \pm 9.2	-28.9 \pm 8.8	79.6 \pm 7.8	69.3 \pm 9.2	1.43 \pm 0.2	1.54 \pm 0.3
2 nd	2.86 \pm 0.2	2.47 \pm 0.3	-34.1 \pm 9.90	-26.2 \pm 9.3	80.7 \pm 7.7	65.7 \pm 8.3	1.42 \pm 0.3	1.62 \pm 0.3
3 rd	2.89 \pm 0.2	2.37 \pm 0.3	-34.1 \pm 10.1	-23.8 \pm 9.5	81.6 \pm 8.1	61.4 \pm 9.1	1.42 \pm 0.3	1.68 \pm 0.3
4 th	2.90 \pm 0.2	2.32 \pm 0.4	-33.2 \pm 10.7	-22.1 \pm 10.9	81.9 \pm 8.3	59.5 \pm 10.7	1.42 \pm 0.3	1.72 \pm 0.3
5 th	2.90 \pm 0.2	2.26 \pm 0.3	-32.4 \pm 11.1	-20.1 \pm 11.5	81.7 \pm 8.6	56.2 \pm 11.4	1.42 \pm 0.3	1.75 \pm 0.3

Table 5.4: AP attributes of 17 RS hippocampal neurons in response to 5 current steps (mean \pm SD).

I_{app} Step	IFWd ² rapidity (ms ⁻¹)		Threshold (mV)		Amplitude (mV)		Width (ms)	
	1 st APs	Average	1 st APs	Average	1 st APs	Average	1 st APs	Average
1 st	5.53 \pm 0.6	5.20 \pm 0.5	-36.5 \pm 2.7	-35.6 \pm 2.7	78.5 \pm 7.4	76.6 \pm 6.8	1.04 \pm 0.08	1.07 \pm 0.08
2 nd	5.54 \pm 0.5	4.84 \pm 0.6	-35.5 \pm 2.8	-33.6 \pm 2.8	77.1 \pm 7.4	73.26 \pm 6.6	1.03 \pm 0.07	1.15 \pm 0.10
3 rd	5.57 \pm 0.4	4.64 \pm 0.7	-35.1 \pm 2.8	-32.1 \pm 3.0	75.8 \pm 7.6	71.06 \pm 6.5	1.02 \pm 0.08	1.26 \pm 0.15
4 th	5.45 \pm 0.5	4.51 \pm 0.7	-34.5 \pm 3.1	-30.8 \pm 3.4	74.9 \pm 7.6	69.26 \pm 6.5	1.00 \pm 0.08	1.38 \pm 0.20
5 th	5.51 \pm 0.6	4.38 \pm 0.8	-34.0 \pm 3.4	-29.4 \pm 3.7	74.2 \pm 7.7	67.56 \pm 6.6	1.00 \pm 0.08	1.50 \pm 0.25

Ion concentration changes dictate monotonic variation in AP attribute

The generation of neuronal spikes is due to the movement of ions through the voltage-gated channels embedded in the membrane wall. Prior works assumed that changes in ion concentrations at each end of the channel can be neglected since the AP was viewed as too sudden and brief to cause any significant change in ion concentration. The change in ion concentration was primarily considered in long-time scales (in seconds or minutes) when the neuron exhibits epileptic events, but not usually during the regular firing regime [25], [26], [70]. However, this study supports the view that changes in ion concentration influence normal neuronal dynamics both in the short and long timescale.

Variety of HH models for different classes of neurons produces different AP shapes and firing patterns but fails to replicate the variation in AP attributes during bursts. Simple model of FS cortical neurons (incorporating only I_{Na^+} , and I_{K^+}) were sufficient to generate the intrinsic firing characteristics of experimental recording [82]. In some cases, it was necessary to add slow K^+ (I_M) channels for initial frequency adaption observed in several neuron types [82]. However, all these models fail to replicate the monotonic variation in AP attributes observed in intracellular

recordings (Figure 5.2). Although the threshold onset potential increases within the first few APs due to I_M , the threshold stay constant for the remaining APs within a burst (Figure 5.2). Various HH types with different rate functions were investigated as well, but none of these models produce the attributes variation [5], [71], [82], [115]. However, AP attribute variation emerges once DRP is included in any of the HH models. Thus, the remainder of this research employed a simple model of a FS cortical neuron with only I_{Na^+} and I_{K^+} as the base for any modifications.

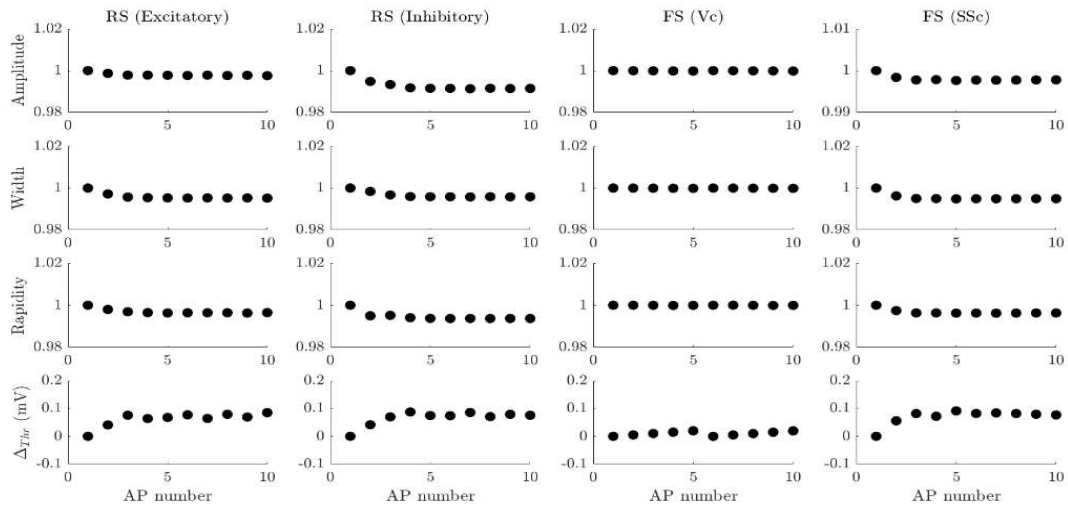


Figure 5.2: AP attribute evolution in spike trains resulting from different HH-type models. All the models are used as described in Pospischil et al. (2008). The models include three ionic currents (I_{Na^+} , I_{K^+} , and I_M), except the FS model for a visual cortical neuron (Vc) that includes only I_{Na^+} and I_{K^+} . The variation of normalized AP amplitude, width, and rapidity is less than 1% for all models.

Dynamic ion concentration changes are responsible for the monotonic variation in AP attributes during neuronal stimulation. Ionic currents partially deplete or accumulate ion concentrations in the vicinity of ion channels when those concentrations are restored via diffusion rather than directly fixed to bulk reservoir concentrations. The shift in ions concentrations adjacent to channels during current pulses alters the channels' reversal potential, which in turn affects neuronal excitability. As shown in Figure 4.3, DRP causes AP attributes to vary in a manner resembling experimental data during a step-current protocol. AP broadening and amplitude reduction was previously been widely observed in experimental recordings and was attributed to

Na^+ and K^+ channels [10], [117]–[120], where each channels influence the spike train waveform differently. The low K^+ channels inactivation recovery was shown to be the primary factor in AP broadening [119]. On the other hand, reduction in AP amplitude was ascribed to blocking voltage-dependent calcium current in Purkinje cell [121], and by Na^+ channels activation in cortical pyramidal neurons [122]. Classical models are inconsistent with these experimental observations, unless DRP is considered for both channels. In multicompartment models that account for Na^+ concentration dynamics only, Zylbertal *et al.* reproduced the amplitude adaptation in a cortical pyramidal cell model but not with a Purkinje cell model, which agrees with experimental observations that Na^+ channels cause the amplitude reduction in cortical neurons but not in the Purkinje cell [70]. Furthermore, we used a simple cortical neuron model that includes Na^+ and K^+ concentration dynamics to reproduce similar AP broadening and amplitude reduction. Although, the magnitude of modeled variation is smaller than the observed experimental change, ion concentration dynamics could be another factor effecting AP width and amplitude patterns.

The impact of DRP is more significant on AP initiation attributes (threshold voltage and rapidity). Previous studies had linked the variation in AP initiation features to the rate of membrane potential changes prior to the AP, stimulus history, Na^+ channels density and activation or inactivation processes, or AP backpropagation [2], [5], [10], [12], [123], [124]. The maximum AP rising slope was used as indication of sodium channel kinetics, and hence as a parameter to analyze AP initiation variation. Henze and Buzsaki found high variation in threshold potential and the rising slope of individual hippocampal neurons. They argued that the mechanism behind high variation in AP initiation attributes must be activated by preceding individual APs and have long recovery time, which is a characteristic of Na^+ channels kinetics [12]. These criteria also apply to the dynamics of ion concentration, especially Na^+ , that are change by individual APs and have

slow recovery (Figure 5.3). The change in accumulated intracellular Na^+ is small but its removal is slow [66], while the percentage change in K^+ is large but rebalances faster after excitation. For example, a rise in E_{K^+} by 16 mV at the end of the current pulse decays back to near the steady-state value within 3s since ($\sim 1\text{s}$ time constant). At the same time, E_{Na^+} drops by a much smaller value ($\sim 1.7\text{ mV}$), but slowly increases and does not reach its steady-state value after 5s ($\sim 11\text{s}$ time constant). Thus, the systematic variation in AP rapidity, and to lower extend part of the threshold variation, is due to E_{Na^+} and E_{K^+} change during the pulse, and the slow recovery of E_{Na^+} lead to the first AP attributes reduction of the subsequent burst. The slight reduction in attributes of the first APs of sequentially increasing stimulus pulses diverges from experimental data where AP initiation attributes slightly increase (Table 5.2-5.4). However, DRP model can mimic the intra-pulse variation of AP attribute found in experimental data.

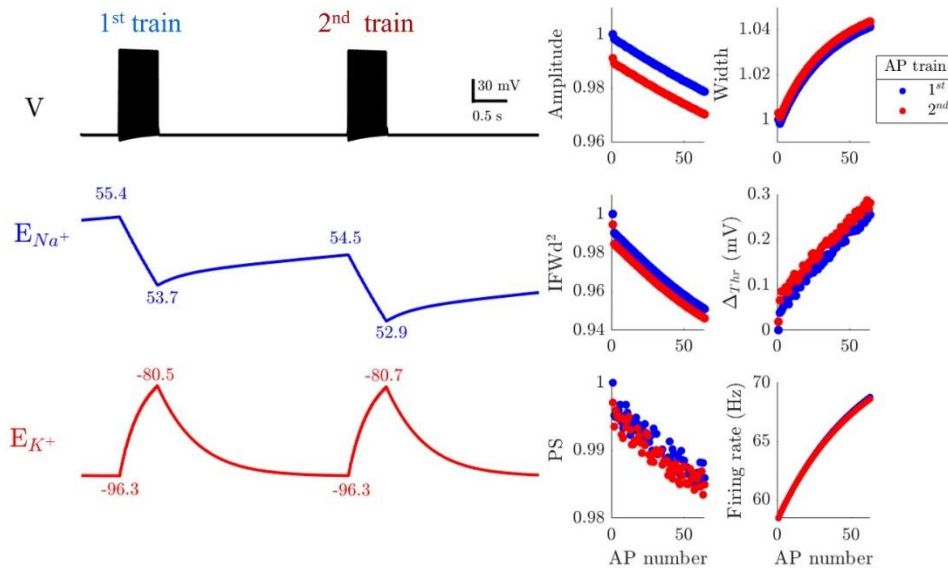


Figure 5.3: Membrane potential (V) and reversal potentials (E_{Na^+} and E_{K^+}) change during two current pulses ($I_{\text{app}} = 3.1 \mu\text{A}/\text{cm}^2$). The right column shows five attributes of each AP as well as the firing rate during the first (blue) and second (red) current pulse. Note that the change in E_{Na^+} during the stimulus pulse does not recover to within 1% of its resting value during the 5s between pulses, unlike the change in E_{K^+} .

Cooperativity and DPR replicates the spike patterns observed in intracellular recordings

Clusters of voltage-gated ion channels exist in various parts of neurons, creating concentrations of ionic currents and thus larger changes in ion concentrations near these clusters.. The corresponding changes in reversal potential during AP bursts impact neuron firing dynamics. Yet larger concentration changes and thus more impact on AP dynamics results if many of the clustered channels open in unison. Cooperative Na^+ channels, where the opening of one channel enhances the probability of neighboring channels opening, were suggested as one of the mechanisms responsible for the rapid AP initiation observed in cortical neurons [2], [5]. The interdependence of ion concentration dynamics on more rapid changes in membrane voltage associated with cooperative channel gating and the evolution of cooperative gating in the presence of altered ion concentrations raise an interesting question about how the combination of cooperativity and ion concentration changes modify neuronal firing. The impact of concentration change depends primarily on the instantaneous magnitude of ionic current (as described in the methods), which is enhanced by cooperative gating. Here, the combined effect of cooperativity and DPR is analyzed to investigate how the two mechanisms alter AP attributes and firing patterns compared to classical HH and cooperative models and how these changes fit experimental data.

Cooperative Na^+ gating enhances the variation of AP attributes during spike trains. DPR without cooperative gating causes the monotonic variation in AP attributes, but the magnitude of modeled variation is smaller than the experimental data, as shown above. Combining cooperativity and DPR increases the magnitude of modeled variation in all AP attributes except AP width. The insensitivity of AP width to Na^+ channel cooperativity is expected since cooperativity increase I_{Na^+} and the AP width is mainly determined by I_{K^+} [46], [104]. Although the magnitude of modeled threshold change is still small compared to experimental data, the magnitude of changes

in AP initiation attributes almost doubled in the presence of strong cooperative Na⁺ gating (Figure 5.4). Cooperativity boosted DPR change so that APs fire at a less depolarized (higher) threshold and reduced rapidity in response to strong stimulus. For example, with cooperativity the last AP was triggered at a 0.85 mV higher threshold and with 21% lower rapidity than the first AP, compared to 0.49 mV higher threshold and 12 % rapidity reduction without cooperativity. the impact of cooperative Na⁺ channels on the first spike attributes diverges from the classical HH model. Cooperative gating kept the first APs shape comparable despite the strength of the stimulus. Figure 4.5 illustrates the difference between the models' impact on AP features, compared to intracellular recording. First APs are initiated at a more hyperpolarized membrane potential in response to strong stimulus in the HH model. The relationship between stimulus strength and threshold is reversed in the presence of cooperative Na⁺ channels where first spikes are triggered at the same threshold voltage (Figure 5.4). Likewise, the first APs rapidity slightly increase with each current step with cooperative gating in manner resemble experimental data. The first AP of the fifth spike train has 1.5% higher rapidity than the first AP from of first spike train (red Figure 4.5), which is similar to the FS recordings (1.6% increase in Figure 5.4 blue). The increase in the modeled first AP rapidities is almost the same with or without DRP. However, the systematic attribute variation disappears without DRP. Therefore, the results show that both observed spike train features are only replicated by combining DRP and cooperative Na⁺ gating, where the magnitude of modeled variation agrees with experimental observations for some AP attributes.

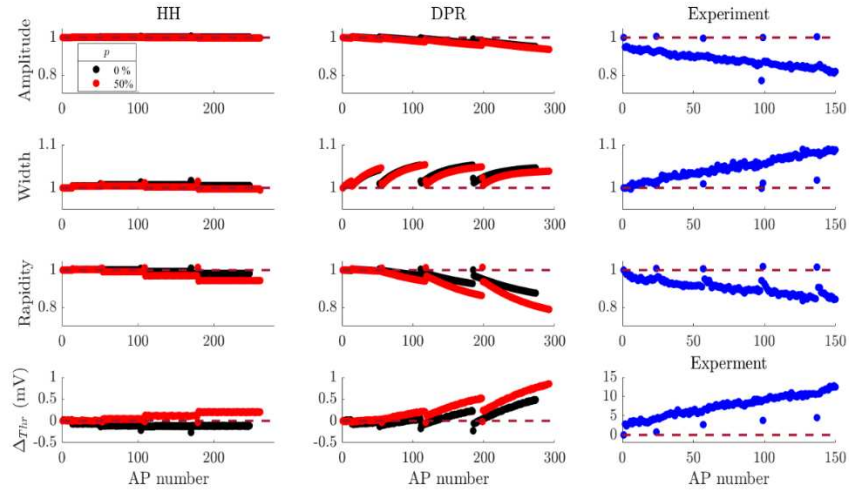


Figure 5.4: Comparison between AP attributes in different modeling conditions and experimental recordings. Left: the model was run with fixed dynamical reversal, black circles represent the values obtained from the original HH model, and red circles represent the values obtained from the cooperative channels model ($p = 50\%$ and $KJ = 400$ mV). Middle: the model with dynamical reversal potential with independent Na^+ channels (black circles), and with 50% cooperative Na^+ channels (red circles, $KJ = 400$ mV). The models were evoked by 5 1s-current steps (1.6, 2.4, 3.2, 4, and $4.8 \mu\text{A}/\text{cm}^2$) with 5s inter sweep interval. Right: AP rapidity and threshold difference from a somatosensory cortical neuron in response to five step current (0.5s steps of 80, 120, 160, 200, and 240 pA with 6.5s intra sweep interval) [78].

Cell volume and pump strength effect on AP attributes

The magnitude of AP attributes variation differs significantly between individual neurons. For example, the reduction in average rapidity ranges from 10% to 43% in the recordings from FS cortical neurons. The spread in the magnitude of monotonic variation was also observed in hippocampal and cortical RS neurons, indicating that other factors might contribute to the observed attribute variation. Neurons volume changes during abnormal and normal activities, and even neuron dilation during individual AP has been estimated [125], [126], where the neuron size stability is regulated through ions pump [127]. Thus, the ratio of intracellular to the extracellular volume of the cell, Na^+/K^+ pump strength, and Na^+ concentration near the pump were adjusted to explore their impact on spike train patterns.

Altering cell volume ratio significantly impact the magnitude of AP attributes variation (Figure 5.5). The rate of concentration change is directly impacted by the intracellular volume to

the extracellular volume ratio (see methods). A ratio of 7 was reported to reflect the normal condition value ($\beta=7$) [26]. Increasing the volume ratio did not influence the first AP of each pulse but did lead to higher variation of AP attributes during pulses, as shown in Figure 4.6. The change in the magnitude of variation is expected since the volume ratio is directly proportional to ion concentration dynamics (see methods). However, although all the results presented here are from normal firing behavior, unrealistic change in cell volume (such as increasing the volume ratio by 50%) is needed to observe any substantial difference in the neuron dynamics. A 60% swelling was observed in pyramidal cortical neurons during anoxic depolarization [128], and even a 10% change in the cell diameter can lead to seizure-like events [125]. Furthermore, pyramidal neurons were shown to maintain their volume during normal condition [129]. Nonetheless, from a modeling perspective, neuron swelling can influence normal neuronal firing behavior and its effect increase in the presence of cooperative channels.

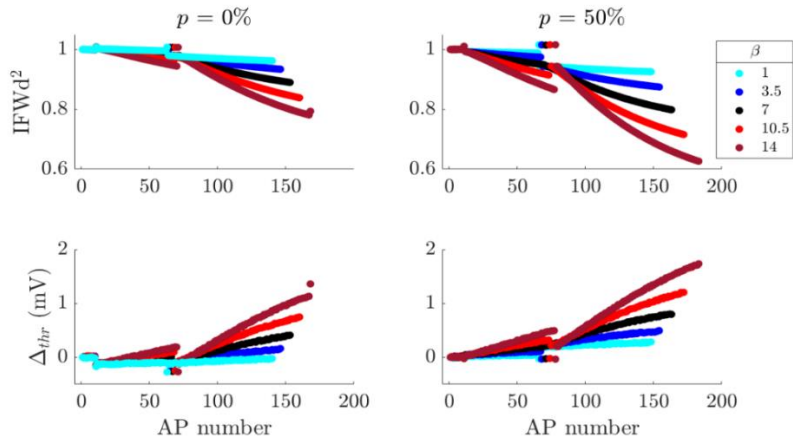


Figure 5.5: Impact of the intracellular to extracellular volume ratio on AP threshold and rapidity. The AP rapidity is normalized to the rapidity of the first spike and $\Delta_{thr} = Threshold - Threshold_{1st}$. Left: the values with no cooperative Na⁺ channels. Right: the values with 50% cooperative Na⁺ channels (KJ = 400 mV). The results were obtained with 3 steps current and intra sweep interval of 5 s.

The Na/K pump strength was modeled with two extreme values to explore the Na/K pump impact on AP onset dynamics. The average pump strength was reported to be around 1.1 mM/s [67]. An order of magnitude increases in Na/K pump speed made minimal changes to predicted

AP initiation attributes while an order of magnitude decrease led to either much smaller variation of attributes, and thus widened disagreement with experimental observations or in the absence of cooperativity pathological behavior of runaway ion concentration changes (Figure 5.7). Furthermore, changes to the pump activity can lead to abnormal neuronal activities such as seizures [130], and can desynchronizes neuronal firing and transmitter release [131].

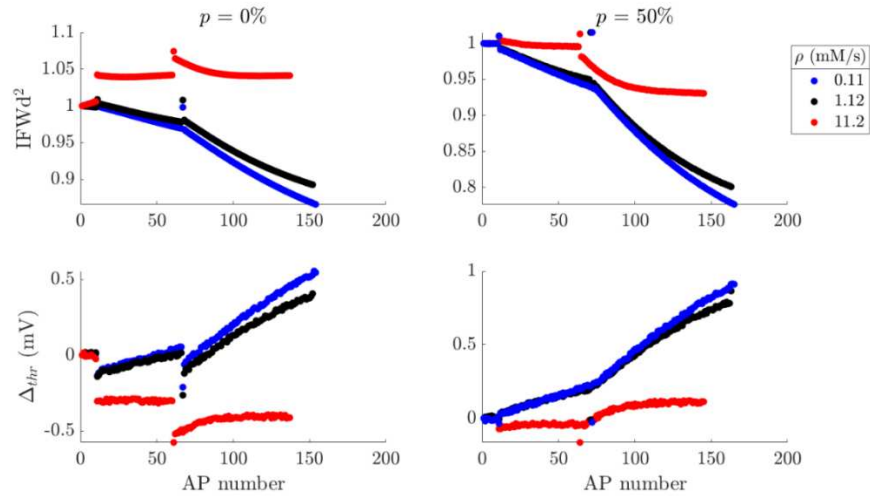


Figure 5.6: Impact of the Na/K pump strength on AP threshold and rapidity. The AP rapidity is normalized to the rapidity of the first spike and threshold difference. Left: the values with no cooperative Na⁺ channels. Right: the values with 50% cooperative Na⁺ channels (KJ = 400 mV). The results were obtained with 3 steps in current and inter-pulse intervals of 5 s. Note that the scale is not the same between independent and cooperative gating to show the difference in all three cases.

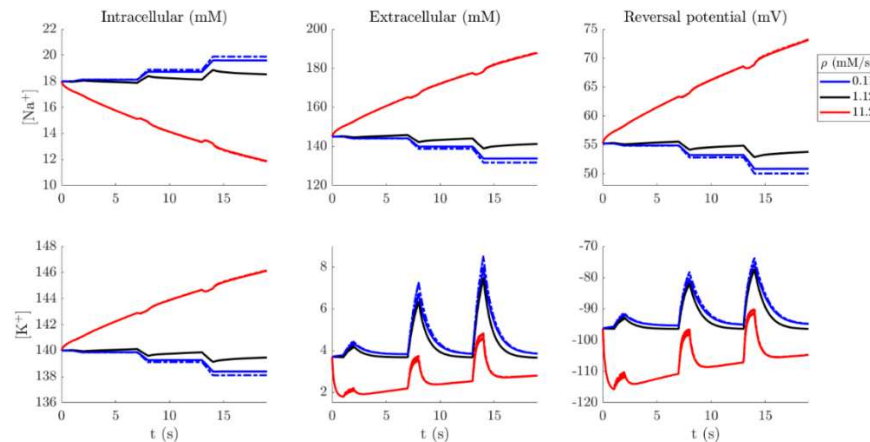


Figure 5.7: Impact of the Na/K pump strength on ion concentrations and reversal potential. The dashed-dotted line represents the concentrations and reversal potential in the presence of 50% strongly cooperative Na⁺ channels (KJ = 400mV). Note that the changes with cooperative channels and fast pump strength (dashed-dotted line) are more slightly more significant than the case with no cooperativity.

Finally, the impact of Na^+ diffusion between channels and the pump is investigated to see if it could account for the underestimation of changes in threshold potential and AP amplitude. The pump current is determined by $[\text{K}^+]_o$ and $[\text{Na}^+]_i$, assuming that any change in $[\text{Na}^+]_i$ is immediately available to Na/K pumps. Such an assumption implies that the spacing between the Na^+ channels cluster and the nearest pumps is either very small or the diffusion of ions is fast so that $[\text{Na}^+]_i$ is assumed to be the same at the channels and pumps. We hypothesized that $[\text{Na}^+]_i$ is near the channels must be higher than near the pump to drive diffusion between them. So, the model was adjusted to have $[\text{Na}^+]_i$ for the Na^+ channels and $[\text{Na}^+]_p$ for Na/K pump (see methods). The distance between the channels and the pump (Δx) and Na^+ diffusion coefficient (D_{Na}) were varied. The distance was varied from 0.25 μm , which the approximate diameter of observed Na^+ channel somatic cluster [132], to 25 μm . The diffusion constant, D_{Na} , was varied from the reported value 0.3 to 0.03 $\mu\text{m}^2/\text{ms}$ [70]. Even across this broad range of parameters, the results did not show any significant differences with or without strong cooperative gating (Figure C1-2). The difference in Na^+ concentration between the pump and channels site is too small to cause any noticeable effect on AP attributes. Therefore, even if there might be a difference in concentration between the pump and the channels, our simulations did not reveal any change in AP attributes.

5.4 Discussions

Here we described a single compartment conductance-based model that takes into account cooperative channel gating and the dynamics of ion concentration in normal neuronal conditions. Our analysis shows that the combined model reproduces the spike train pattern observed in central mammalian neurons, where we examined the impact of several factors on neuronal dynamics. The results show that the dynamic change of reversal potential due to changes in the local ion

concentration alters the AP attributes during neuronal firing, and the level of AP attribute change is enhanced in the presence of a fraction of cooperative Na⁺ channels.

Factors influencing neuronal variability

Understanding AP initiation is an integral part of determining how neurons encode information. The variability in neuronal response has interested scientists for decades, where the variability was observed between individual neurons of the same cell type [133], and for the same neuron in response to the same DC stimulus [14]. The observed variability of neuronal response could arise from several factors such as the diversity in voltage-gated ion channel types and densities, diversity of synaptic inputs, or the neuron intrinsic properties [13], [14]. Here, we observed variability in neuronal response, but the variability followed a specific pattern across different cell types. Applying multiple consecutive step currents, the evoked spike trains have similar first AP attributes regardless of the amplitude of the stimulus. Then, the AP attributes continuously change, and the parameters change magnitude increases with the amplitude of the stimulus. Even though the extent of systematic variation in AP attributes differed between individual neurons, the two spike train features were observed in all the neurons analyzed here. For example, the first spikes rapidity of 27 RS cortical neurons were comparable ($2.90 \pm 0.2 \text{ ms}^{-1}$) and higher by 17% than average AP rapidity ($2.26 \pm 0.3 \text{ ms}^{-1}$) in response to strong stimulus (Table 5.3). Mainen and Sejnowski showed that the timing of first spikes was tightly locked to the stimulus onset while being highly variable for last spikes [14]. Our result shows similar observation regarding the first AP spikes, but we observed similar pattern for last spike parameters.

The shape of action potentials differs significantly between neuron types. FS neurons exhibit narrower AP width and higher frequency than RS neurons [11], [85], [94]. Previous body of work associated the activity-dependent decrease in AP amplitude and broadening AP width to

Na⁺ and K⁺ channels [10], [117]–[119]. Geiger and Jonas showed the broadening of AP width in somatic granule cell AP and presynaptic hippocampal mossy fiber boutons APs [119], similar to the observed AP width pattern shown above (Figure 4.1). They found that broadening of AP width is mediated by fast-inactivating K⁺ current [119]. While the model could not produce the observed percentage of AP broadening, the results indicates that changes in K⁺ concentration could be among the factor contributing to AP broadening during firing.

The variation in AP initiation parameters was observed in hippocampal and cortical neurons. Threshold potential variation was linked to previous neuronal activities and Na⁺ channel gating. The threshold variation observed in pyramidal hippocampal neurons was attributed to the effect of previous APs, within 1s, on subsequent APs and the inactivation Na⁺ channels [12]. Higher threshold was found to coincide with lower spike rise (the slope of the AP from resting potential to the AP peak) as well, which is an indication of the degree Na⁺ channel inactivation [10]. Our analysis of publicly available experimental intercellular recordings agrees with these observations that higher threshold coincides with lower AP rapidity. A simple one-compartment model that includes DRP replicates the relationship between threshold and rapidity, and shows a good correspondence with experimental observations for AP rapidity, but not threshold. The magnitude of simulated rapidity variation was within the lower range of the observed change in experimental recordings, indicating that ion concentration changes could be responsible for the variation in AP initiation. Thus, ion concentration dynamics can have a major role in neuronal excitability during normal neuronal dynamics.

Ion concentration impact on spike train is enhanced with cooperative gating

The movement of ions mediates neuronal signaling through the voltage-gated channels, but usually ignored in neuronal models. However, fluctuation in [Na⁺] and [K⁺] was observed in

normal cortical neuron behavior[22]–[25]. In addition, increasing $[\text{Na}^+]_i$ was shown to facilitate seizure termination [66], and their slow dynamics can impact normal neuronal firing and synaptic activities [70]. Here, we showed that the continuous change in AP attributes due to concentration fluctuations alter normal spike train patterns, especially AP rapidity. The slow and steady increase in E_{Na^+} between current steps causes the change in first APs' rapidity. Combining cooperativity and dynamical reversal potential offset the slight decrease in the first spikes rapidity and enhance the magnitude of modeled variation. Cooperative Na^+ channels was proposed for the sharp AP onset variability and rapidity in cortical neurons [2], [5]. Thus, cooperative gating can set the level of AP initiation attributes, and their impact on ion concentration dynamics increase the magnitude of tilt during bursts. The two bursts' features could not be replicated in a variety of HH-type models without including DRP and cooperative gating.

5.5 Conclusions

Analysis of publicly available experimental intercellular recordings for three different neuron types show that AP attributes monotonically change during bursts while the first APs of each burst have comparable APs attributes. A single compartment model that includes DRP replicated the observed trends in AP attributes, and adding cooperative Na^+ gating enhanced those trends. The magnitude of modeled variation agrees with experimental observations for some AP attributes (rapidity, width) but not threshold and amplitude. Further investigations are needed to resolve this disagreement.

6 CONCLUSIONS

The overall objective of this Ph.D. dissertation is to develop analysis tools and construct computational models to study the AP initiation mechanism in central mammalian neurons. To achieve these goals, the proposed tool and model were verified against electrophysiological recordings from different neuron types. The rapidity quantification methods were judged based on their sensitivity and specificity to sodium channels using a classical HH model, the degree of variation among the same neuron types, and the degree of classification ability among different cell types using electrophysiological recordings. Then, a conductance-based model was developed to replicate AP train pattern in response to multiple current steps. The following sections summarize the achieved milestones and future works based on the findings.

6.1 Two novel methods for AP rapidity quantification methods

Two novel methods were developed for AP rapidity quantification. Previous quantification methods are affected by on the researcher's judgment on defining where the AP rapidity is measured. Thus, many studies exploring the same phenomena reported different values, complicating the comparison between their findings. The subjectivity in quantifying AP rapidity in prior methods highlighted the need for a more systematic and consistent method. Therefore, we proposed two novel methods to quantify AP rapidity that are well-defined and provide higher sensitivity and specificity to Na⁺ channels kinetics than prior methods. The proposed methods were based on the full-width and half-width at half the rising phase peak of the membrane potential second-time derivative, where the rapidity is defined as the inverse of the full-width at the half maximum of the \ddot{V}_m peak (IFWd²), and the inverse of half-width at the half maximum of the \ddot{V}_m

peak (IHWd²). The sensitivity and specificity to Na⁺ channels kinetics were verified using a conductance-based model.

The IFWd² and IHWd² methods showed higher sensitivity to Na⁺ channels kinetics than the standard AP rapidity quantification method, the phase slope method. The two \ddot{V}_m peak methods showed significantly higher sensitivity to all Na⁺ channels parameters and maximum conductance than the phase slope method. On the other hand, the phase slope method showed higher sensitivity to K⁺ channels parameters and maximum conductance than the proposed methods. For example, IFWd² rapidity doubled by increasing Na⁺ conductance 5-folds, but only 2% with K⁺ conductance. In contrast, the phase slope increased by 14% with five times the Na⁺ conductance and 5% with K⁺ conductance. Thus, we showed that the two \ddot{V}_m peak methods are better approaches to quantitatively study Na⁺ channels kinetics and the factors that contribute to AP onset dynamics in experimental data.

6.2 AP rapidity as a tool to classify neuron types

Differences in the AP shapes between neuron types, including quantitative features such as the AP width and amplitude, are well-known in the literature. However, AP onset rapidity had not been reported as one of the AP features used in classifying neuron types. Therefore, the \ddot{V}_m peak width methods alongside the two prior methods were used to quantify the rapidity of four central mammalian neuron types and analyze their ability to use rapidity as a classification parameter. The results showed that IFWd² and IHWd² methods provide a smaller relative variation among APs from a single neuron type while still distinguishing between different neuron types. Rapidity obtained using the phase slope and error ratio methods were significantly impacted by the selected data, criterion level, or the data interpolation function, which hampers their ability to

categorize neuron types when used with different researchers' parameters. On the other hand, the \ddot{V}_m peak width methods do not depend on subjective data selection, and they are minimally impacted by the choice of interpolation functions. Such benefits were reflected in the methods' ability to classify neuron types.

Analysis of rapidity shows a significant difference between the four neuron types (pyramidal hippocampal and cortical neurons, hippocampal PVBCs, and FS cortical neurons). The \ddot{V}_m peak width methods provide better separation between different cell types compared to the phase slope and the error ratio methods based on parametric and non-parametric statistical tests. In fact, the IFWd² method provides the highest classification ability of all the methods and hence provides a sensitive tool to investigate the mechanisms impacting AP dynamics. Moreover, the other AP feature with a good classification ability was the AP width, which is known to be one of the best classification parameters. Interestingly, the utility of both AP onset rapidity, which could be associated with Na⁺ channels, and AP width, which is mainly associated with K⁺ channels, to differentiate neuron types is intriguing since the two underlying mechanisms of Na⁺ and K⁺ channel types need not be correlated.

6.3 Mechanisms underlying AP variation in intracellular recordings

Variation in neuronal response was observed among the same neuron type from the same brain regions and even in individual neurons in response to the same stimulus [14]. The source of such variation can arise from several factors such as channel types and densities, dendritic tree size, AP initiation sites, or the intrinsic neuron properties [13]–[15]. Although neuronal response variability was previously shown in individual neurons receiving the same DC current, we showed that some variability is more systematic than random. An evoked spike train exhibits two

distinctive features in response to multiple-step currents. The first APs in a spike train usually have comparable attributes despite the stimulus strength, while the following APs during each stimulus pulse exhibit a continuous change (variation) that increases with the stimulus strength. The two distinctive spike train features were observed in 52 neurons of three different types, indicating a common mechanism that determines these features despite their biological differences.

We developed a conductance-based model that replicates the two distinctive spike train features observed in mammalian neurons. The observed trends could not be replicated using various standard computational models, indicating that the mechanism responsible for the attributes variation deviates from the classical models. However, the attributes variation was reproduced once dynamical reversal potential was incorporated into the models. The first spikes attributes can be better represented using cooperative Na^+ gating, which also boosted the variation magnitude for some attributes to match the experimental data, but failed to reproduce the magnitude of threshold variation. Thus, different mechanisms might be responsible for the high threshold variation in cortical neurons such as the conductance stimulus history or changes in the availability of active sodium channels (Na^+ inactivation mechanism). Finally, several model parameters were adjusted to investigate their impact on spike train patterns. Increasing cell volume ratio increases dynamic ion concentration changes and thus AP parameter variation, but realistic cell volume ratios still did not significantly affect AP bursts pattern. We conclude that changes in ion concentration dynamics are responsible for some of the AP parameters' variation during regular neuronal firing, and cooperative gating can enhance their effect. Therefore, the two mechanisms could contribute to some of the observed variability in neuronal response.

6.4 Future works

AP rapidity measured at the single-channel level

AP rapidity is a relatively new term in neuroscience. The importance of rapidity can probably trace back to the Naundorf *et al.* paper challenging the general view regarding Na⁺ activation mechanisms [2], [46]. Thus, it would be of interest to study changes in AP rapidity from single-channel recording and how different mutations could affect AP generation. A complete analysis of the effect of channels mutations on AP rapidity could be valuable, especially with recent studies indicating that Na channels physically interact and specific mutations impaired the coupled gating of Na⁺ channels [17], [18]. To my knowledge, such a recordings are not available in public databases., which pose an obstacle for such a study. However, in collaboration with the Tamkun lab, recordings from three SCN8A encephalopathy-causing mutations in one of the Na⁺ channel subtypes, Nav1.6, were analyzed. The initial results indicate a reduction in the mean IFWd² rapidity with some of these mutations, while other mutations did not alter the mean rapidity. Interestingly, the V216D mutation, the mutation associated with the most severe phenotype and the one causing the most significant electrophysiological changes [134], was the mutation that produced similar mean rapidity to the wild-type. On the other hand, the G214D and N215D mutations, which produced similar current density to the wild type, according to Solé *et al.* (2020), have a slower rapidity [134]. However, it should be noted that the rapidity results were not sufficient to make any conclusions since the number of recordings for each mutation is small, and the recording noise needs to be carefully filtered before any analysis. Further filtering and analysis for more recordings will provide a better understanding of the role of Nav1.6 mutations on AP rapidity. Analyzing the impact of these three mutations on AP rapidity could provide an insight into the mechanism of disease-causing mutations.

In addition to Nav 1.6 mutations, analysis of the abrupt spikes in retinal ipRGCs is a topic of interest. In collaboration with the Vigh lab, I analyzed AP trains elicited by intrinsically photosensitive retinal ganglion cells (ipRGCs) in response to dim and bright light stimuli. Initial results indicate that APs evoked by dim light were more rapid than APs evoked by bright light, which agrees with the idea of activity-dependent plasticity observed in retinal cells [135]. However, similar to Nav 1.6 data, more recordings and data preparation are needed before analyzing the AP rapidity due to noise in the existing recordings.

Improvement in Na^+ concentration modeling

To better understand the role of Na^+ concentration on neuronal firing, missing mechanisms might be necessary to include in computational models. Na^+ concentration dynamics are usually determined by the interactions of Na^+ current and Na^+/K^+ pump in models. However, different mechanisms such as astroglia uptake and Ca^{2+}/Na^+ exchanger could influence Na^+ concentration. Astrocytes were found to affect Na^+ concentration fluctuations and vice versa [136]. An increase in the glia sodium influx was observed during action potential generation, indicating the important role of glia cells in regulating Na^+ concentration [137]. However, in computational models, the glia-neuron interaction is only considered to influence K^+ concentration [26]. Ca^{2+}/Na^+ exchanger is another factor that could influence Na^+ concentration and subsequently AP generation. Intracellular Na^+ concentration was shown to regulate the intracellular Ca^{2+} stable state through Ca^{2+}/Na^+ exchanger. Also, the exchanger was shown to reverse their direction under normal conditions [114], which raises an interesting question on how it affects neuronal dynamics and its firing pattern.

Cooperativity model that accounts for channels spacing and their influence on conduction velocity

Published cooperative Na⁺ channels models were based on the mean-field approximation, in which the cooperativity strength constant was varied until the model replicates the sharp AP observed in electrophysiological recordings. While these cooperative models can replicate the sharp cortical AP onset, they did not provide insight into the coupled channels' spatial arrangement. Since channel co-localization is a prerequisite for cooperative gating [21], a cooperative Na⁺ channels model that considers the channels spacing is of interest. The model could be constructed to incorporate the cable equation and cooperative model. Although previous studies such as Öz *et al.* (2015) analyzed the impact of cooperative gating in a multicompartment model, the focus will be on continuously varying the intra-channel spacing within a cluster. Moreover, another future project is to investigate the impact of cooperative Na⁺ channels on the velocity of AP propagation. Freeman *et al* found that the density of different Na⁺ channel types changes during neuron maturation [138]. Interestingly, they found that channels clustering accelerate conduction velocity prior to myelination [138]. Thus, studying the effect of somatic cooperative Na⁺ channels on the velocity of AP propagation in myelinated and unmyelinated axons could show another functional role of cooperative gating during maturation.

REFERENCES

- [1] A. L. Hodgkin and A. F. Huxley, “A quantitative description of membrane current and its application to conduction and excitation in nerve,” *J. Physiol.*, vol. 117, no. 4, pp. 500–544, Aug. 1952, doi: 10.1113/jphysiol.1952.sp004764.
- [2] B. Naundorf, F. Wolf, and M. Volgushev, “Unique features of action potential initiation in cortical neurons,” *Nature*, vol. 440, no. 7087, pp. 1060–1063, Apr. 2006, doi: 10.1038/nature04610.
- [3] G. Yu, Y. Shu, and D. A. McCormick, “Cortical action potential backpropagation explains spike threshold variability and rapid-onset kinetics,” *J. Neurosci.*, vol. 28, no. 29, pp. 7260–7272, Jul. 2008, doi: 10.1523/JNEUROSCI.1613-08.2008.
- [4] G. Eyal, H. D. Mansvelder, C. P. J. de Kock, and I. Segev, “Dendrites impact the encoding capabilities of the axon,” *J. Neurosci.*, vol. 34, no. 24, pp. 8063–8071, Jun. 2014, doi: 10.1523/JNEUROSCI.5431-13.2014.
- [5] M. Huang, M. Volgushev, and F. Wolf, “A small fraction of strongly cooperative sodium channels boosts neuronal encoding of high frequencies,” *PLoS One*, vol. 7, no. 5, p. 37629, May 2012, doi: 10.1371/journal.pone.0037629.
- [6] P. Öz, M. Huang, and F. Wolf, “Action potential initiation in a multi-compartmental model with cooperatively gating Na channels in the axon initial segment,” *J. Comput. Neurosci.*, vol. 39, no. 1, pp. 63–75, Aug. 2015, doi: 10.1007/s10827-015-0561-9.
- [7] M. Telenczuk, B. Fontaine, and R. Brette, “The basis of sharp spike onset in standard biophysical models,” *PLoS One*, vol. 12, no. 4, pp. 1–27, Apr. 2017, doi: 10.1371/journal.pone.0175362.
- [8] M. Sekerli, C. A. Del Negro, R. H. Lee, and R. J. Butera, “Estimating action potential thresholds from neuronal time-series: New metrics and evaluation of methodologies,” *IEEE Trans. Biomed. Eng.*, vol. 51, no. 9, pp. 1665–1672, Sep. 2004, doi: 10.1109/TBME.2004.827531.
- [9] M. Volgushev, A. Malyshev, P. Balaban, M. Chistiakova, S. Volgushev, and F. Wolf, “Onset dynamics of action potentials in rat neocortical neurons and identified snail neurons: Quantification of the difference,” *PLoS One*, vol. 3, no. 4, 2008, doi: 10.1371/journal.pone.0001962.
- [10] G. G. De Polavieja, A. Harsch, I. Kleppe, H. P. C. Robinson, and M. Juusola, “Stimulus history reliably shapes action potential waveforms of cortical neurons,” *J. Neurosci.*, vol. 25, no. 23, pp. 5657–5665, Jun. 2005, doi: 10.1523/JNEUROSCI.0242-05.2005.
- [11] D. A. McCormick, B. W. Connors, J. W. Lighthall, and D. A. Prince, “Comparative electrophysiology of pyramidal and sparsely spiny stellate neurons of the neocortex,” *J. Neurophysiol.*, vol. 54, no. 4, pp. 782–806, 1985, doi: 10.1152/jn.1985.54.4.782.
- [12] D. A. Henze and G. Buzsáki, “Action potential threshold of hippocampal pyramidal cells in vivo is increased by recent spiking activity,” *Neuroscience*, vol. 105, no. 1, pp. 121–130, Jul. 2001, doi: 10.1016/S0306-4522(01)00167-1.
- [13] E. Marder and J. M. Goaillard, “Variability, compensation and homeostasis in neuron and network function,” *Nat. Rev. Neurosci.* 2006 77, vol. 7, no. 7, pp. 563–574, Jul. 2006, doi: 10.1038/nrn1949.
- [14] Z. F. Mainen and T. J. Sejnowski, “Reliability of Spike Timing in Neocortical Neurons,” *Science (80-.)*, vol. 268, no. 5216, pp. 1503–1506, 1995.
- [15] Z. F. Mainen and T. J. Sejnowski, “Influence of dendritic structure on firing pattern in model neocortical neurons,” *Nat.* 1996 3826589, vol. 382, no. 6589, pp. 363–366, 1996, doi: 10.1038/382363a0.
- [16] S. Namadurai *et al.*, “Crystal structure and molecular imaging of the Nav channel β 3 subunit indicates a

- trimeric assembly,” *J. Biol. Chem.*, vol. 289, no. 15, pp. 10797–10811, Apr. 2014, doi: 10.1074/jbc.M113.527994.
- [17] J. Clatot *et al.*, “Voltage-gated sodium channels assemble and gate as dimers,” *Nat. Commun.*, vol. 8, no. 1, Dec. 2017, doi: 10.1038/s41467-017-02262-0.
- [18] J. Clatot *et al.*, “Mutant voltage-gated Na⁺ channels can exert a dominant negative effect through coupled gating,” *Am. J. Physiol. Circ. Physiol.*, vol. 315, no. 5, pp. H1250–H1257, Nov. 2018, doi: 10.1152/ajpheart.00721.2017.
- [19] A. H. Rühlmann *et al.*, “Uncoupling sodium channel dimers restores the phenotype of a pain-linked Na_v1.7 channel mutation,” *Br. J. Pharmacol.*, vol. 177, no. 19, p. bph.15196, Aug. 2020, doi: 10.1111/bph.15196.
- [20] E. J. Akin *et al.*, “Single-Molecule Imaging of Na_v1.6 on the Surface of Hippocampal Neurons Reveals Somatic Nanoclusters,” *Biophysj*, vol. 111, pp. 1235–1247, 2016, doi: 10.1016/j.bpj.2016.08.016.
- [21] K.-H. Choi, “Cooperative gating between ion channels,” *Gen. Physiol. Biophys.*, vol. 33, no. 01, pp. 1–12, 2014, doi: 10.4149/gpb_2013076.
- [22] W. Singer and H. Dieter Lux, “Extracellular potassium gradients and visual receptive fields in the cat striate cortex,” *Brain Res.*, vol. 96, no. 2, pp. 378–383, Oct. 1975, doi: 10.1016/0006-8993(75)90751-9.
- [23] F. Amzica and M. Steriade, “Neuronal and Glial Membrane Potentials during Sleep and Paroxysmal Oscillations in the Neocortex,” *J. Neurosci.*, vol. 20, no. 17, pp. 6648–6665, Sep. 2000, doi: 10.1523/JNEUROSCI.20-17-06648.2000.
- [24] L. Felix, D. Ziemens, G. Seifert, and C. R. Rose, “Spontaneous Ultraslow Na⁺ Fluctuations in the Neonatal Mouse Brain,” *Cells 2020, Vol. 9, Page 102*, vol. 9, no. 1, p. 102, Dec. 2019, doi: 10.3390/CELLS9010102.
- [25] C. Perez, L. Felix, S. Durrý, C. R. Rose, and G. Ullah, “On the origin of ultraslow spontaneous Na⁺ fluctuations in neurons of the neonatal forebrain,” <https://doi.org/10.1152/jn.00373.2020>, vol. 125, no. 2, pp. 408–425, Feb. 2021, doi: 10.1152/JN.00373.2020.
- [26] J. R. Cressman, G. Ullah, J. Ziburkus, S. J. Schiff, and E. Barreto, “The influence of sodium and potassium dynamics on excitability, seizures, and the stability of persistent states: I. Single neuron dynamics,” *J. Comput. Neurosci.*, vol. 26, no. 2, pp. 159–170, 2009, doi: 10.1007/s10827-008-0132-4.
- [27] A. A. Aldohbeyb, J. Vigh, and K. L. Lear, “New method to analyze the rapidity of action potential initiation,” *Biomed. Sci. Instrum.*, vol. 56, no. 2, pp. 402–415, 2020.
- [28] A. A. Aldohbeyb, J. Vigh, and K. L. Lear, “New methods for quantifying rapidity of action potential onset differentiate neuron types,” *PLoS One*, vol. 16, no. 4, p. e0247242, 2021, doi: 10.1371/journal.pone.0247242.
- [29] F. Bezanilla, “Ion Channels: From Conductance to Structure,” *Neuron*, vol. 60, no. 3, pp. 456–468, 2008, doi: 10.1016/j.neuron.2008.10.035.
- [30] D. A. McCormick, Y. Shu, and Y. Yu, “Hodgkin and Huxley model - Still standing?,” *Nature*, vol. 445, no. 7123. Nature Publishing Group, 04-Jan-2007, doi: 10.1038/nature05523.
- [31] D. Sato, R. E. Dixon, L. F. Santana, and M. F. Navedo, “A model for cooperative gating of L-type Ca²⁺ channels and its effects on cardiac alternans dynamics,” *PLoS Comput. Biol.*, vol. 14, no. 1, p. 1005906, Jan. 2018, doi: 10.1371/journal.pcbi.1005906.
- [32] G. E. Kim *et al.*, “Human Slack Potassium Channel Mutations Increase Positive Cooperativity between Individual Channels,” *Cell Rep.*, vol. 9, no. 5, pp. 1661–1672, Dec. 2014, doi: 10.1016/j.celrep.2014.11.015.
- [33] R. Siciliano, “The Hodgkin-Huxley Model Its Extensions, Analysis and Numerics,” 2012.
- [34] A. L. Hodgkin, A. F. Huxley, S. L. Cowan, and B. Katz, “Playing the Devil’s advocate: Is the Hodgkin-Huxley model useful?,” *Trends Neurosci.*, vol. 25, no. 11, pp. 558–563, Nov. 2002, doi: 10.1016/S0166-

2236(02)02278-6.

- [35] A. I. Undrovinas, I. A. Fleidervish, and J. C. Makielski, "Inward sodium current at resting potentials in single cardiac myocytes induced by the ischemic metabolite lysophosphatidylcholine.," *Circ. Res.*, vol. 71, no. 5, pp. 1231–1241, Nov. 1992, doi: 10.1161/01.RES.71.5.1231.
- [36] M. L. Molina *et al.*, "Clustering and coupled gating modulate the activity in KcsA, a potassium channel model," *J. Biol. Chem.*, vol. 281, no. 27, pp. 18837–18848, Jul. 2006, doi: 10.1074/jbc.M600342200.
- [37] M. F. Navedo *et al.*, "Increased coupled gating of L-type Ca²⁺ channels during hypertension and timothy syndrome," *Circ. Res.*, vol. 106, no. 4, pp. 748–756, Mar. 2010, doi: 10.1161/CIRCRESAHA.109.213363.
- [38] R. E. Dixon *et al.*, "Graded Ca²⁺/calmodulin-dependent coupling of voltage-gated CaV1.2 channels," *Elife*, vol. 2015, no. 4, Feb. 2015, doi: 10.7554/eLife.05608.
- [39] K. Iwasa, G. Ehrenstein, N. Moran, and M. Jia, "Evidence for interactions between batrachotoxin-modified channels in hybrid neuroblastoma cells," *Biophys. J.*, vol. 50, no. 3, pp. 531–537, 1986, doi: 10.1016/S0006-3495(86)83491-9.
- [40] B. Neumcke and R. Stämpfli, "Alteration of the conductance of Na⁺ channels in the nodal membrane of frog nerve by holding potential and tetrodotoxin," *BBA - Biomembr.*, vol. 727, no. 1, pp. 177–184, Jan. 1983, doi: 10.1016/0005-2736(83)90382-6.
- [41] R. C. Hoyt, "The Squid Giant Axon: Mathematical Models," *Biophys. J.*, vol. 3, no. 5, pp. 399–431, 1963, doi: 10.1016/S0006-3495(63)86829-0.
- [42] R. C. Hoyt, "Sodium Inactivation in Nerve Fibers," *Biophys. J.*, vol. 8, no. 10, pp. 1074–1097, 1968, doi: 10.1016/S0006-3495(68)86540-3.
- [43] R. C. Hoyt and W. J. Adelman, "Sodium Inactivation: Experimental Test of Two Models," *Biophys. J.*, vol. 10, no. 7, pp. 610–617, 1970, doi: 10.1016/S0006-3495(70)86323-8.
- [44] L. Goldman and C. L. Schauf, "Inactivation of the sodium current in myxicola giant axons: Evidence for coupling to the activation process," *J. Gen. Physiol.*, vol. 59, no. 6, pp. 659–675, Jun. 1972, doi: 10.1085/jgp.59.6.659.
- [45] A. Taddese and B. P. Bean, "Subthreshold sodium current from rapidly inactivating sodium channels drives spontaneous firing of tuberomammillary neurons," *Neuron*, vol. 33, no. 4, pp. 587–600, Feb. 2002, doi: 10.1016/S0896-6273(02)00574-3.
- [46] B. P. Bean, "The action potential in mammalian central neurons," *Nat. Rev. Neurosci.*, vol. 8, no. 6, pp. 451–465, Jun. 2007, doi: 10.1038/nrn2148.
- [47] C. M. Armstrong and F. Bezanilla, "Currents related to movement of the gating particles of the sodium channels," *Nature*, vol. 242, no. 5398, pp. 459–461, Apr. 1973, doi: 10.1038/242459a0.
- [48] F. Bezanilla and C. M. Armstrong, "Inactivation of the sodium channel. I. Sodium current experiments.," *J. Gen. Physiol.*, vol. 70, no. 5, pp. 549–66, Nov. 1977, doi: 10.1085/jgp.70.5.567.
- [49] C. M. Armstrong and F. Bezanilla, "Inactivation of the sodium channel: II. gating current experiments," *J. Gen. Physiol.*, vol. 70, no. 5, pp. 567–590, Nov. 1977, doi: 10.1085/jgp.70.5.567.
- [50] R. Horn and C. A. Vandenberg, "Statistical properties of single sodium channels," *J. Gen. Physiol.*, vol. 84, no. 4, pp. 505–534, Oct. 1984, doi: 10.1085/jgp.84.4.505.
- [51] R. W. Aldrich, D. P. Corey, and C. F. Stevens, "A reinterpretation of mammalian sodium channel gating based on single channel recording," *Nature*, vol. 306, no. 5942, pp. 436–441, 1983, doi: 10.1038/306436a0.
- [52] F. Bezanilla, "Gating currents," *J. Gen. Physiol.*, vol. 150, no. 7, 2018, doi: 10.1085/jgp.201812090.
- [53] C. A. Vandenberg and F. Bezanilla, "A sodium channel gating model based on single channel, macroscopic ionic, and gating currents in the squid giant axon," *Biophys. J.*, vol. 60, no. 6, pp. 1511–1533, Dec. 1991,

doi: 10.1016/S0006-3495(91)82186-5.

- [54] B. Chanda, O. K. Asamoah, and F. Bezanilla, “Coupling Interactions between Voltage Sensors of the Sodium Channel as Revealed by Site-specific Measurements,” *J. Gen. Physiol.*, vol. 123, no. 3, pp. 217–230, Mar. 2004, doi: 10.1085/jgp.200308971.
- [55] B. Neumcke and R. Stämpfli, “Sodium currents and sodium-current fluctuations in rat myelinated nerve fibres,” *J. Physiol.*, vol. 329, no. 1, pp. 163–184, Aug. 1982, doi: 10.1113/jphysiol.1982.sp014296.
- [56] G. Baranauskas and M. Martina, “Sodium currents activate without a Hodgkin and Huxley-type delay in central mammalian neurons,” *J. Neurosci.*, vol. 26, no. 2, pp. 671–684, Jan. 2006, doi: 10.1523/JNEUROSCI.2283-05.2006.
- [57] G. Baranauskas, “Ionic channel function in action potential generation: Current perspective,” *Molecular Neurobiology*, vol. 35, no. 2. Humana Press, pp. 129–150, 25-Jul-2007, doi: 10.1007/s12035-007-8001-0.
- [58] D. Debanne, E. Campanac, A. Bialowas, E. Carlier, and G. Alcaraz, “Axon physiology,” *Physiol. Rev.*, vol. 91, no. 2, pp. 555–602, Apr. 2011, doi: 10.1152/physrev.00048.2009.
- [59] R. Brette, “Sharpness of Spike Initiation in Neurons Explained by Compartmentalization,” *PLoS Comput. Biol.*, vol. 9, no. 12, p. e1003338, Dec. 2013, doi: 10.1371/journal.pcbi.1003338.
- [60] B. Naundorf, F. Wolf, and M. Volgushev, “Hodgkin and Huxley model — still standing? (Reply),” *Nature*, vol. 445, no. 7123, pp. E2–E3, 2007, doi: 10.1038/nature05534.
- [61] I. A. Fleidervish, N. Lasser-Ross, M. J. Gutnick, and W. N. Ross, “Na⁺ imaging reveals little difference in action potential-evoked Na⁺ influx between axon and soma,” *Nat. Neurosci.*, vol. 13, no. 7, pp. 852–860, Jul. 2010, doi: 10.1038/nn.2574.
- [62] M. Volgushev, Albert Mukovskiy, and F. Wolf, “The Elusive Action Potential.” 2007.
- [63] G. Baranauskas, A. Mukovskiy, F. Wolf, and M. Volgushev, “The determinants of the onset dynamics of action potentials in a computational model,” *Neuroscience*, vol. 167, no. 4, pp. 1070–1090, 2010, doi: 10.1016/j.neuroscience.2010.02.072.
- [64] V. Ilin, A. Malyshev, F. Wolf, and M. Volgushev, “Fast computations in cortical ensembles require rapid initiation of action potentials,” *J. Neurosci.*, vol. 33, no. 6, pp. 2281–2292, Feb. 2013, doi: 10.1523/JNEUROSCI.0771-12.2013.
- [65] P. Pfeiffer, A. V Egorov, F. Lorenz, J.-H. Schleimer, A. Draguhn, and S. Schreiber, “Clusters of cooperative ion channels enable a membrane-potential-based mechanism for short-term memory,” *Elife*, vol. 9, Feb. 2020, doi: 10.7554/eLife.49974.
- [66] G. P. Krishnan and M. Bazhenov, “Ionic Dynamics Mediate Spontaneous Termination of Seizures and Postictal Depression State,” *J. Neurosci.*, vol. 31, no. 24, pp. 8870–8882, Jun. 2011, doi: 10.1523/JNEUROSCI.6200-10.2011.
- [67] G. Ullah, J. R. Cressman, E. Barreto, and S. J. Schiff, “The influence of sodium and potassium dynamics on excitability, seizures, and the stability of persistent states: II. Network and glial dynamics,” *J. Comput. Neurosci.*, vol. 26, no. 2, pp. 171–183, Dec. 2009, doi: 10.1007/s10827-008-0130-6.
- [68] M. Emin Tagluk and R. Tekin, “The influence of ion concentrations on the dynamic behavior of the Hodgkin-Huxley model-based cortical network,” *Cogn. Neurodyn.*, vol. 8, no. 4, pp. 287–298, 2014, doi: 10.1007/s11571-014-9281-5.
- [69] A. Zylbertal, A. Kahan, Y. Ben-Shaul, Y. Yarom, and S. Wagner, “Prolonged Intracellular Na⁺ Dynamics Govern Electrical Activity in Accessory Olfactory Bulb Mitral Cells,” *PLOS Biol.*, vol. 13, no. 12, p. e1002319, Dec. 2015, doi: 10.1371/journal.pbio.1002319.
- [70] A. Zylbertal, Y. Yarom, and S. Wagner, “The Slow Dynamics of Intracellular Sodium Concentration Increase the Time Window of Neuronal Integration: A Simulation Study,” *Front. Comput. Neurosci.*, vol.

- 11, p. 85, Sep. 2017, doi: 10.3389/fncom.2017.00085.
- [71] X. J. Wang and G. Buzsáki, “Gamma oscillation by synaptic inhibition in a hippocampal interneuronal network model,” *J. Neurosci.*, vol. 16, no. 20, pp. 6402–6413, Oct. 1996, doi: 10.1523/jneurosci.16-20-06402.1996.
- [72] W. Hu, C. Tian, T. Li, M. Yang, H. Hou, and Y. Shu, “Distinct contributions of Nav1.6 and Nav1.2 in action potential initiation and backpropagation,” *Nat. Neurosci.*, vol. 12, no. 8, pp. 996–1002, Aug. 2009, doi: 10.1038/nn.2359.
- [73] M. H. P. Kole and G. J. Stuart, “Is action potential threshold lowest in the axon?,” *Nat. Neurosci.*, vol. 11, no. 11, pp. 1253–1255, Nov. 2008, doi: 10.1038/nn.2203.
- [74] L. J. Colwell and M. P. Brenner, “Action potential initiation in the Hodgkin-Huxley model,” *PLoS Comput. Biol.*, vol. 5, no. 1, Jan. 2009, doi: 10.1371/journal.pcbi.1000265.
- [75] P. Anderson, J. Storm, and H. V. Wheal, “Thresholds of action potentials evoked by synapses on the dendrites of pyramidal cells in the rat hippocampus in vitro.,” *J. Physiol.*, vol. 383, no. 1, pp. 509–526, Feb. 1987, doi: 10.1113/jphysiol.1987.sp016425.
- [76] J. Platkiewicz and R. Brette, “A Threshold Equation for Action Potential Initiation,” *PLoS Comput. Biol.*, vol. 6, no. 7, p. e1000850, Jul. 2010, doi: 10.1371/journal.pcbi.1000850.
- [77] W. B. Wilent and D. Contreras, “Stimulus-dependent changes in spike threshold enhance feature selectivity in rat barrel cortex neurons,” *J. Neurosci.*, vol. 25, no. 11, pp. 2983–2991, Mar. 2005, doi: 10.1523/JNEUROSCI.4906-04.2005.
- [78] A. da Silva Lantyer *et al.*, “Supporting data for “A databank for intracellular electrophysiological mapping of the adult somatosensory cortex.”,” *GigaScience Database*, 2018.
- [79] A. Destexhe and D. Paré, “Impact of network activity on the integrative properties of neocortical pyramidal neurons in vivo,” *J. Neurophysiol.*, vol. 81, no. 4, pp. 1531–1547, 1999, doi: 10.1152/jn.1999.81.4.1531.
- [80] J. R. Huguenard, O. P. Hamill, and D. A. Prince, “Developmental Changes in Na⁺ Conductances in Rat Neocortical Neurons: Appearance of a Slowly Inactivating Component,” 1988.
- [81] F. Faraci, S. Hille, and M. Timme, “The 60th anniversary of the Hodgkin-Huxley model : a critical assessment from a historical and modeller ’ s viewpoint,” 2013.
- [82] M. Pospischil *et al.*, “Minimal Hodgkin-Huxley type models for different classes of cortical and thalamic neurons,” *Biol. Cybern.*, vol. 99, no. 4–5, pp. 427–441, Nov. 2008, doi: 10.1007/s00422-008-0263-8.
- [83] R. R. Llinás, “The intrinsic electrophysiological properties of mammalian neurons: Insights into central nervous system function,” *Science (80-)*, vol. 242, no. 4886, pp. 1654–1664, Dec. 1988, doi: 10.1126/science.3059497.
- [84] B. Hille, *Ionic channels of excitable membranes*, 2nd ed.. Sunderland, Mass.: Sinauer Associates, 1992.
- [85] L. G. Nowak *et al.*, “Electrophysiological Classes of Cat Primary Visual Cortical Neurons In Vivo as Revealed by Quantitative Analyses,” 2003, doi: 10.1152/jn.00580.2002.
- [86] M. Volgushev, A. Mukovskiy, and F. Wolf, “The Elusive Action Potential,” 2007.
- [87] S. H. Lee, M. Krook-Magnuson, Esther Bezaire, and I. Soltesz, “Intracellular, in vitro somatic membrane potential recordings from whole cell patch clamped rodent hippocampal CA1 neurons,” *CRCNS.org*, 2016.
- [88] S. H. Lee *et al.*, “Parvalbumin-positive basket cells differentiate among hippocampal pyramidal cells,” *Neuron*, vol. 82, no. 5, pp. 1129–1144, Jun. 2014, doi: 10.1016/j.neuron.2014.03.034.
- [89] T. Tateno, A. Harsch, and H. P. C. Robinson, “Threshold firing frequency-current relationships of neurons in rat somatosensory cortex: Type 1 and type 2 dynamics,” *J. Neurophysiol.*, vol. 92, no. 4, pp. 2283–2294, Oct. 2004, doi: 10.1152/jn.00109.2004.

- [90] M. C. Meyer, *Probability and mathematical statistics theory, applications, and practice in R*. Philadelphia: Society for Industrial and Applied Mathematics, 2019.
- [91] H. Hentschke and M. C. Stüttgen, “Computation of measures of effect size for neuroscience data sets,” *Eur. J. Neurosci.*, vol. 34, no. 12, pp. 1887–1894, Dec. 2011, doi: 10.1111/j.1460-9568.2011.07902.x.
- [92] N. Spruston, “Pyramidal neurons: Dendritic structure and synaptic integration,” *Nature Reviews Neuroscience*, vol. 9, no. 3. Nature Publishing Group, pp. 206–221, Mar-2008, doi: 10.1038/nrn2286.
- [93] J. M. Bekkers, “Pyramidal neurons,” *Current Biology*, vol. 21, no. 24. Cell Press, p. R975, 20-Dec-2011, doi: 10.1016/j.cub.2011.10.037.
- [94] B. C. Carter and B. P. Bean, “Sodium Entry during Action Potentials of Mammalian Neurons: Incomplete Inactivation and Reduced Metabolic Efficiency in Fast-Spiking Neurons,” *Neuron*, vol. 64, no. 6, pp. 898–909, Dec. 2009, doi: 10.1016/j.neuron.2009.12.011.
- [95] P. L. Watson, J. L. Weiner, and P. L. Carlen, “Effects of variations in hippocampal slice preparation protocol on the electrophysiological stability, epileptogenicity and graded hypoxia responses of CA1 neurons,” *Brain Res.*, vol. 775, no. 1–2, pp. 134–143, Nov. 1997, doi: 10.1016/S0006-8993(97)00893-7.
- [96] J. C. Pineda, R. S. Waters, and R. C. Foehring, “Specificity in the Interaction of HVA Ca²⁺ Channel Types With Ca²⁺-Dependent AHPs and Firing Behavior in Neocortical Pyramidal Neurons,” *J. Neurophysiol.*, vol. 79, no. 5, pp. 2522–2534, May 1998, doi: 10.1152/jn.1998.79.5.2522.
- [97] J. C. F. Lee, J. C. Callaway, and R. C. Foehring, “Effects of temperature on calcium transients and Ca²⁺-dependent afterhyperpolarizations in neocortical pyramidal neurons,” *J. Neurophysiol.*, vol. 93, no. 4, pp. 2012–2020, Apr. 2005, doi: 10.1152/jn.01017.2004.
- [98] G. J. Kress, M. J. Dowling, J. P. Meeks, and S. Mennerick, “High Threshold, Proximal Initiation, and Slow Conduction Velocity of Action Potentials in Dentate Granule Neuron Mossy Fibers,” *J. Neurophysiol.*, vol. 100, no. 1, pp. 281–291, Jul. 2008, doi: 10.1152/jn.90295.2008.
- [99] M. H. Kole and R. Brette, “The electrical significance of axon location diversity,” *Curr. Opin. Neurobiol.*, vol. 51, pp. 52–59, Aug. 2018, doi: 10.1016/J.CONB.2018.02.016.
- [100] M. S. Hamada, S. Goethals, S. I. De Vries, R. Brette, and M. H. P. Kole, “Covariation of axon initial segment location and dendritic tree normalizes the somatic action potential,” *Proc. Natl. Acad. Sci. U. S. A.*, vol. 113, no. 51, pp. 14841–14846, Dec. 2016, doi: 10.1073/pnas.1607548113.
- [101] J. Wang, S.-W. Ou, and Y.-J. Wang, “Distribution and function of voltage-gated sodium channels in the nervous system,” 2017, doi: 10.1080/19336950.2017.1380758.
- [102] M. Avermann, C. Tamm, C. Mateo, W. Gerstner, and C. C. H. Petersen, “Microcircuits of excitatory and inhibitory neurons in layer 2/3 of mouse barrel cortex,” *J. Neurophysiol.*, vol. 107, no. 11, pp. 3116–3134, Jun. 2012, doi: 10.1152/jn.00917.2011.
- [103] B. N. Routh, D. Johnston, K. Harris, and R. A. Chitwood, “Anatomical and Electrophysiological Comparison of CA1 Pyramidal Neurons of the Rat and Mouse,” *J. Neurophysiol.*, vol. 102, no. 4, pp. 2288–2302, Oct. 2009, doi: 10.1152/jn.00082.2009.
- [104] C. C. Lien and P. Jonas, “Kv3 potassium conductance is necessary and kinetically optimized for high-frequency action potential generation in hippocampal interneurons,” *J. Neurosci.*, vol. 23, no. 6, pp. 2058–2068, Mar. 2003, doi: 10.1523/jneurosci.23-06-02058.2003.
- [105] K. A. Pelkey, R. Chittajallu, M. T. Craig, L. Tricoire, J. C. Wester, and C. J. McBain, “Hippocampal gabaergic inhibitory interneurons,” *Physiol. Rev.*, vol. 97, no. 4, pp. 1619–1747, Oct. 2017, doi: 10.1152/physrev.00007.2017.
- [106] J. Kim, D.-S. Wei, and D. A. Hoffman, “Kv4 potassium channel subunits control action potential repolarization and frequency-dependent broadening in rat hippocampal CA1 pyramidal neurones,” *J. Physiol.*, vol. 569, no. 1, pp. 41–57, Nov. 2005, doi: 10.1113/jphysiol.2005.095042.

- [107] M. Martina and P. Jonas, “Functional differences in Na⁺ channel gating between fast-spiking interneurons and principal neurons of rat hippocampus,” *J. Physiol.*, vol. 505, no. 3, pp. 593–603, Dec. 1997, doi: 10.1111/j.1469-7793.1997.593ba.x.
- [108] R. Brette, “What Is the Most Realistic Single-Compartment Model of Spike Initiation?,” *PLoS Comput. Biol.*, vol. 11, no. 4, pp. 1–13, 2015, doi: 10.1371/journal.pcbi.1004114.
- [109] J. V. Raimondo, R. J. Burman, A. A. Katz, and C. J. Akerman, “Ion dynamics during seizures,” *Front. Cell. Neurosci.*, vol. 0, no. OCTOBER, p. 419, Oct. 2015, doi: 10.3389/FNCEL.2015.00419.
- [110] S. J. Clapcote *et al.*, “Mutation I810N in the alpha3 isoform of Na⁺,K⁺-ATPase causes impairments in the sodium pump and hyperexcitability in the CNS,” *Proc. Natl. Acad. Sci. U. S. A.*, vol. 106, no. 33, pp. 14085–14090, Aug. 2009, doi: 10.1073/PNAS.0904817106.
- [111] V. Gnatkovsky, L. Librizzi, F. Trombin, and M. De Curtis, “Fast activity at seizure onset is mediated by inhibitory circuits in the entorhinal cortex in vitro,” *Ann. Neurol.*, vol. 64, no. 6, pp. 674–686, Dec. 2008, doi: 10.1002/ANA.21519.
- [112] K. M. Igelström, “Is slack an intrinsic seizure terminator?,” *Neuroscientist*, vol. 19, no. 3, pp. 248–254, Jun. 2013, doi: 10.1177/1073858412446311.
- [113] A. J. Trevelyan, D. Sussillo, and R. Yuste, “Feedforward Inhibition Contributes to the Control of Epileptiform Propagation Speed,” *J. Neurosci.*, vol. 27, no. 13, pp. 3383–3387, Mar. 2007, doi: 10.1523/JNEUROSCI.0145-07.2007.
- [114] G. P. Krishnan, G. Filatov, A. Shilnikov, and M. Bazhenov, “Electrogenic properties of the Na⁺/K⁺ ATPase control transitions between normal and pathological brain states,” <https://doi.org/10.1152/jn.00460.2014>, vol. 113, no. 9, pp. 3356–3374, May 2015, doi: 10.1152/JN.00460.2014.
- [115] B. S. Gutkin, C. R. Laing, C. L. Colby, C. C. Chow, and G. B. Ermentrout, “Turning On and Off with Excitation: The Role of Spike-Timing Asynchrony and Synchrony in Sustained Neural Activity,” *J. Comput. Neurosci.* 2001 112, vol. 11, no. 2, pp. 121–134, 2001, doi: 10.1023/A:1012837415096.
- [116] M. H. Higgs and W. J. Spain, “Conditional Bursting Enhances Resonant Firing in Neocortical Layer 2–3 Pyramidal Neurons,” *J. Neurosci.*, vol. 29, no. 5, pp. 1285–1299, Feb. 2009, doi: 10.1523/JNEUROSCI.3728-08.2009.
- [117] M. B. Jackson, A. Konnerth, and G. J. Augustine, “Action potential broadening and frequency-dependent facilitation of calcium signals in pituitary nerve terminals,” *Proc. Natl. Acad. Sci.*, vol. 88, no. 2, pp. 380–384, Jan. 1991, doi: 10.1073/PNAS.88.2.380.
- [118] R. Gillette, M. U. Gillette, and W. J. Davis, “Action-potential broadening and endogenously sustained bursting are substrates of command ability in a feeding neuron of Pleurobranchaea,” <https://doi.org/10.1152/jn.1980.43.3.669>, vol. 43, no. 3, pp. 669–685, 1980, doi: 10.1152/JN.1980.43.3.669.
- [119] J. R. P. Geiger and P. Jonas, “Dynamic control of presynaptic Ca²⁺ inflow by fast-inactivating K⁺ channels in hippocampal mossy fiber boutons,” *Neuron*, vol. 28, no. 3, pp. 927–939, 2000, doi: 10.1016/S0896-6273(00)00164-1.
- [120] J. V. Le Bé, G. Silberberg, Y. Wang, and H. Markram, “Morphological, Electrophysiological, and Synaptic Properties of Corticocallosal Pyramidal Cells in the Neonatal Rat Neocortex,” *Cereb. Cortex*, vol. 17, no. 9, pp. 2204–2213, Sep. 2007, doi: 10.1093/CERCOR/BHL127.
- [121] I. M. Raman, L. K. Sprunger, M. H. Meisler, and B. P. Bean, “Altered subthreshold sodium currents and disrupted firing patterns in Purkinje neurons of Scn8a mutant mice,” *Neuron*, vol. 19, no. 4, pp. 881–891, 1997, doi: 10.1016/S0896-6273(00)80969-1.
- [122] G. Stuart and B. Sakmann, “Amplification of EPSPs by axosomatic sodium channels in neocortical pyramidal neurons,” *Neuron*, vol. 15, no. 5, pp. 1065–1076, 1995, doi: 10.1016/0896-6273(95)90095-0.
- [123] M. H. P. Kole, S. U. Ilschner, B. M. Kampa, S. R. Williams, P. C. Ruben, and G. J. Stuart, “Action potential

- generation requires a high sodium channel density in the axon initial segment,” *Nat. Neurosci.*, vol. 11, no. 2, pp. 178–186, 2008, doi: 10.1038/nn2040.
- [124] R. Azouz and C. M. Gray, “Dynamic spike threshold reveals a mechanism for synaptic coincidence detection in cortical neurons in vivo,” *Proc. Natl. Acad. Sci. U. S. A.*, vol. 97, no. 14, pp. 8110–8115, Jul. 2000, doi: 10.1073/PNAS.130200797/ASSET/869CA2DD-DE8B-4046-9516-50F39786E1B5/ASSETS/GRAPHIC/PQ1302007005.JPEG.
- [125] G. Ullah, Y. Wei, M. A. Dahlem, M. Wechselberger, and S. J. Schiff, “The Role of Cell Volume in the Dynamics of Seizure, Spreading Depression, and Anoxic Depolarization,” *PLOS Comput. Biol.*, vol. 11, no. 8, p. e1004414, Aug. 2015, doi: 10.1371/JOURNAL.PCBI.1004414.
- [126] K. Iwasa, I. Tasaki, and R. C. Gibbons, “Swelling of Nerve Fibers Associated with Action Potentials,” *Science (80-.)*, vol. 210, no. 4467, pp. 338–339, 1980.
- [127] A. R. Kay, “How cells can control their size by pumping ions,” *Front. Cell Dev. Biol.*, vol. 5, no. MAY, May 2017, doi: 10.3389/FCELL.2017.00041/FULL.
- [128] C. Devin Brisson and R. David Andrew, “A neuronal population in hypothalamus that dramatically resists acute ischemic injury compared to neocortex,” *J. Neurophysiol.*, vol. 108, no. 2, pp. 419–430, Jul. 2012, doi: 10.1152/JN.00090.2012/ASSET/IMAGES/LARGE/Z9K0131214390008.JPEG.
- [129] R. D. Andrew, M. W. Labron, S. E. Boehnke, L. Carnduff, and S. A. Kirov, “Physiological evidence that pyramidal neurons lack functional water channels,” *Cereb. Cortex*, vol. 17, no. 4, pp. 787–802, Apr. 2007, doi: 10.1093/CERCOR/BHK032.
- [130] C. Vaillend, S. E. Mason, M. F. Cuttle, and B. E. Alger, “Mechanisms of neuronal hyperexcitability caused by partial inhibition of Na⁺-K⁺-ATPases in the rat CA1 hippocampal region,” *J. Neurophysiol.*, vol. 88, no. 6, pp. 2963–2978, Dec. 2002, doi: 10.1152/JN.00244.2002.
- [131] L. R. Shao, R. Janicot, and C. E. Stafstrom, “Na⁺-K⁺-ATPase functions in the developing hippocampus: Regional differences in CA1 and CA3 neuronal excitability and role in epileptiform network bursting,” *J. Neurophysiol.*, vol. 125, no. 1, pp. 1–11, Jan. 2021, doi: 10.1152/JN.00453.2020.
- [132] E. J. Akin *et al.*, “Single-Molecule Imaging of Nav1.6 on the Surface of Hippocampal Neurons Reveals Somatic Nanoclusters,” *Biophys. J.*, 2016, doi: 10.1016/j.bpj.2016.08.016.
- [133] M. S. Goldman, J. Golowasch, E. Marder, and L. F. Abbott, “Global Structure, Robustness, and Modulation of Neuronal Models,” *J. Neurosci.*, vol. 21, no. 14, pp. 5229–5238, 2001.
- [134] L. Solé, J. L. Wagnon, and M. M. Tamkun, “Functional analysis of three Nav1.6 mutations causing early infantile epileptic encephalopathy,” *Biochim. Biophys. Acta - Mol. Basis Dis.*, vol. 1866, no. 12, p. 165959, Dec. 2020, doi: 10.1016/j.bbdis.2020.165959.
- [135] R. E. Tooker *et al.*, “Nitric oxide mediates activity-dependent plasticity of retinal bipolar cell output via S-nitrosylation,” *J. Neurosci.*, vol. 33, no. 49, pp. 19176–19193, Dec. 2013, doi: 10.1523/JNEUROSCI.2792-13.2013.
- [136] L. Felix, A. Delekate, G. C. Petzold, and C. R. Rose, “Sodium Fluctuations in Astroglia and Their Potential Impact on Astrocyte Function,” *Front. Physiol.*, vol. 11, p. 871, Aug. 2020, doi: 10.3389/FPHYS.2020.00871.
- [137] B. Moshrefi-Ravasdjani, D. Ziemens, N. Pape, M. Färfers, and C. R. Rose, “Action Potential Firing Induces Sodium Transients in Macroglial Cells of the Mouse Corpus Callosum,” *Neuroglia 2018, Vol. 1, Pages 106-125*, vol. 1, no. 1, pp. 106–125, Jul. 2018, doi: 10.3390/NEUROGLIA1010009.
- [138] S. A. Freeman *et al.*, “Acceleration of conduction velocity linked to clustering of nodal components precedes myelination,” *Proc. Natl. Acad. Sci. U. S. A.*, vol. 112, no. 3, pp. E321–8, Jan. 2015, doi: 10.1073/pnas.1419099112.
- [139] Z. F. Mainen, J. Joerges, J. R. Huguenard, and T. J. Sejnowski, “A Model of Spike Initiation in Neocortical

- Pyramidal Neurons,” *Neuron*, vol. 15, pp. 1427–1439, 1995.
- [140] M. J. Bezaire and I. Soltesz, “Quantitative assessment of CA1 local circuits: Knowledge base for interneuron-pyramidal cell connectivity,” *Hippocampus*, vol. 23, no. 9, pp. 751–785, Sep. 2013, doi: 10.1002/hipo.22141.
- [141] M. J. Bezaire, I. Raikov, K. Burk, D. Vyas, and I. Soltesz, “Interneuronal mechanisms of hippocampal theta oscillations in a full-scale model of the rodent CA1 circuit,” *Elife*, vol. 5, no. DECEMBER2016, Dec. 2016, doi: 10.7554/eLife.18566.
- [142] A. A. Aldohbeyb, J. Vigh, and K. L. Lear, “No Title,” *Biomed. Sci. Instrum.*, vol. 56, no. 2, p. 20, 2020.
- [143] Z. M. Khaliq and I. M. Raman, “Relative contributions of axonal and somatic Na channels to action potential initiation in cerebellar purkinje neurons,” *J. Neurosci.*, vol. 26, no. 7, pp. 1935–1944, Feb. 2006, doi: 10.1523/JNEUROSCI.4664-05.2006.
- [144] R. M. Takeuchi, “An analysis of neuronal networks with recurrent excitation,” ProQuest Information & Learning, 2018.
- [145] M. Huang, M. Volgushev, and F. Wolf, “File S1 - A Small Fraction of Strongly Cooperative Sodium Channels Boosts Neuronal Encoding of High Frequencies,” 2012, doi: 10.1371/journal.pone.0037629.s001.
- [146] R. D. Traub and R. Miles, *Neuronal Networks of the Hippocampus*. Cambridge University Press, 1991.
- [147] C. Koch and I. Segev, *Methods in neuronal modeling : from synapses to networks*. MIT Press, 1989.
- [148] A. da Silva Lantyer *et al.*, “A databank for intracellular electrophysiological mapping of the adult somatosensory cortex,” *Gigascience*, vol. 7, no. 12, pp. 1–9, Dec. 2018, doi: 10.1093/gigascience/giy147.
- [149] P. Moin, *Fundamentals of engineering numerical analysis*, vol. 9780521884327. Cambridge University Press, 2010.

Appendix A: Supporting information for neuron classification (published)

Appendix A contains the supporting information published with the PLOS One paper.

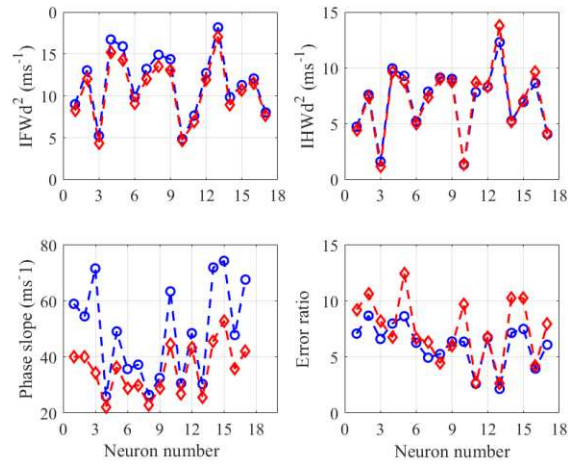


Figure S1: Pooled mean values for hippocampal pyramidal neuron rapidity. The first 9 neurons are deep pyramidal neurons, while the following 8 neurons are superficial pyramidal neurons. Blue circle: values using *spline* interpolation. Red diamond: values using *pchip* interpolation.

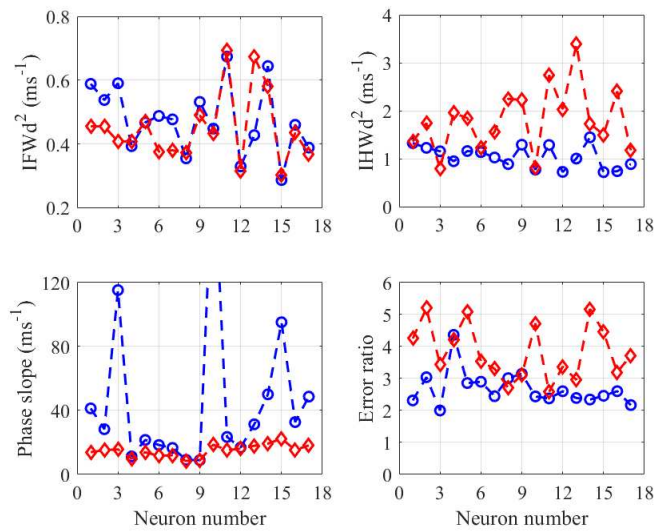


Figure S2: Pooled standard deviation values for hippocampal pyramidal neuron rapidity. The first 9 neurons are deep pyramidal neurons, while the following 8 neurons are superficial pyramidal neurons. Blue circle: values using *spline* interpolation. Red diamond: values using *pchip* interpolation.

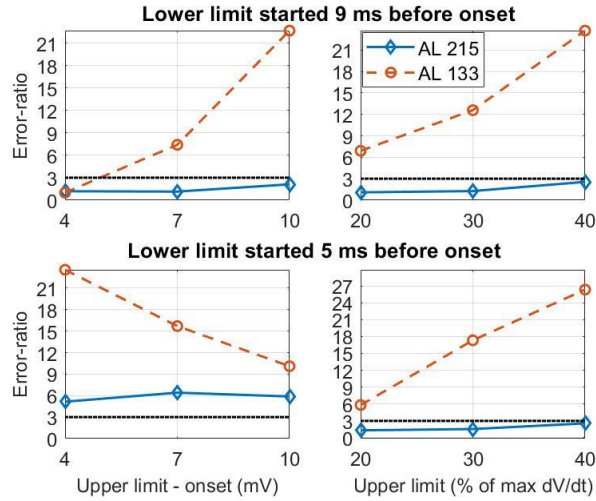


Figure S3: The effect on the error ratio of changing the upper and lower limits of data selection is compared for two neurons. Top left: the error-ratio value when the upper limit was set at varying voltages above onset potential and the lower limit was 9 ms before onset. Top right: the error-ratio value when the upper limit was set at varying percentages of the maximum \dot{V}_m and the lower limit was 9 ms before onset. Bottom left: the error-ratio value when the upper limit was set at varying absolute voltages above onset potential and the lower limit was 5 ms before onset. Bottom right: the error-ratio value when the upper limit was set at varying percentages of the maximum \dot{V} and the lower limit was 5 ms before onset. Blue diamonds represent the error ratio for the neuron labeled AL 133, and orange circles represent the error ratio for the neuron labeled AL 215 [19].

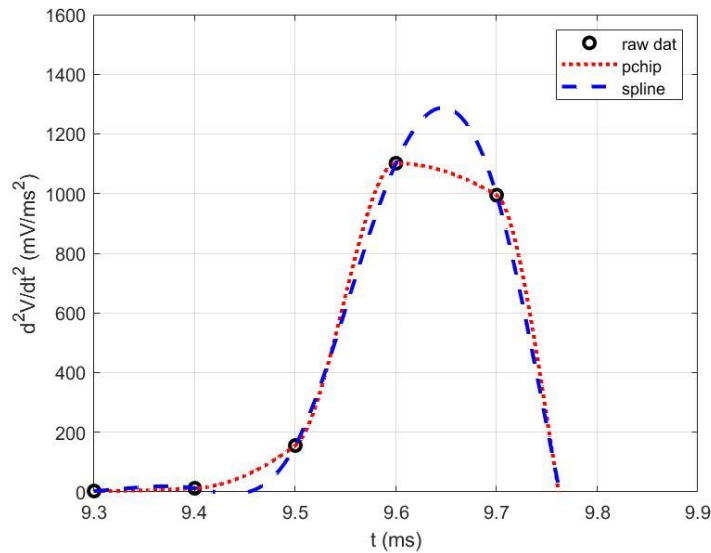


Figure S4: The impact of interpolation function on the shape and thus height of the \ddot{V}_m peak. Black circles represent the \ddot{V}_m points calculated from the raw recordings before applying any interpolation functions. The dotted red line shows the \ddot{V}_m trace after applying the quadratic regression interpolation function (*pchip*), while the dashed blue line shows the \ddot{V}_m trace after applying the cubic spline interpolation function (*spline*)

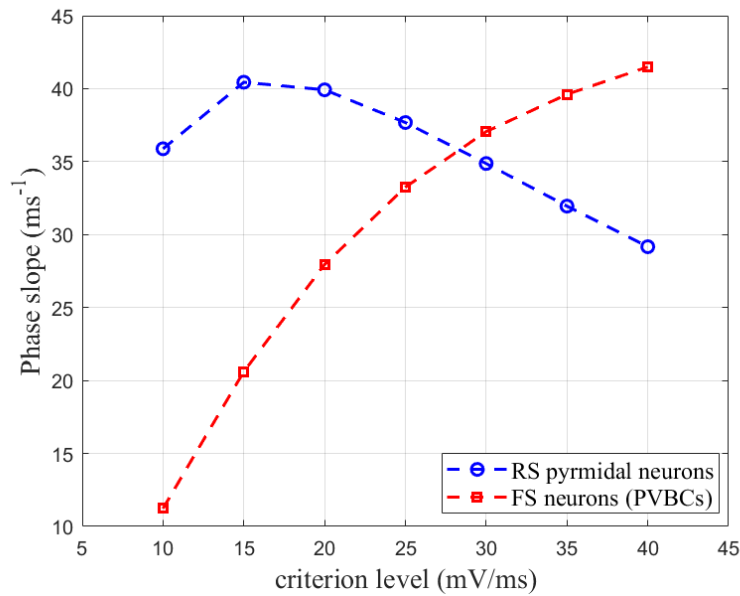


Figure S5: The impact of the onset criterion level on the phase slope for hippocampal neurons. Blue circles show the mean phase slope value at different criterion levels for the hippocampal RS pyramidal neurons. Red squares show the mean phase slope value at different criterion levels for the hippocampal FS PVBCs. All APs that have maximum \dot{V}_m less than 45 mV/ms were excluded. Note that the rapidity for RS and FS hippocampal neurons cross using the phase slope method.

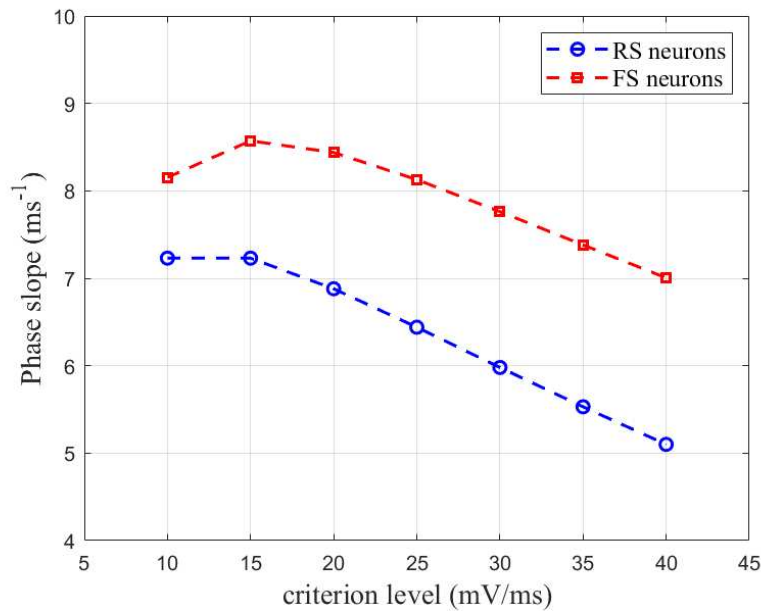


Figure S6: The impact of the onset criterion level on the phase slope for cortical neurons. Blue circles show the mean phase slope value at different criterion levels for the cortical RS pyramidal neurons. Red squares show the mean phase slope value at different criterion levels for the cortical FS neurons. All APs that have maximum \dot{V}_m less than 45 mV/ms were excluded.

Table S1: Electrophysiological properties using the pooled mean and standard deviation

	Cortex				Hippocampus			
	RS	FS	t	d	RS	FS	t	d
n	27	7	----	----	17	6	----	----
IFWd² (ms ⁻¹)	2.1 ±0.3	2.7± 0.2	4.94 ^e *	2.38	4.3 ±0.5	6.9 ±0.4	11.29 ^{e*}	5.61
IHWd² (ms ⁻¹)	4.0 ±0.5	4.6 ± 0.3	2.91 ^e *	1.41	7.2 ±1.1	12.1 ±1.0	9.18 ^{e*}	4.75
Phase Slope (ms ⁻¹)	6.9 ±1.3	8.1 ± 1.1	2.27 ^e *	1.00	47.8 ±64.6	10.4 ±4.5	2.37 [*]	0.82
					35.2±15.2 ^a	11.1 ±4.6 ^a	5.75 [*]	2.15
Error ratio (dimensionless)	7.9 ±6.4	11.2 ±7.5	1.85 ^e	0.48	6.1 ±2.7	0.7 ±0.5	7.92 [*]	2.79
					8.5 ±2.5 ^b	8.5 ±2.8 ^b	0.00 ^e	0.01
Amplitude (mV)	61.7 ±8. 6	58.0 ±5.2	1.06 ^e	0.51	67.5 ±5.3	48.9 ±2.1	11.96 *	4.58
Width (ms)	2.0 ±0.3	0.8 ± 0.1	19.0 2 [*]	5.59	1.6 ±0.4	0.3 ±0.01	13.81 *	4.74
Onset potential (mV)	- 26.3±6. 0	- 39.5±3. 3	5.56 ^e *	2.74	-30.2 ±3.5	-33.4 ±1.1	3.30 [*]	1.23

All data are expressed as mean ± SD. The RS neurons is pyramidal neuron, and the FS hippocampal neurons are PVBCs. ^a using piecewise cubic interpolation. ^b the upper limit was set to 3 mV above the onset. * the difference is significant at p<0.05. d is the Cohen's d effect size, and t is the t-score. For the t-score, ^e indicate that the equal variance hypothesis was accepted.

Table S2: Two-tailed p-value from the t-score between the IFWd² values from different neuron types, and Cohen's d effect size (in parentheses). Green cells indicate a p-value below 0.05.

AP width		Cortex		Hippocampus	
		PCs	FS	PCs	PVBCs
Cortex	PCs		<0.0001 (2.34)	<0.0001 (1.46)	<0.0001 (3.04)
	FS	<0.0001 (2.34)		<0.0001 (3.08)	<0.0001 (4.09)
Hippocampus	PCs	<0.0001 (1.46)	<0.0001 (3.08)		<0.0001 (5.53)
	PVBCs	<0.0001 (3.04)	<0.0001 (4.09)	<0.0001 (5.53)	

Appendix B: Supporting information for neuron classification (not published)

Appendix B contains some of the results and analysis related to the PLOS One paper (chapter 3), but it was not part of the published paper. Also, it contains extra analysis such as using outlier detection methods on the recordings, which was not part of paper. The extra analysis was done after the paper was published.

Error ratio Quantification

The error ratio was calculated in four steps. First, the AP peak and the maximum \dot{V} value. Second, the AP onset voltage was defined as the voltage at the best breaking points of a continuous piecewise linear function (Eq. 4) fitted to the AP trace 5 ms from its peak to 0.1 ms before peaking. Third, using the identified AP onset, the AP portion in the phase plot was selected to be 5 ms before the onset voltage to either 20-30% of the maximum \dot{V} value or 3-10 mV above onset. Finally, the selected portion in the phase plot was fitted to an exponential function and continuous piecewise linear function. The error ratio value is defined as the mean square error (MSE) of the exponential fit to the MSE of the continuous piecewise linear fit.

The exponential fit function was set to be:

$$y = a + \exp(c \times (x + b)) \quad (\text{Eq. 1})$$

Here we used MATLAB *fit* function with initial guess for the three parameters a , b , and c . The initial guess was obtained using MATLAB *exp1* fit function. The *exp1* function is define as $y_{exp1} = a_{exp1} \times \exp(b_{exp1} \times x)$. We fit the selected AP portion on the phase plot to *exp1*. Then, we assumed that at the beginning:

- $c = b_{exp1}$

- $b = 0$
- $a + \exp(cx(1)) = \exp(b_{exp1}x(1))$

Thus,

$$a = y(1) - \exp(b_{exp1}x(1))$$

$$b = x(1) - \frac{\ln(|x(1)|) - \ln(|a|)}{c}$$

Although these initial guesses for a , b , and c might not be accurate, it provides a good starting point to solve the exponential fit function and find the best values that minimize the MSE of the exponential function from the data points. We used this approach instead of solving the exponential fit function with predetermined value of the parameter c because it requires significantly less computation time and provide smaller MSE value.

The continuous piecewise linear fit function was set to be:

$$y = \begin{cases} a_1x + b_1 & 0 < x < C \\ a_2x + b_2 & C < x < X_{max} \end{cases} \quad (\text{Eq. 4})$$

Where C is the breaking point between the two linear fit, at which two linear parts converge, and X_{max} is the maximum value of the breaking point. The remaining parameters was calculated using MATLAB *polyfit* (the first order polynomial fit) for the first line. for fitting the second line, we used the first order MATLAB *polyfix* function, which is a polynomial fit but ensure that the second line fit is continuous to the first fit.

Impact of the data selection on the error ratio

The choice of the upper limit can alter the error ratio value. The impact of the upper limit can be demonstrated by comparing two neurons, one showing the slowest AP onset using all quantification methods (labelled AL 215 which is neuron number 10 in figure 2), and another

neuron showing a fast AP onset (labelled AL 133 which is neuron number 1 in figure 2) by all the quantification methods. The difference in AP onset dynamics can be clearly seen in the phase plot of the average AP for the two neurons (Fig. B1).

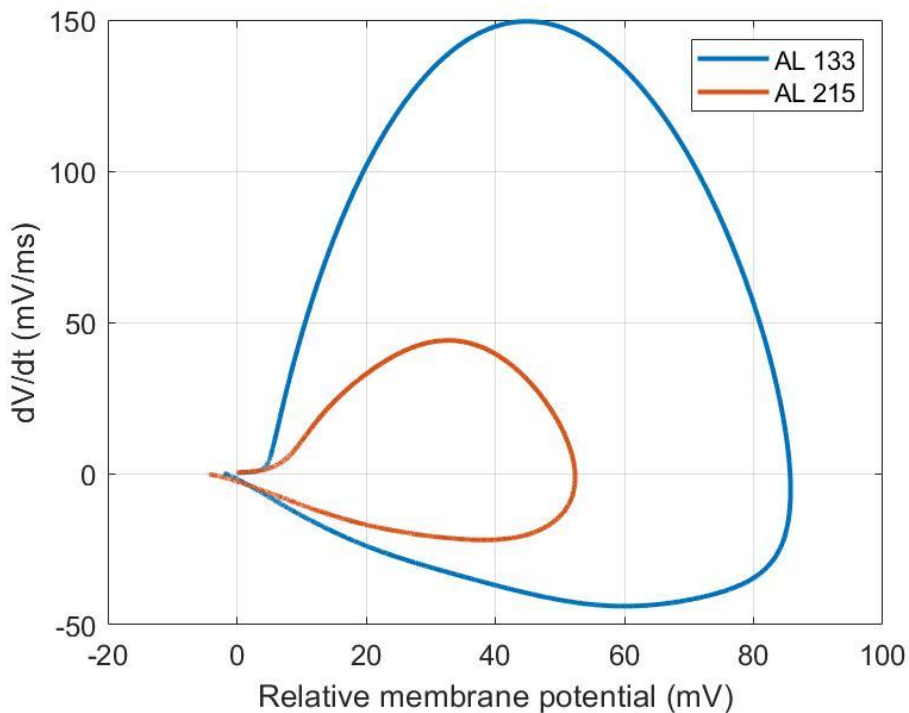


Figure B1: phase plot of averaged APs from two neurons. AL 133 and AL 215 represents the neurons labels in the GigaScience Database [19].

The slowness of the neuron labeled AL 215 is clear with the error ratio method where the error ratio is 1.5, which is about 80 % below the average rapidity of all the RS neurons analyzed here. For the fast AL133 neuron, the error ratio is 17.3, which is more than double the average value. When changing the selected AP portion for fitting, the error ratio value can be significantly altered with neurons exhibiting fast AP onset but has a lower impact on neurons with a slow onset neuron. For example, while setting the lower limit to be 9 ms before onset potential, the mean error ratio the neuron labeled AL133 varied from around 7 to 22 as the upper limit of the fitted

portion was varied from 20% to 40% of the maximum \dot{V} . In contrast, the mean error ratio for a slow neuron is minimally impacted by the choice of the upper limit, in most cases. For example, changing the upper limit only increases the error ratio value from around 1 to less than 3, whereas the only significant change is observed when the lower limit was set to be 5 ms before the onset and the upper limit to be more than 3 mV above onset (Fig. S3 bottom left). Thus, these results show the huge impact of the limit of AP portion on the error ratio value, and hence its implication on categorizing a neuron as having a fast or slow onset.

The lack of distinguishability between the different neuron types using the error ratio could be because the error-ratio method is more like a binary method that can indicate whether the rapidity of AP onset is slow or fast, but not a continuous range in the same way as the other methods. Therefore, the error ratio can indicate the dividing line separating slow and fast onset for the other quantification methods. For that, here we can use the AP rapidity of the neurons with slowest onset (AL 215) as the dividing line. These values correspond to 1.2 ms^{-1} using the IFWd² method, 2.0 ms^{-1} using the IHWD² method, and 2.8 ms^{-1} using the phase slope method.

Differences among hippocampal pyramidal neurons

The PV+ basket cells have been found to evoke greater inhibition to the deep pyramidal neurons while receiving more frequent excitation from the superficial pyramidal neurons [88]. Here, we looked at the electrophysiological properties of these subpopulation of the hippocampal pyramidal neurons. The results show that the hippocampal pyramidal neurons have the same electrophysiological properties despite their location. Although, the deep pyramidal hippocampal neurons show slightly higher AP amplitude, rapidity and lower AP onset voltage and width than the pyramidal superficial neurons, but the difference is not significant. Also, for the hippocampal pyramidal neurons, we did another analysis that included the APs that were separated by less than

30 ms (the new limit was set to 12 ms (see Methods)). The 30 ms separation limit between APs was chosen as the onset potential of two APs with short inter-spike-intervals, ISI, (<25 ms) between them are substantially different [6]. Changing ISI lead to increase the APs analyzed in each recording by around 34 APs, on average. Nonetheless, including these APs did not cause any significant difference for all the electrophysiological properties as shown in Table B1. Thus, regardless of the time limit between the APs, the hippocampal pyramidal neurons show similar electrophysiological properties in the data analyzed here.

Table B1: Comparison between deep and superficial PCs with 12 and 30 ms ISI.

PCs location	ISI (ms)	IFWd ² (ms)	IHWd ² (ms)	Phase slope (ms)	Amplitude (mV)	Width (ms)	Onset (mV)	APs
superficial	30	4.1 ± 0.5	7.1 ± 1.0	53.4 ± 86.7	65.1 ± 5.9	1.7 ± 0.4	-28.8 ± 4.3	131
	12	4.1 ± 0.5	7.2 ± 1.0	50.1 ± 199	65.1 ± 5.7	1.7 ± 0.4	-28.7 ± 4.1	174
deep	30	4.5 ± 0.5	7.3 ± 1.2	43.3 ± 38.9	69.3 ± 4.9	1.5 ± 0.3	-31.3 ± 2.8	146
	12	4.5 ± 0.4	7.3 ± 1.0	43.7 ± 27.6	69.5 ± 4.5	1.6 ± 0.3	-31.4 ± 2.6	172

AP onset potential quantification methods

The definition of AP onset potential is a subjective process [8], where multiple methods are used to estimate AP onset potential. One of the most common method define the AP onset potential as the point at which the AP rate of change exceed a certain value [2], [3], [5]. Other definitions used the potential correspond to the maximum \ddot{V} [139], the maximum \ddot{V} value [12], or

the best breaking point of continuous piecewise linear function (AP BP in Table B2) [9]. Also, we define the AP onset potential as the potential correspond the best breaking point of continuous piecewise linear function on the phase slope (phase plot BP in Table B2). Here, we apply these five quantification methods to the hippocampal and cortical neurons and compare the results. Table B2 summarize the results of the five AP onset potential quantification methods.

Table B2: Comparison of the AP onset potential quantification methods.

methods	sPCs (hipp.)	dPCs (hipp.)	PVBCs (hipp.)	RS (cortex)	FS (cortex)
$\dot{V} = 10 \text{ mV/ms}$	-28.8 ± 4.3	-31.3 ± 2.8	-33.4 ± 1.1	-26.3 ± 6.0	-39.5 ± 3.3
$\dot{V} \text{ max}$	-25.6 ± 4.7	-27.6 ± 3.6	-31.5 ± 1.4	-19.3 ± 5.0	-30.5 ± 2.9
$\ddot{V} \text{ max}$	-33.4 ± 3.4	-35.7 ± 2.1	-41.8 ± 2.2	-32.3 ± 5.5	-48.5 ± 2.5
AP BP	-26.7 ± 4.0	-30.0 ± 2.4	-30.3 ± 1.1	-23.3 ± 5.3	-35.3 ± 2.8
Phase plot BP	-29.2 ± 4.1	-31.6 ± 2.7	-33.1 ± 1.2	-27.9 ± 5.6	-40.7 ± 3.0

The \ddot{V} method produces the lowest AP onset potential and the smallest RSD, whereas the AP BP produce the highest onset potential values and the highest RSD. Also, the results show that the \dot{V} method at 10 mV/ms produce AP onset potential values that are very similar to the values given by the PS BP method. These results indicate that \dot{V} method estimation of the onset potential reflect the kink at the best breaking point in the phase plot in very accurate way, even though the change in the criterion level could change the rapidity value significantly as shown in the results section. For example, for hippocampal PVBCs, shifting the criterion level from 10 to 40 mV/ms, lead to 1.1 mV change in the AP onset value while the phase slope increased from 10.6 to 48.6 ms⁻¹

¹. Therefore, although the \dot{V} method is not the best way to measure the AP rapidity, it provides the easiest way, with a good approximation, to measure the AP onset potential.

Outliers' detection methods

The cubic spline interpolation caused a huge variation in the phase slope values for hippocampal pyramidal neurons, as discussed in the results section (chapter 5). The high phase slope SD value was caused by 3 neurons, which labeled as D206, S104, and S313. Excluding these three neurons led to smaller variation of the phase slope values while it did not change the variation significantly for the other methods and AP parameters (Table B3). The phase slope RSD value was reduced 135.3% to 64.8%, which was higher than the RSD obtained with *pchip* interpolation method (n =17, RSD = 43.1%). Furthermore, taking a closer look at the phase slope values for each of the three neurons with high SD values reveal that the cause of such high variation is only several APs within some spike train. Therefore, we applied three outlier detection methods to exclude the outlier APs in each of the three neurons.

Table B3: Comparison of the AP properties after excluding the three neurons with high phase slope SD

	n	IFWd ² (ms)	IHWd ² (ms)	Phase slope (ms)	Error ratio	Amplitude (mV)	Width (ms)	Onset (mV)
Mean	14	4.5	7.6	43.7	6.0	66.7	1.6	-29.8
SD		0.5	1.1	28.3	2.8	5.1	0.4	3.6
RSD		11.1%	14.6%	64.8%	46.5%	7.7%	24.3%	-12.1%
Mean	17	4.3	7.2	47.8	6.1	67.5	1.6	-30.2
SD		0.5	1.1	64.6	2.7	5.3	0.4	3.5
RSD		11.4%	15.0%	135.3%	44.4%	7.9%	23.6%	-11.7%

MATLAB *isoutlier* function was used to detect the outliers phase slope values for the three neurons with high SD values (using spline interpolation). The *isoutlier* function detected the outlier based on five methods, which was applied to the phase slope values from the three neurons. The five methods exclude 20 APs at most, which represents less than 15% of the total APs as shown in Table B4. As expected, excluding the outlier APs have insignificant impact on the mean AP properties since all the variation between the values was small. For the \ddot{V} peak width methods and the error ratio method, excluding some APs did not change the mean value significantly while it had a small impact on the SD values (>25% change). On the other hand, the phase slope values changed significantly. By excluding the highest number of APs in each of the three neurons, the median method led to the lowest pooled mean and SD of the phase slope value, and hence the lowest variation. Whereas the mean method caused a substantial change in the pooled SD of the phase slope value (> 50% decrease) by excluding only 9 APs from all the three neurons (Table. B5). Nonetheless, even after applying the outlier test methods on the APs from the three hippocampal PCs, the phase slope RSD was still very high compared to the value obtained with the *pchip* interpolation method (RSD = 43.1%).

Table B4: Number of APs excluded by each outlier test method for the three hippocampal PCs

Label	N	median	mean	quartiles	grubbs	gesd
S104	145	20	4	15	15	15
S313	126	12	1	10	4	9
D206	103	13	4	9	9	9

Table B5: Pooled statistics after applying the outlier test methods for the three neurons with the highest phase slope SD.

Hippocampal PCs (n = 17)		IFWd ² (ms)	IHWd ² (ms)	Phase slope (ms)	Error ratio	Amplitude (mV)	Width (ms)	Onset (mV)
Original	Mean	4.3	7.2	47.8	6.1	67.5	1.6	-30.2
	SD	0.5	1.1	64.6	2.7	5.3	0.4	3.5
	RSD	11.4%	15.0%	135.3%	44.4%	7.9%	23.6%	-11.7%
Median	Mean	4.3	7.3	45.4	6.1	67.2	1.6	-30.0
	SD	0.5	1.1	27.9	2.7	5.2	0.4	3.5
	RSD	11.1%	14.7%	61.4%	44.2%	7.7%	23.5%	-11.6%
Mean	Mean	4.3	7.3	47.6	6.1	67.4	1.6	-30.1
	SD	0.5	1.1	35.6	2.7	5.3	0.4	3.5
	RSD	11.2%	14.8%	74.8%	44.2%	7.8%	23.5%	-11.7%
quartiles	Mean	4.3	7.3	45.9	6.1	67.2	1.6	-30.1
	SD	0.5	1.1	28.4	2.7	5.2	0.4	3.5
	RSD	11.1%	14.7%	61.9%	44.2%	7.7%	23.5%	-11.6%
grubbs	Mean	4.3	7.3	46.2	6.1	67.3	1.6	-30.1
	SD	0.5	1.1	29.0	2.7	5.2	0.4	3.5
	RSD	11.1%	14.7%	62.8%	44.2%	7.7%	23.5%	-11.6%
gesd	Mean	4.3	7.3	45.9	6.1	67.2	1.6	-30.1
	SD	0.5	1.1	28.4	2.7	5.2	0.4	3.5
	RSD	11.1%	14.7%	62.0%	44.2%	7.7%	23.5%	-11.6%

Relationship between the \ddot{V} peak width and the integrated area

The relationship between the rapidity, using the \ddot{V} peak width methods, and the integrated area under the rising phase of \dot{V} and \ddot{V} were analyzed. Assuming a constant membrane capacitance, the integrated area under the rising phase of \dot{V} represent the total inward charge, whereas the integrated area under the rising phase of \ddot{V} represent the total inward current. Also, we looked at the relationship between the IFWd² and IHWd² verses the integrated \dot{V} area up to the peak. The value for the membrane capacitance for each cell types were taken as the mean value reported in the NeuroElectro project website. Therefore, the mean membrane capacitance was set to 90 pF for CA1 hippocampal PCs, 162 pF for CA1 hippocampal basket neurons, 153 pF for CA1 hippocampal OLMs, and 174 pF for cortical pyramidal neurons. For the FS cortical neurons, the

specific cell type was not reported and was identified only by its firing pattern [78]. Thus, we choose a 60 pF membrane capacitance since it is within the range of the reported values for deep cortical interneurons (44 pF), cortical basket cells (59 pF), and uncharacterized cortical neurons (61 pF).

The normalized integrated area of \dot{V} and \ddot{V} were not significantly different between the hippocampal deep and superficial PCs (Table B6). The only significant difference between deep and superficial PCs were between the area under the rising phase of \ddot{V} and the area of \dot{V} up to the peak value. However, it should be noted that one superficial PC is responsible for the significant difference. More specifically, the late APs in the spike train of the neuron labelled S147. Once this neuron was eliminated, there was no significant difference in the area under the rising phase of \ddot{V} between the hippocampal deep and superficial PCs ($t = 1.61$, $p = 0.13$), but the difference is still significant in the area of \dot{V} up to the peak value ($t = 3.24$, $p = 0.006$) even though the clusters seems to lay in the same region as shown in Figure B2.

Table B6: Relationship between the \ddot{V} peak width and the integrated area in hippocampal pyramidal neurons.

CA1 hipp.	Deep PCs (n=9)		Superficial PCs (n=8)		t	p
	Mean \pm SD	RSD	Mean \pm SD	RSD		
IFWd ²	4.5 \pm 0.5	11.2%	4.1 \pm 0.5	11.6%	1.635	0.123
IFWd ²	7.3 \pm 1.2	15.8%	7.1 \pm 1.0	13.8%	0.370	0.716
AP amplitude	69.4 \pm 4.9	7.0%	65.1 \pm 5.8	9.0%	1.658	0.118
AP width	1.5 \pm 0.3	20.6%	1.7 \pm 0.4	26.2%	1.175	0.25
onset potential	-31.3 \pm 2.8	-8.8%	-28.8 \pm 4.3	-14.9%	1.437	0.171
$C_m \int \frac{\ddot{V}_{rise}}{\ddot{V}_{max}} dt$	20.9 \pm 2.2	10.4%	23.0 \pm 2.8	12.3%	1.72	0.107
$C_m \int \frac{\dot{V}}{\dot{V}_{max}} dt$	-0.8 \pm 0.6	-79.2%	-1.3 \pm 1.7	-128.5%	0.89	0.389
$C_m \int \frac{\dot{V}_{peak}}{\dot{V}_{max}} dt$	12.4 \pm 1.9	15.1%	15.0 \pm 5.0	33.5%	1.45	0.168

$C_m \int \frac{\dot{V}_{rise}}{\dot{V}_{max}} dt$	33.0 ± 3.0	9.0%	40.9 ± 13.2	32.2%	1.76	0.099
$C_m \int \frac{\dot{V}}{\dot{V}_{max}} dt$	2.1 ± 2.8	131.0%	4.9 ± 12.1	245.6%	0.68	0.51
$C_m \int \ddot{V}_{rise} dt$	17720 ± 2523	14.2%	14497 ± 2655	18.3%	2.565	0.0215
$C_m \int \ddot{V} dt$	-522.0 ± 297.9	-57.1%	-484.1 ± 275.9	-57.0%	0.27	0.79
$C_m \int \dot{V}_{peak} dt$	2420.1 ± 63.4	2.6%	2228.6 ± 127.5	5.7%	3.997	0.0012
$C_m \int \dot{V}_{rise} dt$	6490.7 ± 392.0	6.0%	6077.0 ± 482.2	7.9%	1.95	0.07
$C_m \int \dot{V} dt$	317.8 ± 412.2	129.7%	274.3 ± 431.6	157.3%	0.212	0.83

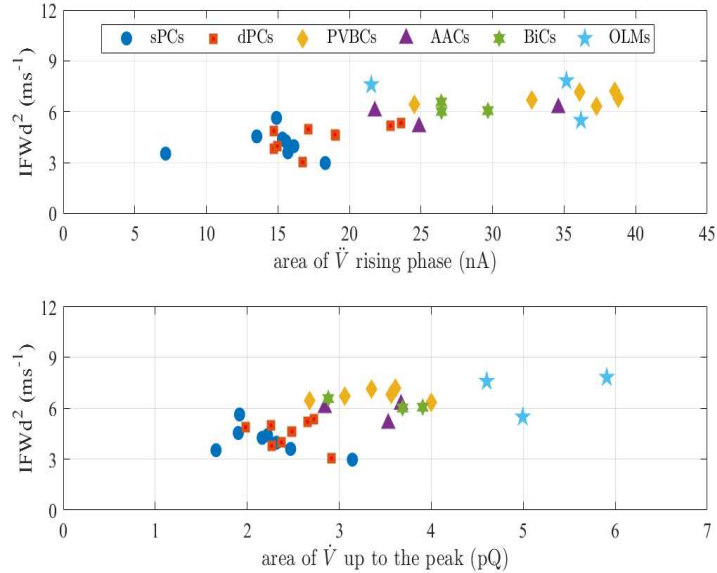


Figure B2: Comparison between IFWd² the integrated area of the rising phase of \dot{V} for hippocampal neurons (top) and the integrated area of the \dot{V} up to the peak value (bottom).

Hippocampal Interneurons

The hippocampal database contain recording from 6 inhibitory interneurons. However, in the main manuscript, we only include the neuron type with a sample size of 3 or more. Thus, here, we present the results from all the inhibitory interneuron types including the interneuron types with a sample size less than 3. These interneurons can be classified based on their firing patterns

as Fast-spiking (FS), Regular-spiking (RS), and Late-spiking (LS). The details of each interneuron type are shown in Table B7. Table B8 and B9 shows the pooled mean and pooled SD values, while Table B10-B13 shows the p-value obtained from the two tailed t score for the IFWd², IHWd², phase slope, and AP width.

Table B7: recording details for each hippocampal interneuron.

Interneuron type	n	Firing patterns	Number of APs
Axo-axonic (AACs)	3	FS	64 - 159
Bistratified (BiCs)	3	FS	31 - 41
PV+ Basket (PVBCs)	6	FS	80 - 199
Oriens-lacunosummoleculare (OLM)	3	RS	316 - 463
Schaffer Collateral Assoc. (SCAs)	2	RS	18 - 23
CCK+ Basket (CCKBCs)	1	RS	12
Ivy (IvCs)	2	LS	352 - 2149
Neurogliaform (NGFCs)	2	LS	99 - 250

Table B8: electrophysiological properties mean and standard deviations values.

Mean values	IFWd² (ms⁻¹)	IHWd² (ms⁻¹)	Phase slope (ms⁻¹)	Error ratio	amplitude (mV)	width (ms)	Onset (mV)
Cortical PC	2.1 ± 0.3	4.0 ± 0.5	6.9 ± 1.4	7.9 ± 6.4	61.7 ± 8.6	2.0 ± 0.3	-26.3 ± 6
Cortical FS	2.7 ± 0.2	4.6 ± 0.3	8.1 ± 1.1	11.2 ± 7.5	58.0 ± 5.2	0.8 ± 0.1	-39.5 ± 3.3
Hipp. PC	4.3 ± 0.5	7.2 ± 1.1	47.8 ± 64	6.1 ± 2.7	65.8 ± 5	1.6 ± 0.4	-30.2 ± 3.5

NGFCs	4.0 ± 0.7	10.3 ± 1.3	75.3 ± 140	---	36.1 ±4	1.2 ± 0.2	-31.4 ± 2.8
IvCs	5.8 ± 0.5	10.7 ± 1.0	134.9 ± 6984	---	46.2± 3.9	0.8 ± 0.1	-29.6 ± 5
AACs	5.7 ± 0.3	10.0 ± 0.7	17.8 ± 5.2	1.4 ± 0.9	43.2 ± 1.5	0.5 ± 0.0	-30.1 ± 1.1
BiC	6.2 ± 0.3	10.9 ± 0.7	7.5 ± 3.3	0.4 ± 0.3	44.0 ± 1.7	0.4 ± 0.0	-29.8 ± 0.8
PVBC	6.9 ± 0.4	12.1 ± 1.0	10.4 ± 4.5	0.7 ± 2.4	48.9 ± 2.1	0.3 ± 0.0	-33.4 ± 1.1
OLM	6.8 ± 1.2	12.2 ± 3.2	31.0 ± 20	4.4	65.5 ± 5.6	0.8 ± 0.1	-42.3 ± 2.1
CCKBCs	4.8 ± 0.4	10.9 ± 1.1	95.8 ± 670	----	63.2 ± 1.1	1.3 ± 0.1	-37.7 ± 0.4
SCAs	4.9 ± 0.3	10.3 ± 1.0	-1300.1 ± 8708	----	58.2 ± 0.6	1.2 ± 0.1	-33.7 ± 9.8

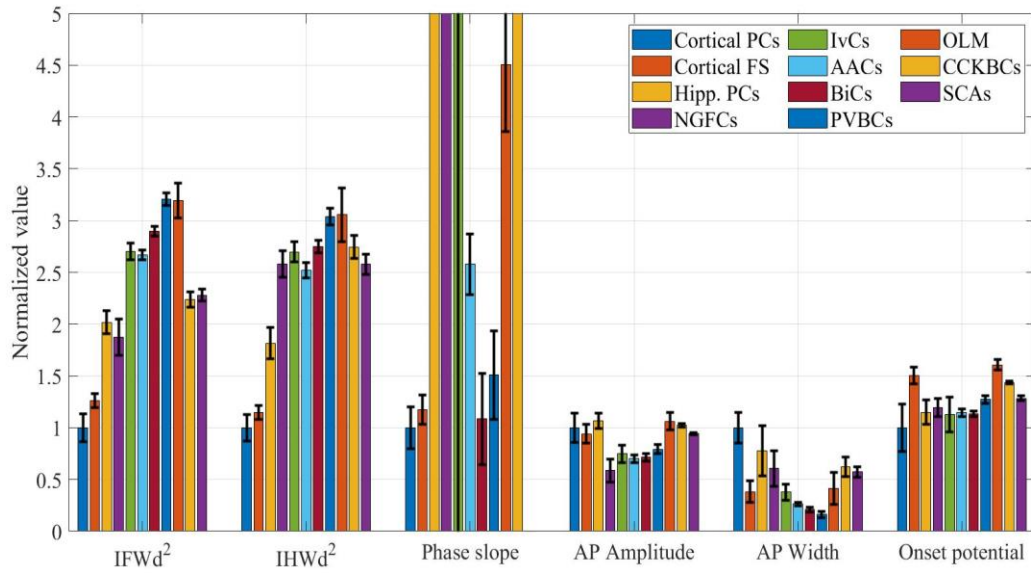


Figure B3: Comparison of the electrophysiological properties. The y-axis is the values normalized to the values obtained from the cortical pyramidal neurons, and the error bar represents the RSD for each neuron population. Note the data from neurons with $n < 3$ was excluded since the size number was insufficient

Table B9: P-values from t test score for $IFWd^2$

$IFWd^2$	cPCs	cFS	hPCs	AACs	BiCs	PVBCs	OLMs	NGFCs	IvCs	SCAs
cPCs	0.00	0.00	0.00	0.00	0.00	0.00	0.00	0.00	0.00	0.00
cFS	0.00	0.00	0.00	0.00	0.00	0.00	0.00	0.00	0.00	0.00
hPCs	0.00	0.00	0.00	0.00	0.00	0.00	0.00	0.42	0.00	0.14
AACs	0.00	0.00	0.00	0.00	0.11	0.00	0.18	0.03	0.84	0.04
BiCs	0.00	0.00	0.00	0.11	0.00	0.05	0.41	0.02	0.30	0.02
PVBCs	0.00	0.00	0.00	0.00	0.05	0.00	0.95	0.00	0.02	0.00
OLMs	0.00	0.00	0.00	0.18	0.41	0.95	0.00	0.06	0.32	0.11
NGFCs	0.00	0.00	0.42	0.03	0.02	0.00	0.06	0.00	0.10	0.24
IvCs	0.00	0.00	0.00	0.84	0.30	0.02	0.32	0.10	0.00	0.14
SCAs	0.00	0.00	0.14	0.04	0.02	0.00	0.11	0.24	0.14	0.00

Table B10: P-values from t test score for IHWd²

IHWd ²	cPCs	cFS	hPCs	AACs	BiCs	PVBCs	OLMs	NGFCs	IvCs	SCAs
cPCs	0.00	0.01	0.00	0.00	0.00	0.00	0.00	0.00	0.00	0.00
cFS	0.01	0.00	0.00	0.00	0.00	0.00	0.00	0.00	0.00	0.00
hPCs	0.00	0.00	0.00	0.00	0.00	0.00	0.00	0.00	0.00	0.00
AACs	0.00	0.00	0.00	0.00	0.19	0.01	0.32	0.79	0.42	0.78
BiCs	0.00	0.00	0.00	0.19	0.00	0.11	0.55	0.50	0.81	0.42
PVBCs	0.00	0.00	0.00	0.01	0.11	0.00	0.96	0.07	0.14	0.06
OLMs	0.00	0.00	0.00	0.32	0.55	0.96	0.00	0.50	0.60	0.49
NGFCs	0.00	0.00	0.00	0.79	0.50	0.07	0.50	0.00	0.73	0.99
IvCs	0.00	0.00	0.00	0.42	0.81	0.14	0.60	0.73	0.00	0.68
SCAs	0.00	0.00	0.00	0.78	0.42	0.06	0.49	0.99	0.68	0.00

Table B11: P-values from t test score for phase slope

Phase slope	cPCs	cFS	hPCs	AACs	BiCs	PVBCs	OLMs	NGFCs	IvCs	SCAs
cPCs	0.00	0.04	0.00	0.00	0.56	0.00	0.00	0.00	0.90	0.30
cFS	0.04	0.00	0.12	0.00	0.65	0.21	0.01	0.16	0.95	0.64
hPCs	0.00	0.12	0.00	0.44	0.30	0.18	0.67	0.61	0.95	0.41
AACs	0.00	0.00	0.44	0.00	0.04	0.06	0.33	0.49	0.98	0.79
BiCs	0.56	0.65	0.30	0.04	0.00	0.35	0.11	0.43	0.97	0.79
PVBCs	0.00	0.21	0.18	0.06	0.35	0.00	0.04	0.21	0.96	0.67
OLMs	0.00	0.01	0.67	0.33	0.11	0.04	0.00	0.60	0.98	0.79
NGFCs	0.00	0.16	0.61	0.49	0.43	0.21	0.60	0.00	0.99	0.84
IvCs	0.90	0.95	0.95	0.98	0.97	0.96	0.98	0.99	0.00	0.87
SCAs	0.30	0.64	0.41	0.79	0.79	0.67	0.79	0.84	0.87	0.00

Table B12: P-values from t test score for AP width

AP width	cPCs	cFS	hPCs	AACs	BiCs	PVBCs	OLMs	NGFCs	IvCs	SCAs
cPCs	0.00	0.00	0.00	0.00	0.00	0.00	0.00	0.00	0.00	0.00
cFS	0.00	0.00	0.00	0.00	0.00	0.00	0.39	0.00	0.88	0.00
hPCs	0.00	0.00	0.00	0.00	0.00	0.00	0.00	0.24	0.01	0.16
AACs	0.00	0.00	0.00	0.00	0.00	0.00	0.02	0.01	0.01	0.00
BiCs	0.00	0.00	0.00	0.00	0.00	0.00	0.01	0.01	0.00	0.00
PVBCs	0.00	0.00	0.00	0.00	0.00	0.00	0.00	0.00	0.00	0.00
OLMs	0.00	0.39	0.00	0.02	0.01	0.00	0.00	0.08	0.54	0.05
NGFCs	0.00	0.00	0.24	0.01	0.01	0.00	0.08	0.00	0.10	0.69
IvCs	0.00	0.88	0.01	0.01	0.00	0.00	0.54	0.10	0.00	0.02
SCAs	0.00	0.00	0.16	0.00	0.00	0.00	0.05	0.69	0.02	0.00

Differences in onset rapidity between CA1 hippocampal interneurons

In the hippocampus, GABAergic interneurons account for 7-11% of the total neuron population [140]. The interneurons, although they are a minority in the hippocampus, have

a major role in determining almost all aspects of neuronal circuits and regulation [105]. Thus, to explore the role of AP onset rapidity in this diversity among interneurons as well as their principle excitatory neuron counterparts, the pyramidal neurons, the rapidity of 3 hippocampal FS interneurons used to construct the CA1 neural network model [141] were analyzed.

First, since the available sample size for BiCs and AACs are small ($n = 3$), the Kruskal-Wallis test was performed to see if the available data is sufficient to do a comparison between the hippocampal FS interneurons. The results from the Kruskal-Wallis test showed that only AP properties are significantly different between the 3 hippocampal FS interneurons are the AP width ($H = 6.7, p = 0.035$) and the AP rapidity calculated using the IFWd² method ($H = 6.9, p = 0.032$). However, it must be noted that with such a small size for the BiCs and AACs, the combination of sample sizes with neuron type with higher sample size such as hippocampal pyramidal cell ($n=17$) does not allow to find a critical value for this Kruskal-Wallis test. Thus, a higher sample size is needed before drawing any conclusions about the differences between the BiCs and AACs and their counterpart, the pyramidal neurons.

The interneuron analysis reveals that IFWd² and IHWd² methods are not only the best methods to distinguish the onset rapidity of cortical and hippocampal pyramidal neurons, but also excel at distinguishing various hippocampal FS interneurons compared to the other rapidity quantification methods as evidenced by higher t-scores. More specifically, the IFWd² method shows the highest t-score between all FS interneurons. The t-score for the IFWd² method is higher than 3 between the FS interneurons except between BiCs and AACs ($t = 2.06, P = 0.108$).

Appendix C: supporting information for spike train patterns (intend to publish)

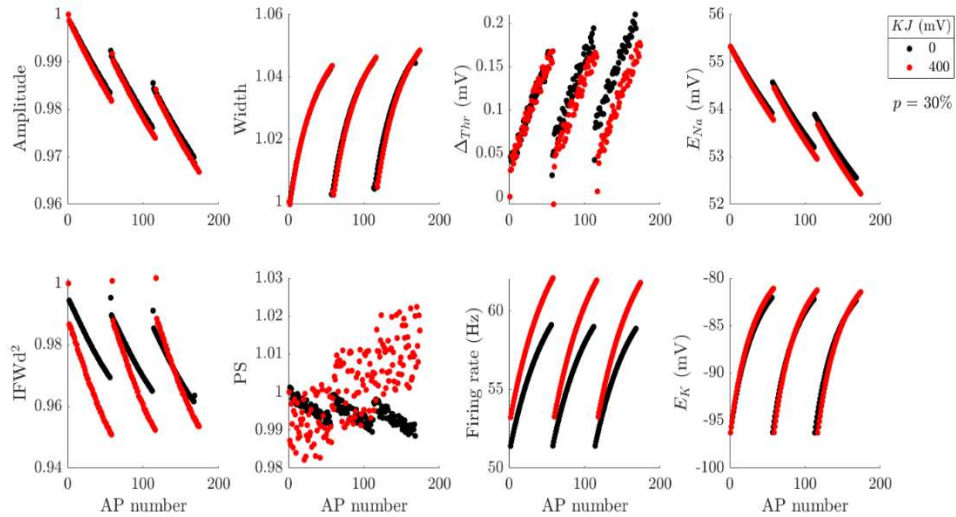


Figure C1: Impact of different coupling strength on AP parameters with three current steps (1s step duration and inter sweep interval of 5s) with no cooperative channels (black) and 30% of Na^+ channels activated cooperatively (red).

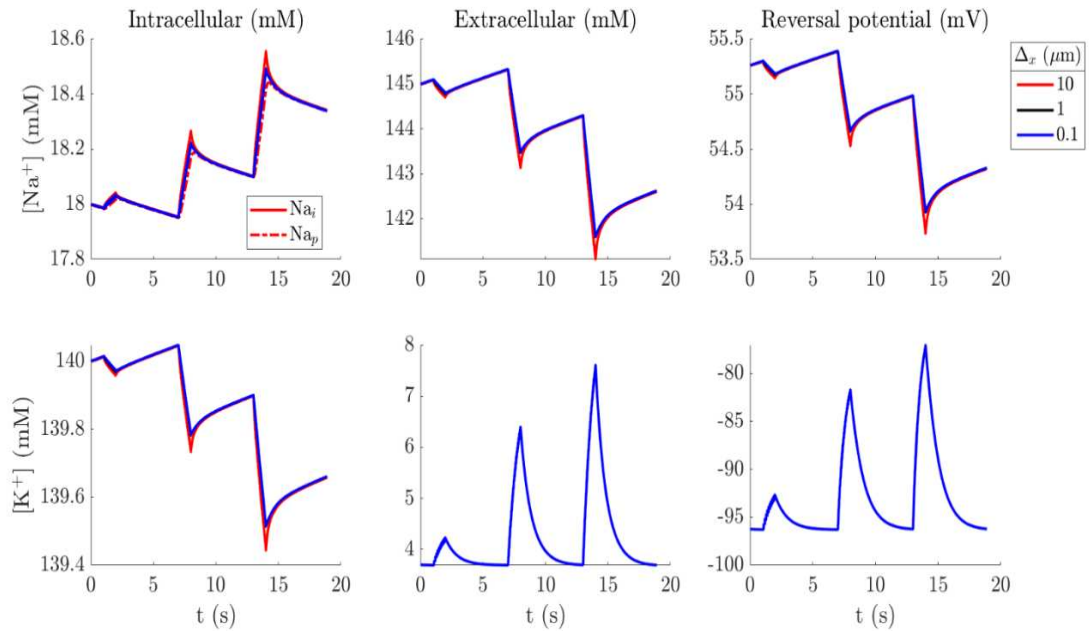


Figure C2: Impact of varying the distance between the pump and Na^+ channels on ion concentrations ($D_{Na} = 0.3$ $\mu m/ms$).

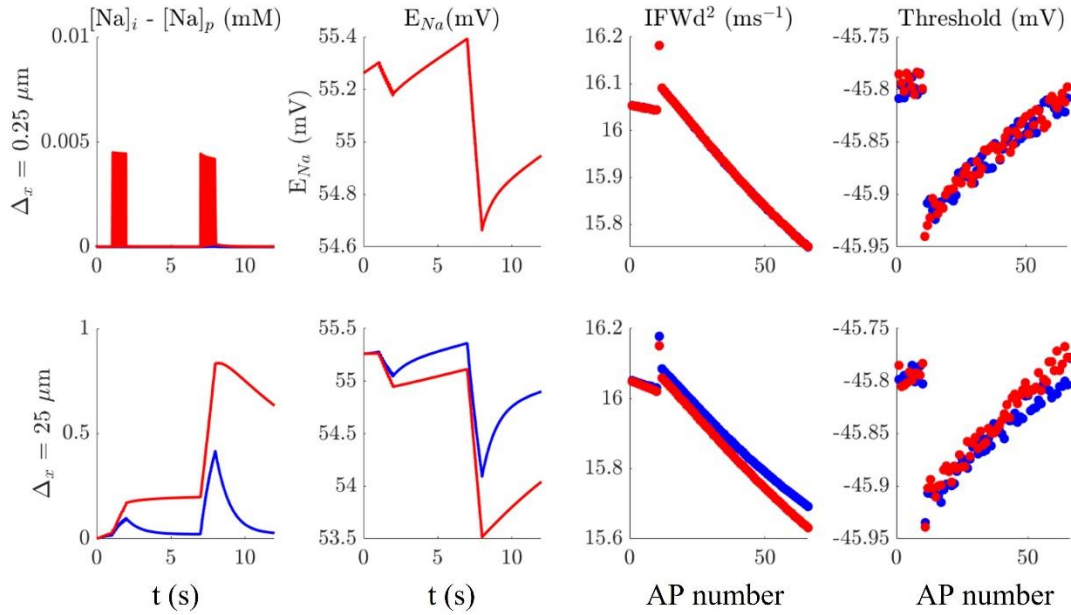


Figure C3: Impact of varying the distance between the pump and Na^+ channels and Na^+ diffusion constant on AP initiation attributes, Na^+ reversal potential, and the difference between intracellular Na^+ concentration. The results obtained with all Na^+ channels exhibit independent gating ($\text{KJ}=0$). The blue symbols represent the value when $D_{\text{Na}}=0.3 \mu\text{m}^2/\text{ms}$. The red symbols represent the value when $D_{\text{Na}}=0.03 \mu\text{m}^2/\text{ms}$.

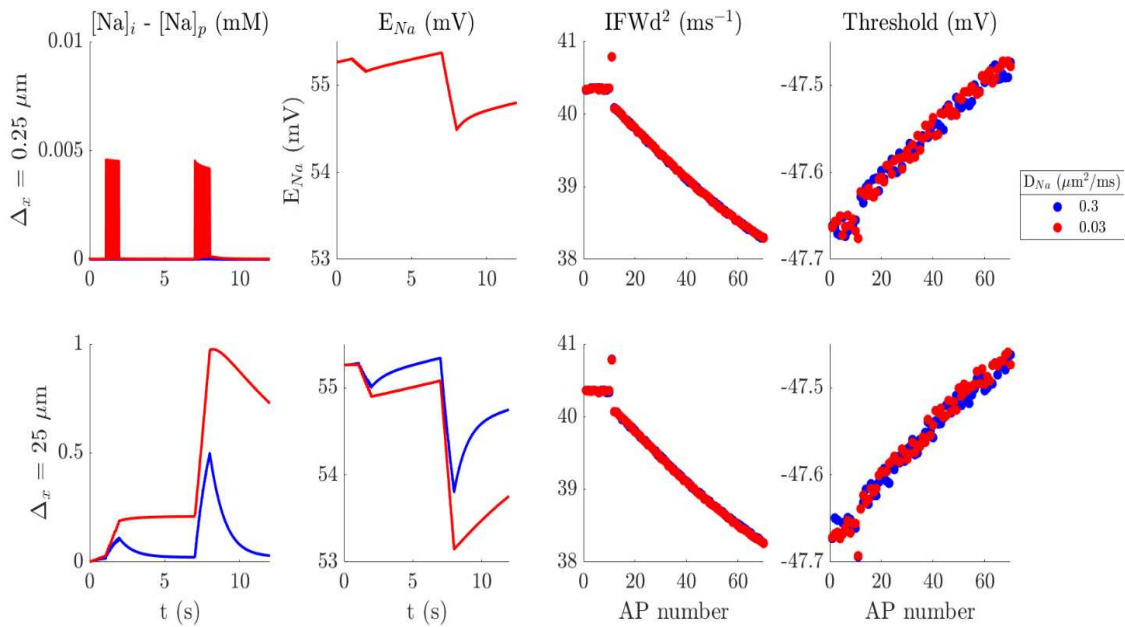


Figure C4: Impact of varying the distance between the pump and Na^+ channels and Na^+ diffusion constant on AP initiation attributes, Na^+ reversal potential, and the difference between intracellular Na^+ concentration. The results obtained in the presence of 50% cooperative Na^+ channels ($\text{KJ}=400 \text{ mV}$).

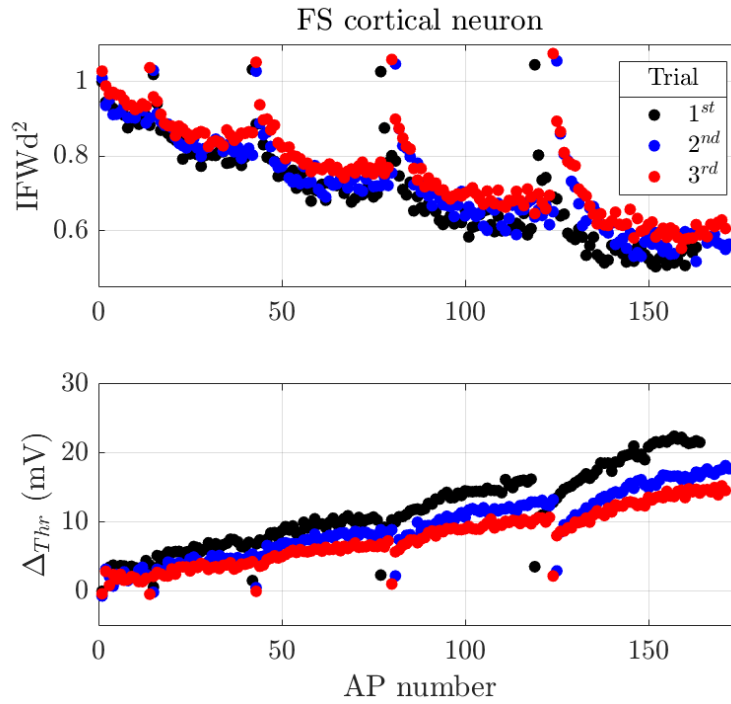


Figure C5: Normalized AP rapidity (top) and threshold potential difference from the value of the first AP. The step-and-hold stimulation protocol included 5 steps of 0.5s long depolarization pulses with an inter-sweep interval of 6.5 s. The stimulus train was repeated 3 times with a 20 s interval. The recordings obtained from the GigaScience database [78].

Appendix D: Comparison and analysis of the models used to replicate spike train patterns

Cooperative gating increases AP onset rapidity

Cooperative gating was proposed as a mechanism responsible for the fast AP phase slope rapidity observed in central mammalian neurons [2], [5], [6]. Here we used the same mechanism for cooperativity, but first two points need to be addressed. First, AP rapidity increases with increasing cooperativity level. Huang *et al* showed that the highest rapidity occurs with a small fraction of strongly coupled channels [5]. However, changing the criterion level, where rapidity is measured, to a higher value led to higher phase slope rapidity. As shown in Figure D1, the maximum rapidity occurred at a higher cooperativity level when the criterion level was shifted. Also, the maximum rapidity value increases with higher criterion level. Such a significant difference is due to the shift in criterion levels position between the baseline and the vertical rise in the phase space plot, which had been discussed previously in the literature [7], [28], [63]. Second, including cooperativity gating in the Wang-Buzsaki model (cWB) can produce biphasic APs, but it can lead to unrealistic features. The biphasic nature of an AP can be seen by the two humps in the phase-plot or double-peak \ddot{V} . However, the two \ddot{V} peaks produced by the cWB model have significantly different amplitudes, where the 1st peak's amplitude is five times higher than the 2nd peak (Figure D2). On the other hand, double-peak's \ddot{V}_m in electrophysiological recordings usually have a similar amplitude [9], [142], [143]. To address the difference between the model and experimental data in terms of \ddot{V}_m shape, we added cooperative gating on several HH-type models. A comparison of the resulting \ddot{V}_m shapes is shown in Figure 2D using the cWB model, the modified Cressman *et al* model with cooperative gating, and the combined model as described in the method using Traub and Miles' (TM) version of HH model. The huge difference between the position and amplitude of the double \ddot{V} peaks was not present using a modified version TM

HH model, producing \ddot{V}_m shapes that are comparable to experimental data as shown in Figure D3. It should be noted that the double peak can significantly influence the IFWd² rapidity. The IFWd² might overestimate the AP rapidity when the two peaks have significantly different amplitude or underestimate the AP rapidity with comparable \ddot{V}_m peaks. Thus, we used the phase slope method to quantify AP rapidity when comparing the different HH-type methods.

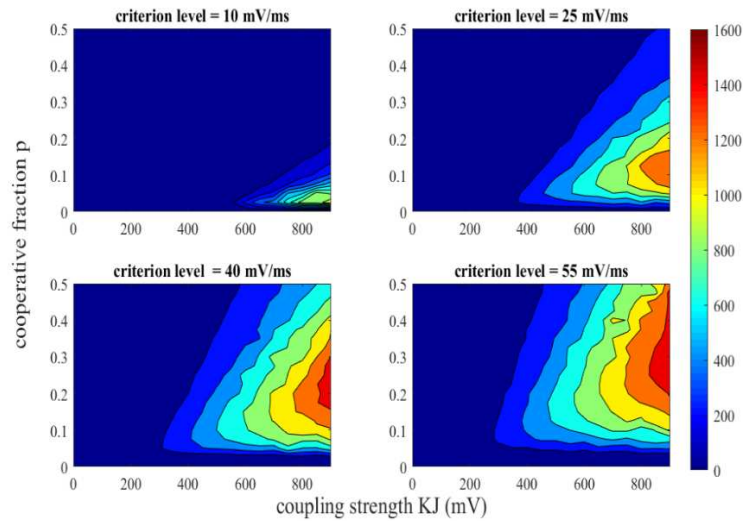


Figure D1: Replication of figure 4A from Huang et al (2012) paper at different criterion level obtained using their published code. The critical values of coupling strength and fraction where the maximum rapidity occurred increase as the criterion level increase. Also, the phase slope values increase with higher criterion level. The maximum values are 970, 1356, 1517, and 1574 ms⁻¹ from the smallest to the highest criterion level.

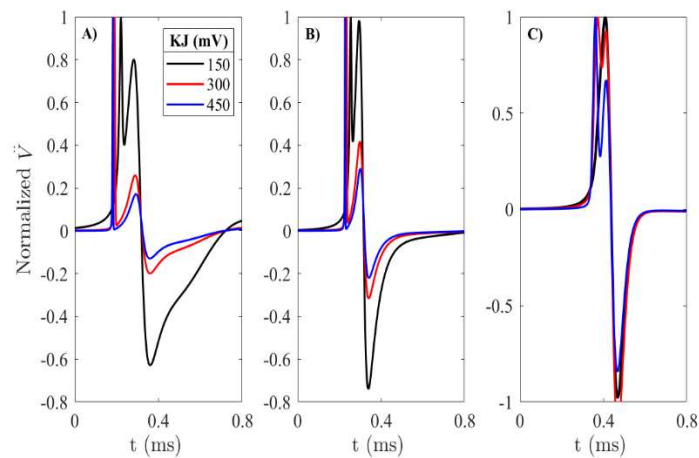


Figure D2: Comparison on the impact of coupling strength on \dot{V} traces using three different models ($p = 10\%$). A) \dot{V} traces using Huang et al (2012) model [5]. B) \dot{V} traces using a modified Cressman et al (2009) [26] model to include cooperative gating. C) \dot{V} traces using the combined model, which is based on Pospischil et al model [82].

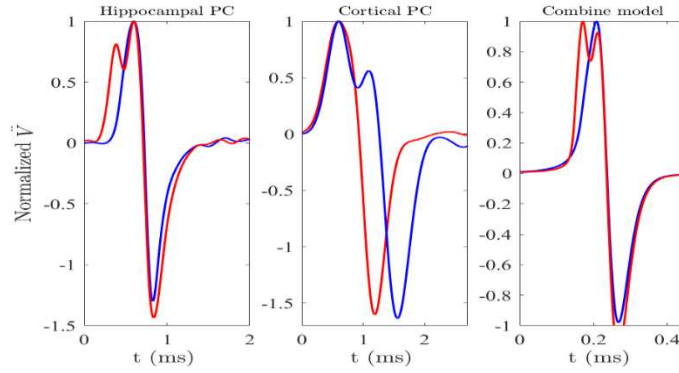


Figure D3: Comparison of \dot{V} traces from intracellular recordings of cortical and hippocampal pyramidal neurons and the combined model. The recording from cortical and hippocampal pyramidal neurons was obtained from GigaScience and CRCNS databases, and the experimental procedure are found in [78], [87]. The \dot{V} traces from the combined model were obtained with $p=10\%$ and $KJ = 150$ (blue) and 300 mV (red).

The rising phase of central mammalian neuron APs can exhibit monotonic or non-monotonic voltage increase [9]. The double-component rising phase was suggested as a characteristic for APs backpropagation from the spikes initiation site at the axon initial segment to the soma [3]. Also, the same phenomena were reproduced with a small fraction of strongly cooperative Na^+ channels, where the rising phase of AP becomes monotonic with a high fraction of cooperative Na^+ channels [5]. However, a higher percentage of cooperative channels, such as $p = 80\%$, produces a small peak near the minimum value of \dot{V} (Figure D4). This can be attributed to the base model, the Wang-Buzsaki (WB) model, which describes a FS PV+ inhibitory basket cell. On the other hand, following TM description for FS neurons or RS pyramidal neurons with a modification to include slow non-inactivating K^+ current did not produce the small peak near the minimum value of \dot{V} (Figure D4). In addition, the afterhyperpolarization (AHP) in FS neurons is more pronounced than the AHP in RS neurons. However, the TM model for a pyramidal cell produced more hyperpolarization than the WB PV+ inhibitory basket cell model, which oppose experimental data [144]. Therefore, the TM version of the HH model was chosen as the base model to add dynamic reversal potential and cooperative gating (The model used in chapter 5).

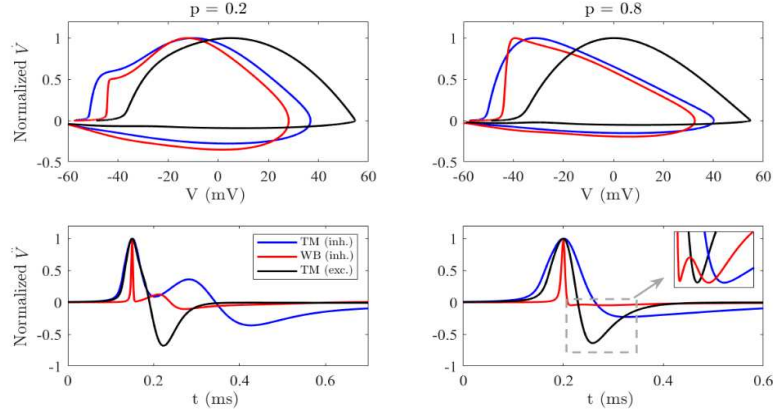


Figure D4: AP dynamics with strong coupling strength ($KJ = 320$ mV). Top: shows the normalized phase plots with a small and a large fraction of cooperative channels. Bottom shows the normalized \dot{V} trace for the same APs on top. Inset box show the negative portion of the \dot{V} trace. The red traces represent a FS hippocampal neuron, which was reproduced using Huang et al (2012) published model without any modification to the main code [145]. Blue and black traces represent a RS excitatory (PC) neuron and RS inhibitory neuron as described in [82], where they modified Traub and Miles (1991) model to include a slow potassium current as described in Yamada et al. (1989) [82], [146], [147].

Table D1: Comparison between the rate functions used in Figure D4.

Model	Wang-Buzsaki (1996) (As used in Huang <i>et al</i>)	Gutkin <i>et al</i> (2001) (As used in Cressman <i>et al</i>)	Traub and Miles (1991) (Used in the combined model)
α_m	$\frac{0.1(V + 35)}{1 - \exp(-0.1(V + 35))}$	$\frac{0.1(V + 30)}{1 - \exp(-0.1(V + 30))}$	$\frac{0.32(V - V_T - 13)}{1 - \exp\left(-\frac{(V - V_T - 13)}{4}\right)}$
β_m	$4 \exp\left(-\frac{V + 60}{18}\right)$	$4 \exp\left(-\frac{(V + 55)}{18}\right)$	$\frac{0.28(V - V_T - 40)}{\exp\left(\frac{V - V_T - 40}{5}\right) - 1}$
α_h	$0.35 \exp(-0.05(V + 58))$	$0.21 \exp(-0.05(V + 44))$	$0.128 \exp\left(-\frac{V - V_T - 17}{18}\right)$
β_h	$\frac{5}{1 + \exp(-0.1(V + 28))}$	$\frac{3}{1 + \exp(-0.1(V + 4))}$	$\frac{4}{\exp\left(-\frac{V - V_T - 40}{18}\right) + 1}$
α_n	$\frac{0.05(V + 34)}{1 - \exp(-0.1(V + 34))}$	$\frac{-0.03(V + 34)}{\exp(-0.1(V + 34)) - 1}$	$\frac{0.032(V - V_T - 15)}{1 - \exp\left(-\frac{V - V_T - 15}{4}\right)}$
β_n	$0.625 \exp\left(-\frac{V + 44}{80}\right)$	$0.375 \exp\left(-\frac{V + 44}{80}\right)$	$0.5 \exp\left(-\frac{V - V_T - 10}{40}\right)$

Table D2: Models parameters used in the combined model for the four cell type models in the published code.

Cell type Parameters	RS		FS	
	Excitatory (Somatosensory)	Inhibitory (Somatosensory)	Inhibitory (Visual)	Inhibitory (Somatosensory)
E_{Leak} (mV)	-70.3	-65	-70	-70.4
V_T (mV)	-56.2	-67.9	-63	-57.9
g_{Leak} (mS/cm ²)	0.0205	0.0133	0.15	0.038
g_{Na} (mS/cm ²)	56	10	50	58
g_{Kd} (mS/cm ²)	6	2.1	10	3.9
g_M (mS/cm ²)	0.075	0.098	-	0.079
τ_M (sec)	0.608	0.934	-	502
$L = d$ (μm)	61.4	61.8	67	56.9

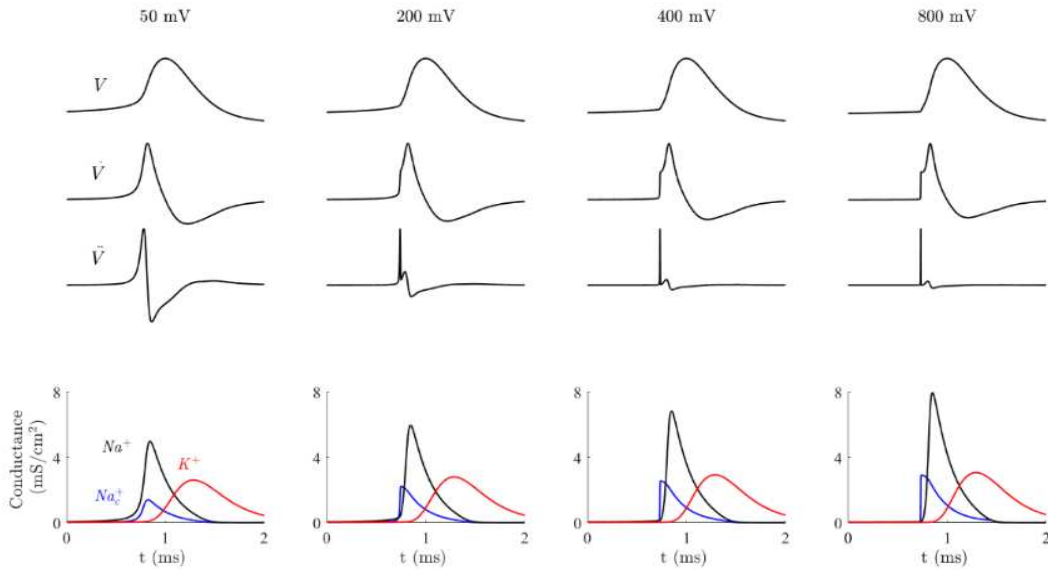


Figure D5: Different AP waveforms due to change in coupling strength (KJ), with 20% of Na⁺ channels activated cooperatively. The normalized membrane potential is shown with their 1st and 2nd time-derivative. The bottom plots show the conductance of independent Na⁺ channels (black), cooperative Na⁺ channels (blue), and K⁺ channels (red) during the same AP on top.

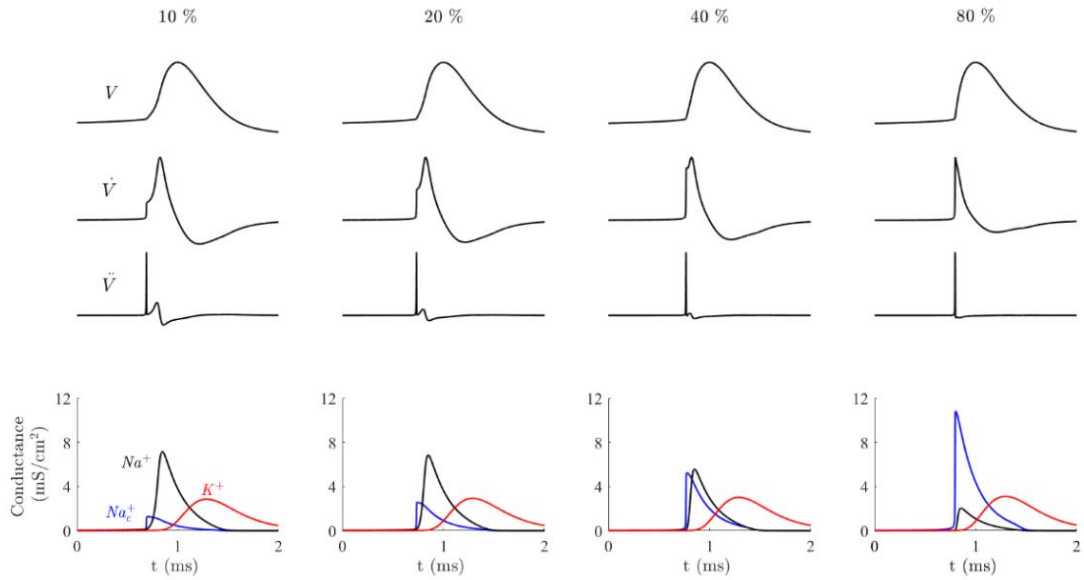


Figure D6: Different AP waveforms due to change in the fraction of cooperative Na⁺ channels with strong coupling strength ($KJ = 400$ mV). The normalized membrane potential is shown with their 1st and 2nd time-derivative. The bottom plots show the conductance of independent Na⁺ channels (black), cooperative Na⁺ channels (blue), and K⁺ channels (red) during the same AP on top.

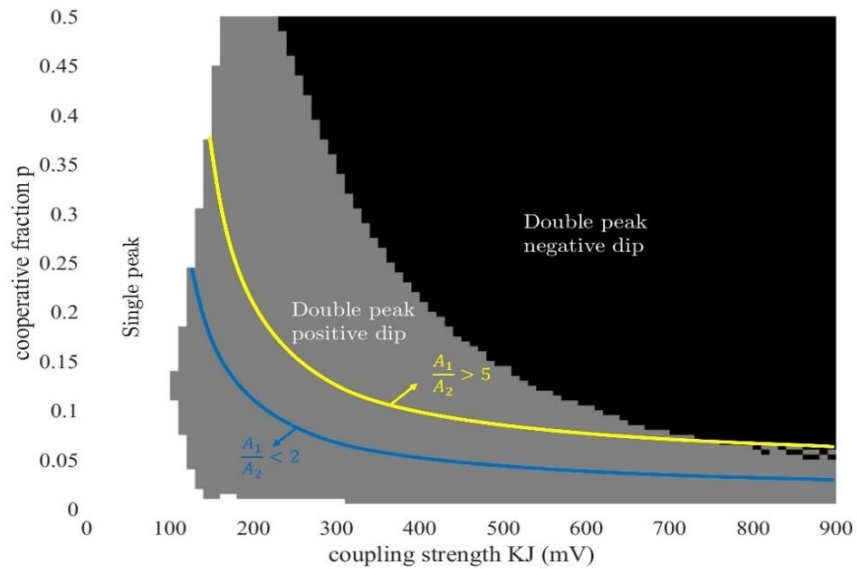


Figure D7: Limit of cooperativity to produce single \dot{V}_m peak (white area), double \dot{V} peak with positive minimum value (dip) between them (grey area), and double \dot{V} peak with negative dip (black area) using Huang *et al* code [145]. The curved line indicates where the ratio of \dot{V}_m peaks (A_1/A_2) is below 2 (blue) and above 5 (yellow).

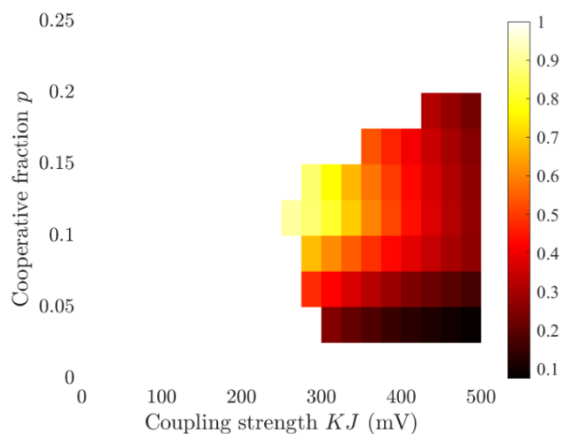


Figure D8: ratio of the minimum value between \tilde{V} two peaks to the maximum value. Note that double-peak \tilde{V} occur at small percentage with moderate to high coupling strength. Otherwise, the value in white indicates a single \tilde{V} peak. $I=0.65$ which produce a single AP. The model is based on Trub and Milles description of a RS pyramidal neuron [82].

Ion concentration impact with weak stimulus

Including dynamical reversal potential causes a slight change to AP parameters in response to weak stimulation. As shown in Table D4, some AP parameters shift slightly with dynamical reversal potential instead of the steady-state value. Thus, choosing steady-state reversal potentials can be justified since the differences is trivial, especially for a short-time scale. However, the difference is more apparent when looking at the AP parameters change in a spike train than the average values, especially after multiple spike trains. With dynamical reversal potential, the AP parameters continuously change during stimulation instead of the same value as the classical model. As shown in Figure D9, most AP parameters continuously change during the spike train and from one spike train to another. For example, the AP amplitude decreased by 0.3 mV and the width increased by around 15 μ s between the first and last AP in each spike train. These trends were absent when using steady-state reversal potential.

Furthermore, to identify how each ion concentration influences AP parameters, the reversal potential of each voltage-gated channel was set to its steady-state value while the other channel has a dynamical reversal potential. As expected, K^+ mainly control the AP width and firing rate,

while Na^+ influence AP amplitude and rapidity. The threshold potential was almost the same regardless of the reversal potential condition with weak stimulation. Increasing the current pulse magnitude causes a greater change in reversal potential, leading to higher threshold potential during the pulse. Nonetheless, even though these changes are small with weak stimulus, having dynamical reversal potential produces spike train patterns similar to electrophysiological recordings. The magnitude of change in AP parameters is influenced by the size of the change in reversal potential and the duration between the stimuli.

Table D4: Comparison on the effect of dynamical reversal potential on AP parameters of FS neuron model

Current pulse	Fixed reversal potential				Dynamical reversal potential			
	1 st	2 nd	3 rd	Average	1 st	2 nd	3 rd	Average
Amplitude (mV)	97.8	97.8	97.8	97.8	97.8	98.1	98.4	98.1
Width (ms)	0.8	0.8	0.8	0.8	0.8	0.8	0.8	0.8
Threshold (mV)	-45.8	-45.8	-45.8	-45.8	-45.8	-45.8	-45.8	-45.8
IFWd ² (ms ⁻¹)	16.0	16.0	16.0	16.0	16.0	16.1	16.1	16.1
PS (ms ⁻¹)	6.3	6.3	6.3	6.3	6.3	6.3	6.3	6.3
Firing rate (Hz)	5.3	5.3	5.3	5.3	5.4	5.5	5.6	5.5

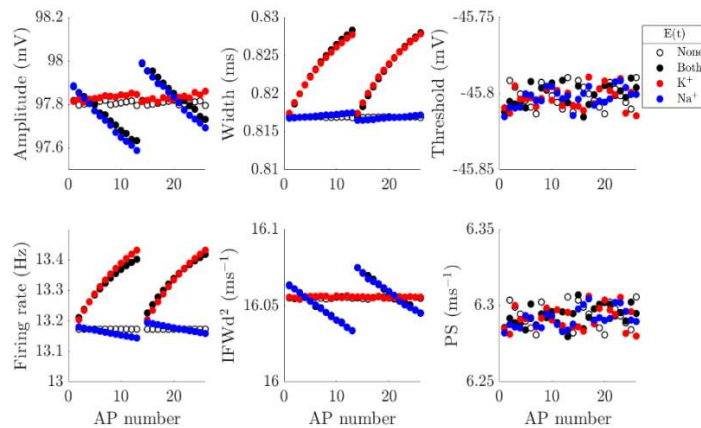


Figure D9: Effect of dynamical reversal potential on AP parameters (FS neuron model). The AP parameters are shown during two spike trains with no dynamical reversal potential (black circles), both channels have dynamical reversal potential (green circles), only K^+ channels have dynamical reversal potential (blue circles), or only Na^+ channels have dynamical reversal potential (red circles). The two current steps have the same magnitude and duration

(1s), with a 5s inter-sweep interval. The impact of concentration changes for each ion channel on the other channels is negligible ($>0.2\%$).

The combined effect of cooperativity and ion concentration on average AP parameters

Combining cooperativity and dynamical reversal potential did not alter the average AP parameter values compared to the classical model (Figure D10), and it has a small effect on a single spike train pattern with a weak current step (Figure D11). The change of rapidity values from declining to steep increase with coupling strength ($KJ=100-350\text{mV}$) is due to the change of the AP waveform from single to double \ddot{V} peaks. The opposite relationship between coupling strength and IFWd^2 will be reversed with a higher percentage of cooperative channels. A higher percentage of cooperative Na^+ produce APs with single \ddot{V} peaks. Therefore, the IFWd^2 increases with higher coupling strength in a similar pattern as the phase slope.

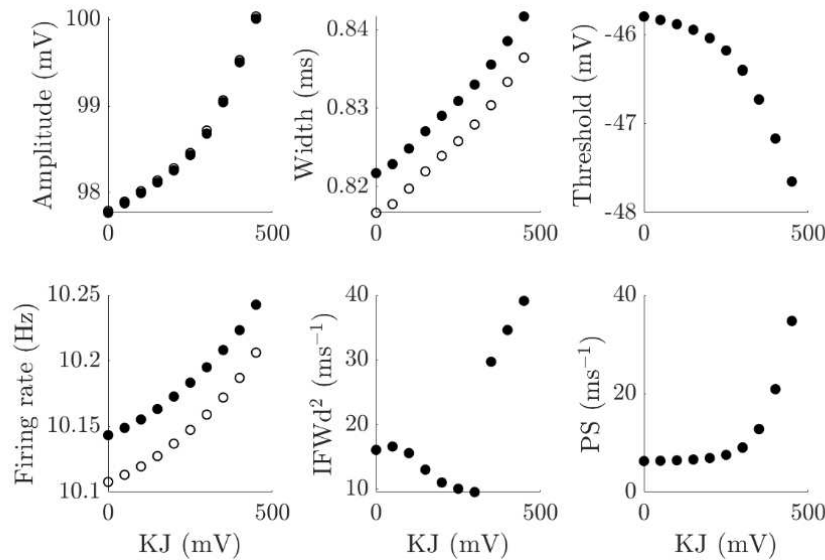


Figure D10: AP parameters in response to a 1s depolarizing current that evoke 10 APs ($p=10\%$). The hollow black circles represent the value from the original TM model, while the filled circles represent the results from the combined model with no cooperative channels.

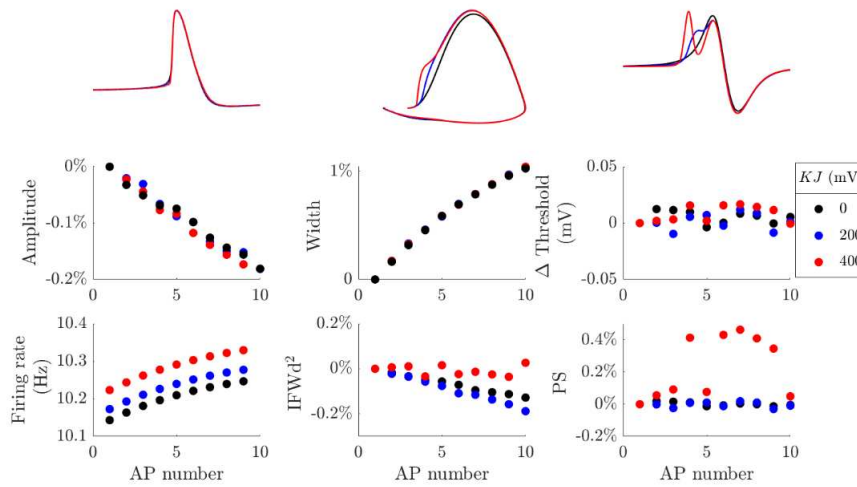


Figure D11: impact of different cooperativity strengths on AP parameters. The first row shows the time course of a single AP (left), the phase plot for the same APs (middle), and the second time derivative of the same AP (right). The second and third rows show the spike patterns with different coupling strengths. Black trace shows an AP without any cooperative Na⁺ channels. The blue and red trace shows an AP when 10% of Na channels activates cooperatively with 200 and 400 mV coupling strength.

The impact of cooperativity on the spike train pattern becomes apparent in response to strong stimuli, as opposed to the minimum current required to evoke a spike train. The percentage change in AP parameters during spike trains increases with a stronger current pulse. For example, the IFWd² rapidity decreases by 5.5% with strong cooperativity and 3 % without cooperativity (Figure D12). The reduction in rapidity is a coupled effect. While we showed above that changes in reversal potential during spike train lead to the change in AP parameter, cooperative Na gating increased that effect. Adding cooperativity ($p = 30\%$ and $KJ = 400$ mV) to the model led to an increase in the maximum E_{Na} change by 10%, causing a 6% increase in E_K maximum change. Thus, the firing rate increased indirectly in the presence of cooperative gating. Also, with a strong stimulus, the threshold shifted to a more depolarized value. The change in the threshold between the first and last AP increased by 0.15 mV. The results reflect the competing effect of the two mechanisms in the long timescale. While cooperativity was shown to shift the AP threshold to more hyperpolarized values, its effect on dynamical reversal potential competes against its main contributions. Cooperativity acts like positive feedback, whereas a change in concentration alters

reversal potential to act as negative feedback. Together, the two mechanisms provide a better agreement to experimental data.

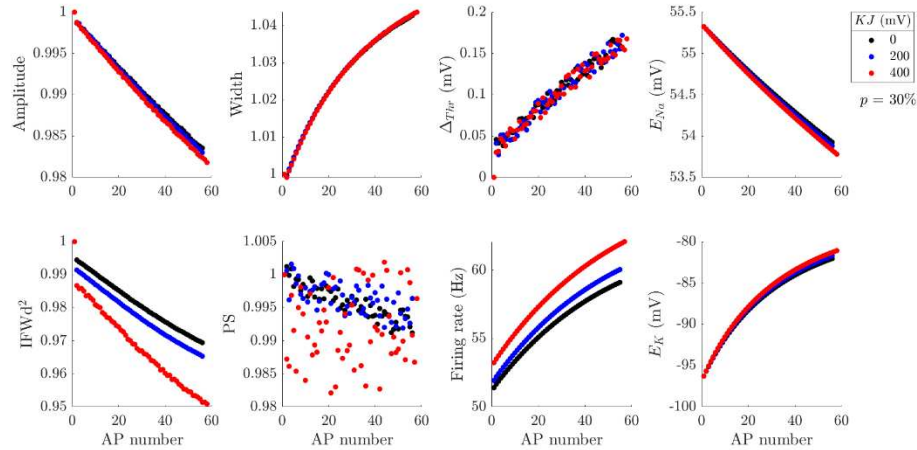


Figure D12: Impact coupling strength on AP parameters with strong stimuli and 30% of Na^+ channels activated cooperatively.

Changing the current pulse's magnitude or duration alters the spike train pattern. Here, we applied five current steps and varied the inter sweep interval between the pulses. With more than 5s inter sweep interval, the K^+ reversal potential reset to its steady potential before the next current pulse, but not Na^+ . Even with 10 s between the current pulses, E_{Na} increased by less than 0.7 mV, which is around the maximum change in E_{Na} resulting with the minimum applied current step. Therefore, increasing the current pulse causes a higher reduction in Na^+ concentration that will not be replenished before the following stimulus, which is reflected in the decrease of mean rapidity with each spike train. Including cooperative, Na^+ channels lead to more reduction in the rapidity and threshold potential and a slight increase in the first spikes in each spike train (Figure D13). The slight increase of first APs with strong cooperative gating is similar to the average increase observed in first APs in cortical neurons (Figure 5.4). In contrast, the first APs decrease with independent Na^+ channels (1.5% decrease Figure D14, black circles). Furthermore, even though cooperative gating had been shown to lower threshold potential to a more hyperpolarized value, it

kept the threshold potential of first spikes almost identical with dynamical reversal potential in response to strong stimuli but lower threshold with fixed reversal potential, compared to the first spike. Thus, the results show that two spike train features observed in experimental data are replicated only with the combined model.

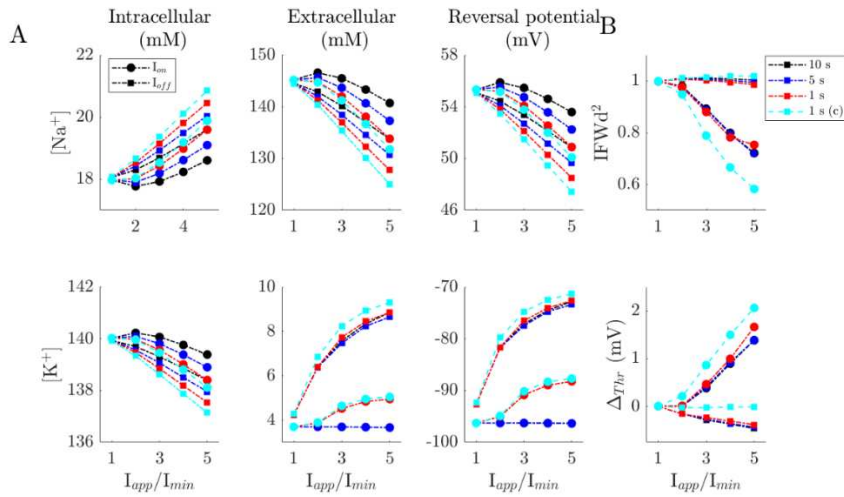


Figure D13: Impact of the current step amplitude and the time between consecutive current steps on ion concentration and AP parameters. A) shows the changes in intracellular concentration (left), extracellular concentration (middle), and reversal potential (right) for Na and K⁺ channels. Circles indicate the value at the beginning of the current pulse, while squares indicate the value at the end of the current pulse. The color of the symbols indicates the duration between the multiple-step current. All the values are obtained without cooperative gating except the values in cyan (KJ=400 mV, p =50%). B) The normalized rapidity and the threshold difference of the spike trains to the first spike. Squares indicate the value of the first spikes, and circles indicate the value of the last spike in each spike train.

Appendix E: MATLAB Codes

Here I describe how the electrophysiological recordings were obtained from public databases and provide the codes used in this dissertation. The three codes were for AP extraction and interpolation (used in chapters 3 and 4), AP attributes calculation (used in chapters 3-5), and the code for the model developed to replicate the APs' attribute variation (chapter 5).

Electrophysiological recordings were obtained from two databases. First, the recordings from the somatosensory cortex were obtained from the GigaScience database [78]. The recordings were stored as MATLAB files in the databases. The information about each file can be found in the excel sheet in da Silva Lantyer *et al* additional information [78], [148]. The excel sheet contains the date of the experiment, the scientist's initial, the mouse age and gender, the neuron classification, and other information for each experiment. The recording file name (Mat file) contains some of this information. For example, the MATLAB file named "161214_AL_113_CC" includes the current-clamp recording (CC) done by Angelica da Silva Lantyer (AL) on 16/12/2014 (the date in British format). This information is unique to this experiment, and extra information can be found in the excel sheet. Each MATLAB file (current clamp files) contains two types of recordings (current and voltage), and each variable contains two columns (time and current or voltage). The variable names provide the information for each recording. The variable name is in this format: Trace_ a_b_c_d, where *a* is the cell and experiment ID, *b* is the data type, *c* is the current step number, and *d* is either current (1) or voltage (2) trace. For example, Trace_ a_b_8_2 in the file named 161214_AL_113_CC is the voltage recording from the 8th current step.

Second, the recordings from hippocampal neurons were obtained from the CRCNS database [87]. The recordings can be found in the hippocampus section in a file named "hc10".

The file contains a PDF document describing the data such as cell type and an archive file containing the current clamp recordings. Each recording was stored as an ATF file, which can be opened using Microsoft Excel. Thus, the recordings can be easily transferred to MATLAB from excel. The first column contains the time steps, and the following columns contain the membrane potential in response to each current step.

Then, the raw data from the electrophysiological recordings will be sorted and analyzed.

The steps are:

1. Identify the voltage vectors that have at least two action potential
2. Store all voltage vectors with two or more APs in one variable for each individual neuron.

The first column should contain the AP train evoked by the minimum current step and the last column should contain the spike train evoked by the maximum current step. The vector was named “ V_r ” in the code.

3. Store the time vector in a variable named t .
4. Convert the units, if necessary, for membrane potential to mV and time to ms.
5. Save the voltage matrix and the time vector.
6. Load the file from step 5 into the AP extraction and interpolation code.
7. Specify the criteria for the AP selection (minimum AP peak height and minimum distance between peaks). Note that the minimum AP height is measured from the resting potential, usually between -80 and -65 mV. Thus, -20 mV or 0 mV minimum AP peak height is sufficient to detect the AP peak, but the choice of the minimum AP peak could differ between various recordings.
8. Specify the length of the AP trace (how many milliseconds before and after the peak).

9. Specify the interpolation method (*spline* or *pchip*) by commenting the undesirable method (see the code below).
10. Run the AP extraction code.
11. The output file contains three variables: AP traces (*Vsn*), the APs' first-time derivative (*dVsn*), and the APs' second-time derivative *d2Vsn*).
12. Check that each column has only one AP trace. If parts of other APs appear in a trace, reduce the length of the AP trace (step 8).
13. The output file is an input file for the AP analysis code, which calculates all the AP attributes (amplitude, width, threshold potential, and rapidity using four methods).

AP extraction and interpolation code

```

clc
% close all
load('C:\.mat'); % input file location
HH = length(Vr(1,:));
M1 = 1;
min_time_bwn_APs = 10; % min time separating two APs
t = (t-t(1));
tic
for JJ = 1:HH
V = Vr(:,JJ); % AP train
dt = t(2)-t(1); % time step (raw data) in ms
dt_spline = 1e-3; % time step (for interpolation) in ms
ts = 0:dt_spline:10; % ms
L = floor(5/dt); % specify the length of the AP trace
[pks,locs_V] =
findpeaks(V,'MinPeakHeight',0,'MinPeakDistance',round(min_time_bwn_APs/dt)); % find
the APs peaks index
N = length(pks); % number of APs
%% separate each AP (raw data)
for j=1:N
E(:,j) = V(locs_V(j)-L:locs_V(j)+L); % separate each AP by "L" ms before & after the peak
dE(:,j) = diff(E(:,j))./(2*dt); % Calc dV/dt for each AP
d2E(:,j) = diff(E(:,j),2)./(dt)^2; % Calc d^2V/dt^2 for each AP
end
te = t(1:length(E(:,1))); % time vector for E

```

```

tde = t(1:length(dE(:,1)));          % time vector for dE
td2e = t(1:length(d2E(:,1)));       % time vector for d2E
%% Interpolate each AP and its derivatives
% for pchip interpolation
for j=1:N
Vs(:,j)= spline(te,E(:,j),ts) ;      % spline fit for E
dVs(:,j) =spline(tde,dE(:,j),ts) ;   % spline fit for dE
d2Vs(:,j) = spline(td2e,d2E(:,j),ts); % spline fit for d2E
% for pchip interpolation uncomment the following lines and comment the
% spline lines
% Vs(:,j)= pchip(te,E(:,j),ts) ;     % spline fit for E
% dVs(:,j) =pchip(tde,dE(:,j),ts) ;  % spline fit for dE
% d2Vs(:,j) = pchip(td2e,d2E(:,j),ts); % spline fit for d2E
end
Ns = length(Vs(1,:));
Vsn(:,M1:M1+Nsn-1)=Vs;
dVsn(:,M1:M1+Nsn-1)=dVs;
d2Vsn(:,M1:M1+Nsn-1)=d2Vs;
M1 = M1+Nsn;
clearvars -except HH Vr tr t M1 M2 Vsn dVsn d2Vsn min_time_bwn_APs X Y clear_spike JJ
ts onset
end
filename ='C:\$\$.mat'; % Output file location
save(filename,'Vsn','dVsn','d2Vsn');

```

AP analysis code

```

clear
clc
load('C:\$.mat')
V = Vsn;
dV =dVsn;
d2V =d2Vsn;
dt = 1E-3;          % Time step
[M,N] = size(V);    % Number of spikes
[MV MVI] =max(V);   % Find the spike peak and index
T_max = M*dt -dt;   % Max time
ts = 0:dt:T_max;    % Time
CH = 0;
%% 1) Calculate FWHM & HWHM of d^2V/dt^2
% Set the limit of the rising phase of d^2V/dt^2
U_limit = MVI+round(2.5/dt); % Set upper limit to be 2.5 ms before spike peak
L_limit = MVI-round(2.5/dt); % Lower limit. 2.5 ms after the spike peak to
cover wide AP
[Min_d2V Min_d2V_IN] = min(d2V(L_limit:U_limit,:)); % find the index of min d2V
UL_d2V = L_limit + Min_d2V_IN;

```

```

[MAX MaxIndex]= max(d2V(L_limit:UL_d2V,:));           % Find the max d^2V/dt^2 within the
chosen limit
halfMax = MaxIndex/2;                               % Half the d^2V/dt^2 max value
Norm_d2Vs = (d2V(L_limit:U_limit,:)/MAX);           % Normalized d^2V/dt^2
T_norm = 0:dt:length(Norm_d2Vs)*dt - dt;           % Time corresponds to d^2V/dt^2 selected
portion
for j = 1:N
    for i=1:length(Norm_d2Vs)
        if(Norm_d2Vs(i,j)>= 0.5)&&(CH==0)
            t1st(1,j) = T_norm(i);                   % The time index of d^2V/dt^2 exceeds half Max
            CH = 1;
            M1(j) = Norm_d2Vs(i,j);
        end
        if(Norm_d2Vs(i,j)== 1)&&(CH==1)
            tmax(1,j) = T_norm(i);                   % The time index of d^2V/dt^2 reaches Max value
            CH = 2;
            MM(j) = Norm_d2Vs(i,j);
        end
        if(Norm_d2Vs(i,j)<= 0.5)&&(CH==2)
            t2nd(1,j) = T_norm(i);                   % The time index of d^2V/dt^2 drop below half Max
            CH = 3;
            M2(j) = Norm_d2Vs(i,j);
        end
    end
    end
    FW(j) = t2nd(1,j)-t1st(1,j);                     % FWHM
    HW(j) = tmax(1,j)-t1st(1,j);                     % HWHM
    CH = 0;
end
%% 2) Calculate the phase slope at a specific dV/dt value
% find phase slope at dV/dt = 10 mV/ms (following Naundorf, et al, P7)
targeted_dV = 10;                                    % The selected dV/dt value
for j= 1:N
    dV_index=find(dV(1000:end,j)>=targeted_dV,1,'first'); dV_index=dV_index+1000;
    slope(j) = (dV(dV_index+1,j)-dV(dV_index-1,j))/(V(dV_index+1,j)-V(dV_index-1,j));
    Thrshold_dV(j) = V(dV_index,j);
end
%% 3) Apply Volgushev method to calculate the error ratio
% I) Find dV/dt max value and the value at which dV/dt = 30% of the max value
[Max_dVs Max_index_dVs] = max(dV);
dVs_20 = Max_dVs*0.20;
dVs_30 = Max_dVs*0.30;
dVs_40 = Max_dVs*0.40;
% II) Fit the V trace from 5 ms to 0.1 ms from the peak with a continuous piecewise-linear
function
tic
for j = 1:N

```

```

i =1;
AP = V(MVI(j)-floor(5/dt):MVI(j)-floor(0.1/dt),j);      % The selected portion from - 5 ms to
0.1 ms back from AP peak
index_1st_pt(j) = MVI(j)-floor(5/dt);                  % The index of the first point of the selected
AP portion
APlen = length(AP);                                  % Length of the selected AP
t = (0:dt:(APlen-1)*dt)';                             % The time of the selected AP
MSE =[];
for bp = 2:APlen-1                                    % Find the breaking point at the min MSE
fit_low = polyfit(t(1:bp),AP(1:bp),1);                 % Fit the lower portion of the PL function
APfit_low =polyval(fit_low,t(1:bp));
fit_high = polyfix(t(bp+1:APlen),AP(bp+1:APlen),1,t(bp+1),APfit_low(bp)); % Fit the higher
portion of the PL function
APfit_high = polyval(fit_high,t(bp+1:APlen));
APfit_onset(1,1:bp) = APfit_low;
APfit_onset(1,bp+1:APlen) = APfit_high;
MSE(i) = immse(APfit_onset',AP);
i =i+1;
end
[MIN(j) Min_in(j)] =min(MSE);                          % Index of the minimum MSE represent the best
breaking point
onset(j) = AP(Min_in(j));                              % AP onset as defined by Volgushev et al (2008)
method
Min_in(j)=find(AP>=onset(j),1,'first');
index_onset_in(j) = index_1st_pt(j)+Min_in(j);        % Index of the AP onset
% III) Select the AP portion in the phase plot to be 5 ms before the AP
% onset to 30% of dV/dt max value
lower_limit(j) =index_onset_in(j)-floor(5/dt);      % Lower limit index
Upper_limit(j) = find(dV(:,j)>=dVs_30,1,'first');   % Upper limit index
end
% III) Fit the selected the AP portion to exponential and piecewise-linear function
tic
for j = 1:N
x = V(lower_limit(j):Upper_limit(j),j);           % Selected Vm
y = dV(lower_limit(j):Upper_limit(j),j);         % Selected dV/dt
%% MATLAB EXP function (exp1)
% use matlab fit function to provide a better intial guess for the exp function
% coffecients
Fit1 = fit(x,y,'exp1');
coeffvals1(j,:)=coeffvalues(Fit1);
APfit_exp = coeffvals1(j,1)*exp(coeffvals1(j,2)*x);
MSE_exp1(j) = immse(APfit_exp,y);
%% volgushev EXP function using the coffecient of exp1 as starting points
% exp function as described by volgushev paper was  $f(x) = a+\exp(b*(x+c))$ . We
% used the following as a starting guess for the function coffecients
a = y(1)-exp(coeffvals1(j,2)*x(1));

```

```

b = coeffvals1(j,2);
c = - x(1) + (log(abs(y(1)))-log(abs(a)))/coeffvals1(j,2) ;
fun1 = fittype('a+exp(b*(x+c))');
Fit2 = fit(x,y,fun1,'StartPoint',[a b c]);
coeffvals2(j,:)=coeffvalues(Fit2);
MSE_exp(j) = immse(Fit2(x),y); % Mean square error for the exp function
% if the MSE is large, redo the previous calculation use another starting
% guess from the previous trace
if(MSE_exp(j)>=2)&&(j>1)
    MMM(Q)= MSE_exp(j) ;
    III(Q) = j;
    Q = Q+1;
    a = coeffvals2(j-1,1);
    b = coeffvals2(j-1,2);
    c = coeffvals2(j-1,3);
    fun1 = fittype('a+exp(b*(x+c))');
    Fit2 = fit(x,y,fun1,'StartPoint',[a b c]);
    coeffvals2(j,:)=coeffvalues(Fit2);
    MSE_exp(j) = immse(Fit2(x),y);
end
%% Piecewise-linear function function
MSE_PL = [];
YL = length(y);
APfit_PL = zeros(1,YL);
i=1;
for bp = 2:YL-1 % Find the breaking point at the min MSE
    fit_lo = polyfit(x(1:bp),y(1:bp),1); % Fit the lower portion (the baseline)
    APfit_lo = polyval(fit_lo,x(1:bp));
    fit_hi =polyfix(x(bp+1:YL),y(bp+1:YL),1,x(bp+1),APfit_lo(bp));
    APfit_hi = polyval(fit_hi,x(bp+1:YL)); % Fit the upper portion (the vertical rise)
    APfit_PL(1,1:bp)=APfit_lo;
    APfit_PL(1,bp+1:end)= APfit_hi;
    MSE_PL(i) = immse(APfit_PL',y);
    i=i+1;
end
[MIN_PL(j) Min_PL_in(j)] =min(MSE_PL(:)); % Find the index of the min MSE_PL
ERR(j) = MSE_exp(j)./MIN_PL(j); % calc the error ratio
onset2(j) = x(Min_PL_in(j)); % the potential at the breaking point of the PL function
end
%% 4) Calculate the spikes width and amplitude
for j= 1:N
    E = (V(:,j)-Thrshold_dV(j)); % AP trace from the threshold potential
    AP_Amplitude(j) = max(E); % The AP amplitude
    HV = 0.5*max(E); % Half the AP amplitude
    for i = 1:length(E)
        if(E(i)>=HV)&&(CH==0)

```

```

    T1 = ts(i);
    CH = 1;
elseif(E(i)<=HV)&&(CH==1)
    T2 = ts(i);
    CH = 2;
end
end
AP_Width(j)= T2-T1;           % The AP width
CH = 0;
end
elapsedTime2 = toc;
% save the results. Change the variable names to match the neuron label
filename = 'C:\AP_parameters_S104';
FW_S104 = 1./FW;           % IFWd2 rapidity
HW_S104 = 1./HW;           % IHWd2 rapidity
slope_S104 = slope;        % phase slope rapidity
ERR_S104 = ERR;           % error ratio rapidity
MSE_exp_S104 = MSE_exp;
MSE_PL_S104 = MIN_PL;
AP_width_S104 = AP_Width;
AP_Amplitude_S104 = AP_Amplitude;
onset_S104 =onset;         % threshold potential as defined by Volgushev et al (2008)
onset2_S104 =onset2;      % threshold potential as defined by the breaking point of the PL
function in the phase plot
onset_dV_S104 = Thrshold_dV; % threshold potential as defined by Naundorf et al (2006)
save(filename,'ERR_S104','MSE_exp_S104','MSE_PL_S104','FW_S104','HW_S104','slope_S10
4','AP_width_S104','AP_Amplitude_S104','onset_S104','onset2_S104','onset_dV_S104');

```

The combined model code

```

clear
clc
tic
%% %% (c)2021, Ahmed Aldohbeyb & Kvein Lear (10/7/2021)
%% %%
% A single-compartment HH-type model that combining the effect of cooperative
% Na+ channels and dynamical reversal potential, which we called the
% Combined Model. The model is based on Pospischil et al (2008) paper, which
% described different type of neurons and their VGICs. The dynamical reversal potential was
% adopted from Cressman et al (2009I) full model and cooperative Na+ channels
% were used as described in Huang et al (2012) model.
% Note that some of the parameters was based on Cressman et al(2009) published
% model in ModelDB where several corrections was made in order to accurately
% reproduce their results.
%% cell type as described in Pospischil et al (2008):

```

```

% 1) regular-spiking (RS) excitatory (pyramidal) neuron & inhibitory neuron
% 2) fast-spiking (FS) neuron,
% Note: changing some the parameters such as g, VT, or tau can reproduce the response of
different cells that fall
% under the same categorize. for example, depending on the choise of Na, Kd, Ks, and leak
channels
% parameters, you can get the response from a RS excitatory or RS inhibitory cell.
% So, this code can reproduce some of the figures in Pospischil et al
% (2008) paper by choosing the cell type and setting dyn_con = 0 & KJ or p = 0.
% for example: to reproduce figure 2A in Pospischil et al (2008), set
% dyn_con =0; type = 1; p=0;KJ=0;
%% neuron types
% 1: RS (exc (PC)) based on somatosensory cortex in vitro fig.2a in Pospischil et al (2008),
% 2: RS(inh), based on somatosensory cortex in vitro fig.2b in Pospischil et al (2008),
% 3: FS (inh), based on ferret visual cortex in vitro Fig.3 in Pospischil et al (2008),
% 4: FS (inh), based on somatosensory cortex in vitro Fig.4 in Pospischil et al (2008),
% model parameter for each cell type. Each coulum represent a neuron type and
% the rows represent the model parameters as following: 1)Na+ conductance,
% 2)g_Kd conductance, 3) g_Ks conductance, 4) g_leak conductance 5) E_leak,
% 6) VT 7)time const. for g_Ks, 8) model dimension in
% um (L = d). Units: conductance (mS/cm2), potential (mV), time (ms), and
% length and depth in um.
tic
% dyn_cond = 1 : dynamical reversal potential & 0 : steady-state value (fixed)
dyn_cond = 1;
type = 3;
para = [56 10 50 58;6 2.1 10 3.9;7.5E-2 9.8E-2 0 7.87E-2;...
        2.05E-2 1.33E-2 1.5E-1 3.8E-2;-70.3 -65 -70 -70.4; ...
        -56.2 -67.9 -63 -57.9;608 934 4000 502;61.4 61.8 67 56.9];
KJa = 0;
pa = 0.0; % vector for fraction of coop. chs' (%)
for W = 1:length(pa)
    p = pa(W); % percentage of coop. Na+ channels
for Q = 1:length(KJa)
    KJ = KJa(Q); % coupling strength (mV);
%% Parameters
dt = 1E-3; % time step (ms)
T_max = 20E3; % max time (ms)
t = 0:dt:T_max; % time vector (ms)
N = length(t); % number of steps
A = (para(8,type)*1e-4)^2; % Area para(10,type) is in um, so x1E-4 to have
A in cm^2
C = A*1; % Membrane capacitance (1 uF/cm^2)
gNa = para(1,type); % Na+ max conductance (mS/cm^2)
gKd = para(2,type); % K+ (delayed-rectifier) max conductance
(mS/cm^2)

```

```

gKs = para(3,type); % K+ (Slow) max conductance (mS/cm^2)
gL = para(4,type); % Leak max conductance (mS/cm^2)
EL = para(5,type); % Leak reversal potential (mV)
VT = para(6,type); % Variable to adjust spike threshold
tau_nsMax = para(7,type); % maximum time const. for slow K+ ch's
deg = 34.1; % °C
V_thermal = 1000*(deg + 273)*(1.38E-23/1.6E-19); % Thermal voltage
B = 7; % Ratio of intracellular to extracellular volume of the cell
Ps = 10*1.125 ; % Pump strength (mM/ms)
G_glia = 200/3; % Strength of glial uptake (mM/ms)
epsilonK = 4.0/3.0; % Diffusion constant (1/ms)
kbath = 4.0; % Steady state extracellular potassium concentration (mM)
gamma = 0.044495; % factor to convert current density to d[conc]/dt (mM.cm2/?coul)
tau = 1000; % to convert mM/s to mM/ms
Na_i = zeros(1,N); Na_o = zeros(1,N); % preallocate vectors for ion concentration
K_i = zeros(1,N); K_o = zeros(1,N);
Na_i(1) = 18.0; % Initial intracellular Na+ conc at the channels (mM)
% Na_p = Na_i; % Initial intracellular Na+ conc at the pump (mM)
Na_o(1) = 145; % Initial extracellular Na+ conc (mM)
K_i(1) = 140 ; % Initial intracellular K+ conc (mM)
K_o(1) = 3.7; % Initial extracellular K+ conc (mM)
kna = 87.5; % Na+ dissociation constant (mM)
kca = 1.38; % Ca2+ dissociation constant (mM)
ksat = 0.1; % the saturation factor
GM = 0.35; % voltage dependence factor
q10 = 3^((deg - 37)/10);
% D_Na = 3e-6;
% delta_X = 1E-4;
% epsilonNa = 2*D_Na./(delta_X)^2;
ENa = zeros(1,N); % preallocate vectors for reversal potential
EK = zeros(1,N);
ENa(1) = V_thermal*log(Na_o(1)/Na_i(1)); % Initial Na+ reversal potential (mV)
EK(1) = V_thermal*log(K_o(1)/K_i(1)); % Initial K+ reversal potential (mV)
%% Initial Conditions
V = zeros(1,N); % preallocate vectors for Vm and gating variables
Vcoop = V; m = V;
mc = V; h = V;
n = V; ns = V;
V(1) = EL; % initial membrane potential
m(1) = alphaM(V(1),VT)/(alphaM(V(1),VT) + betaM(V(1),VT)); % independent Na+ channels activation
mc(1) = m(1); % cooperative Na+ channels activation
h(1) = alphaH(V(1),VT)/(alphaH(V(1),VT) + betaH(V(1),VT)); % Na+ channels inactivation

```

```

n(1) = alphaN(V(1),VT)/(alphaN(V(1),VT) + betaN(V(1),VT)); % K+ (delayed-rectifier)
channels activation
ns(1) = Ns_inf(V(1)); % K+ (slow) channels activation
INai = zeros(1,N);INac = INai;INa = INai; % preallocate vectors for ch's current
IKd = zeros(1,N);IKs = IKd;IK = IKd;
ILeak = zeros(1,N);Ipump=ILeak;Iglia=ILeak;IKdiff =ILeak;
%% current pulse & synaptic parameters
I = 0; % Vector for current pulse
I_app = 0;
PL_T = round(1000/dt); % length of the current pulse
T_bw_pulses = round(5000/dt); % Time between current pulses
I_on = round(1000/dt); % on time for 1st current pulse
I_off = I_on + PL_T; % off time for 1st current pulse
I_on2 = I_off + T_bw_pulses; % on time for 2nd current pulse
I_off2 = I_on2 + PL_T; % off time for 2nd current pulse
I_on3 = I_off2 + T_bw_pulses; % on time for 3rd current pulse
I_off3 = I_on3 + PL_T; % off time for 3rd current pulse
I_on4 = I_off3 + T_bw_pulses; % on time for 4th current pulse
I_off4 = I_on4 + PL_T; % off time for 4th current pulse
I_on5 = I_off4 + T_bw_pulses; % on time for 4th current pulse
I_off5 = I_on5 + PL_T; % off time for 4th current pulse
%% the main loop
for i = 1:N-1
%% Current through each voltage-gated ion channels & Membrane potential
INai(i) = (1-p)*gNa*m(i)*h(i)*(ENa(i) - V(i)); % Independent Na+ channels
current
INac(i) = p*gNa*mc(i)*h(i)*(ENa(i) - V(i)); % Cooperative Na+ channels
current
INa(i) = INai(i) + INac(i); % total Na+ current
IKd(i) = gKd*n(i)^4*(EK(i) - V(i)); % delayed-rectifier K+ current
IKs(i) = gKs*ns(i)*(EK(i) - V(i)); % slow non-inactivating K+ current
IK(i) = IKd(i) + IKs(i); % total K+ current
ILeak(i) = gL*(EL-V(i)); % leak channel current
% membrane potential (4RK method)
Vrk(1) = (dt/C)*A*(INa(i) + IK(i) + ILeak(i) + I);
kV = V(i) + Vrk(1)/2;
Vrk(2) = 0.5*(dt/C)*A*((1-p)*gNa*m(i)*h(i)*(ENa(i) - kV) + p*gNa*mc(i)*h(i)*(ENa(i) -
kV)...
+ gKd*n(i)^4*(EK(i) - kV)+ gKs*ns(i)*(EK(i) - kV) + gL*(EL-kV) + I);
kV = V(i) + Vrk(2)/2;
Vrk(3) = 0.5*(dt/C)*A*((1-p)*gNa*m(i)*h(i)*(ENa(i) - kV) + p*gNa*mc(i)*h(i)*(ENa(i) -
kV)...
+ gKd*n(i)^4*(EK(i) - kV)+ gKs*ns(i)*(EK(i) - kV) + gL*(EL-kV) + I);
kV = V(i) + Vrk(3);
Vrk(4) = (dt/C)*A*((1-p)*gNa*m(i)*h(i)*(ENa(i) - kV) + p*gNa*mc(i)*h(i)*(ENa(i) - kV)...
+ gKd*n(i)^4*(EK(i) - kV)+ gKs*ns(i)*(EK(i) - kV) + gL*(EL-kV) + I);

```

```

V(i+1) = V(i) + (Vrk(1) + 2*Vrk(2) + 2*Vrk(3) + Vrk(4))/6;
%% Conc. & Reversal potential (Dynamical (dyn_con = 1) or Fixed (dyn_con = 0))
if(dyn_cond == 0) % For fixed reversal potential use conc. SS value
ENa(i+1) = V_thermal*log(Na_o(1)/Na_i(1));
EK(i+1) = V_thermal*log(K_o(1)/K_i(1));
else % For dynamical reversal potential
ENa(i+1) = V_thermal*log(Na_o(i)/Na_i(i)); % Na+ reversal potential (mV)
EK(i+1) = V_thermal*log(K_o(i)/K_i(i)); % K+ reversal potential (mV)
Ippump(i) = (Ps/(1.0+exp((25.0-Na_i(i))/3.0)))*(1/(1+exp(5.5-K_o(i)))); % Na+/K+ pump
(mM/s)
Iglia(i) = G_glia/(1.0+exp((18.0-K_o(i))/2.5)); % glial capacity to remove
excess K+ from the extracellular space (mM/s)
IKdiff(i) = epsilonK*(K_o(i)-kbath); % diffusion of potassium away
from the local extracellular micro-environment (mM/s)
% INadiff(i) = epsilonNa*(Na_i(i)-Na_p(i)); % diffusion of Na from the
channels to the Na/K pump
Na_o(i+1) = 145 - B*(Na_i(i)-Na_o(1)); % Extracellular Na+
concentration (mM)
K_i(i+1) = 140 +(Na_o(1) - Na_i(i)); % Intracellular K+ concentration
(mM)
% 4RK for [Na+]i & [K+]o
% Intial values
INa0 = INa(i);
Iglia0 = Iglia(i);
IKdiff0 = IKdiff(i);
% INadiff0 = INadiff(i);
IK0 = IK(i);
INaK = Ippump(i);
dt0=dt;
for j = 1:4 % Calculate the 4 RK coefficients for each ion species
k_K(j)= dt0*(-gamma*B*IK0 - 2*B*INaK -Iglia0-IKdiff0)/tau;
k_Na(j) = dt0*(gamma*INa0-3*INaK)/tau;
% k_Nap(j) = dt0*(-3*INaK + INadiff0)/tau;
if(j==3) % for the fourth coefficients, the values are multiplied by 1
Na_i0 = Na_i(i) + k_Na(j);
% Na_p0 = Na_p(i) + k_Nap(j);
K_o0 = K_o(i) + k_K(j);
dt0 = dt;
else
Na_i0 = Na_i(i) + k_Na(j)/2;
% Na_p0 = Na_p(i) + k_Nap(j)/2;
K_o0 = K_o(i) + k_K(j)/2;
dt0 = dt/2;
end
ENa0 = V_thermal*log(Na_o(i)/Na_i0);
INa0 = (1-p)*gNa*m(i)*h(i)*(ENa0 - V(i)) + p*gNa*mc(i)*h(i)*(ENa0 - V(i));

```

```

EK0 = V_thermal*log(K_o0./K_i(i));
Iglia0 = G_glia/(1.0+exp((18.0-K_o0)/2.5));
IKdiff0 = epsilonK*(K_o0-kbath);
% INadiff(i) = epsilonNa*(Na_i0-Na_p0);
IK0 = gKd*n(i)^4*(EK0 - V(i)) + gKs*ns(i)*(EK0 - V(i));
INaK = (Ps/(1.0+exp((25.0-Na_i0)/3.0)))*(1/(1+exp(5.5-K_o0)));
end
K_o(i+1)=K_o(i) + (k_K(1) + 2*k_K(2) +2*k_K(3) +k_K(4))/6;           % Extracellular K+
concentration (mM)
Na_i(i+1)=Na_i(i) + (k_Na(1) + 2*k_Na(2) +2*k_Na(3) +k_Na(4))/6;     % Intracellular Na+
concentration (mM)
% Na_p(i+1)=Na_p(i) + (k_Nap(1) + 2*k_Nap(2) +2*k_Nap(3) +k_Nap(4))/6;   % Na+
concentration at the pump(mM)
end
%% gating variables (4RK method for differential eq's)
Vcoop(i) = V(i) + KJ*mc(i)*h(i);           % V for Na+ cooperative channels
% Na+ gating variables
mc_inf = alphaM(Vcoop(i),VT)/(betaM(Vcoop(i),VT) + alphaM(Vcoop(i),VT));
tau_mc = 1/(alphaM(Vcoop(i),VT)+betaM(Vcoop(i),VT));
mc(i+1) = mc_inf^3 + (mc(i)-mc_inf^3)*exp(-dt/tau_mc);
m_inf = alphaM(V(i),VT)/(betaM(V(i),VT) + alphaM(V(i),VT));
tau_m = 1/(alphaM(V(i),VT)+betaM(V(i),VT));
m(i+1) = m_inf^3 + (m(i)-m_inf^3)*exp(-dt/tau_m);
fh = @(h0,V,dt) dt*(0.128*exp(-(V-VT-17)/18)*(1-h0) - h0*4./(exp(-(V-VT-40)/5)+1));
h(i+1) = RK4_function(fh,dt,h(i),V(i));
% K+ gating variables
fn = @(n0,V,dt) dt*(-0.032*(V-VT-15)/(exp(-(V-VT-15)/5) - 1)*(1-n0) - n0*0.5*exp(-(V-VT-
10)/40));
n(i+1) = RK4_function(fn,dt,n(i),V(i));
fns = @(ns0,V,dt) dt*((1/(1+exp(-(V+35)/10))) - ns0)/(tau_nsMax/(3.3*(exp((V+35)/20)) +
exp(-(V+35)/20)));
ns(i+1) = RK4_function(fns,dt,ns(i),V(i));
if (i>I_on)&&(i<I_off)           % 1st pulse
    I = I_app;
elseif(i>I_on2)&&(i<I_off2)     % 2nd pulse
    I = 1.5*I_app;
elseif(i>I_on3)&&(i<I_off3)     % 3rd pulse
    I = 2*I_app;
elseif(i>=I_on4)&&(i<I_off4)    % 4th pulse
    I = 2.5*I_app;
elseif(i>=I_on5)&&(i<I_off5)    % 4th pulse
    I = 3*I_app;
else
    I = 0;
end
end

```

```

% check if V(i) becomes a complex number & break if it is a complex number or V> or < +- 300
mV
tf = isreal(V(i));
if(tf == 0) || (abs(V(i))>300)
mass = [' Error occured. V = ',num2str(round(V(i))),' mV at t = ',num2str(t(i)),' ms'];
disp(mass)
break
end
end
[pkcs,locs_V] = findpeaks(V,'MinPeakHeight',0,'MinPeakDistance',50); % APs peaks index
%% APs' parametes
ISI = t(locs_V(2:end)-locs_V(1:end-1)); % Intracellular-spike interval in
ms(ISI). in case of multiple pulses ignore the first value after the first pulse
N = length(pkcs); % number of APs
r =zeros(1,length(V)); % vector for spike time
r(locs_V)=1; % 1 for each spike, zero elsewhere
AP_t_HW = round(4/dt); % the number of data points selected
before and after each AP peak
tVs = t(1:2*AP_t_HW +1); % time vector for the selected AP
(ms)
t_d2Vs = t(1:2*AP_t_HW -1); % time vector to calc IFWd^2
c_level1 = 25; % criterion level 1 : for phase slope and
threshold (mV)
c_level2 = 70; % criterion level 2 : to calc slope between
c_level 1 & 2(mV)
for i = 1:N
Vs = V(locs_V(i)-AP_t_HW:locs_V(i)+AP_t_HW); % separete each AP
dVs = diff(Vs)/dt; % AP 1st derivative
d2Vs = diff(Vs,2)/(dt*dt); % AP 2nd derivative
FW(i) = 1./fwhm(t_d2Vs,d2Vs); % rapidity using IFWd^2 method
(1/ms). Fwhm calc using Patrick Egan (2022). fwhm
%(https://www.mathworks.com/matlabcentral/fileexchange/10590-fwhm)
PS_i = find(dVs>= c_level1,1,'first'); % find the index of criterion_level
PS(i) = (dVs(PS_i+1)-dVs(PS_i-1))/(Vs(PS_i+1)-Vs(PS_i-1)); % AP rapidity using the
phase slope (1/ms)
Thr(i) = Vs(PS_i); % AP threshold (mV)
AP_h(i) = max(Vs)-Thr(i); % AP Amplitude from thrshold to
peak (mV)
AP_w(i) = fwhm(tVs,Vs-Thr(i)); % AP width at half the amplitude
(ms)
t_thr(i) = tVs(PS_i); % time of Thrshold
PS_ic = find(dVs>= c_level2,1,'first'); % find the index when dVcoop/dt
>= criterion level
PSc(i) = (dVs(PS_ic+1)-dVs(PS_ic-1))/(Vs(PS_ic+1)-Vs(PS_ic-1)); % VNa rapidity
using the phase slope (1/ms)

```

```

    Ss(i,:) = polyfit(Vs(PS_i:PS_ic),dVs(PS_i:PS_ic),1);           % slope of a line between
criterion_level 1 & 2
    Thrc(i) = Vs(PS_ic);                                         % AP threshold at c_level2(mV)
end
%% mean AP parameters
onset(W,Q) = mean(Thr);                                         % mean onset potential at 1st criterion level (mV)
onset2(W,Q) = mean(Thrc);                                       % mean onset potential at at 2nd criterion level (mV)
SD_1(W,Q) = std(Thr);
SD_2(W,Q) = std(Thrc);
slope(W,Q) = mean(PS);                                         % mean rapidity using phase slope (point) method at 1st
criterion level (ms^-1)
slope2(W,Q) = mean(Ss(:,1));                                     % mean rapidity using phase slope (line)method bwn 1st
& 2nd criterion level (ms^-1)
IFWd(W,Q) = mean(FW);                                         % mean rapidity using the inverse of the full-width
method at half max (ms^-1)
width(W,Q) = mean(AP_w);                                       % mean AP width (ms)
amplitude(W,Q) = mean(AP_h);                                    % mean AP amplitude (mV)
Thr_var(W,Q)=max(Thr)-min(Thr);                                % onset variability (mV), which is the difference
between the max and min onset value as defined by Naundorf et al (2006)
num(W,Q) = N                                                   % AP number
ISIt(W,Q) = 1/(mean(ISI)/1000);                                % mean ISI (ms)
ENa_d(W,Q) = ENa(I_on)-ENa(I_off);                             % Na+ reversal potential difference bwn the
begining and the end of injected current pulse
EK_d(W,Q) = EK(I_on)-EK(I_off);                                % K+ reversal potential difference bwn the beginig
and the end of injected current pulse
clearvars -except para type dyn_cond pa KJa W Q tic p onset slope onset2 slope2 Thr_var...
    ENa_d EK_d Vec_str IFWd width amplitude Time_diff num Threshold_diff ISIt
end
end
time = toc/60;                                                 % Simulation time in minutes
%% rate functions
% alpha
function aM = alphaM(V,VT)
aM = -0.32*(V-VT-13)/(exp(-(V-VT-13)/4) - 1);
end
function aH = alphaH(V,VT)
aH = 0.128*exp(-(V-VT-17)/18);
end
function aN = alphaN(V,VT)
aN = -0.032*(V-VT-15)/(exp(-(V-VT-15)/5) - 1);
end
% beta
function bM = betaM(V,VT)
bM = 0.28*(V-VT-40)/(exp((V-VT-40)/5) - 1);
end
function bH = betaH(V,VT)

```

```

bH = 4./(exp(-(V-VT-40)/5)+1);
end
function bN = betaN(V,VT)
bN = 0.5*exp(-(V-VT-10)/40);
end
function Ns_i = Ns_inf(V)
Ns_i= 1/(1+exp(-(V+35)/10));
end
function tns_i = tau_ns(V,tau_nsMax)
tns_i= tau_nsMax/(3.3*(exp((V+35)/20)) + exp(-(V+35)/20));
end
%% 4th RK for channels variables
function RK4g= RK4_function(f,dt,a0,V)
dt0 =dt;
m1 = a0;
for j = 1:3
    k(j) = f(m1,V,dt0);
    m1 = a0 + k(j)/2;
    dt0 = dt/2;
end
m1 = a0 + k(j);
dt0 = dt;
k(4) = f(m1,V,dt0);

RK4g = a0 + (k(1) + 2*k(2) +2*k(3) +k(4))/6;
end

```

Appendix F: Numerical analysis and data source

Numerical analysis is an area of mathematics that provides algorithms to solve difficult problems using approximate solutions. One of the main advantages of numerical analysis is to convert real-world problems such as heat transfer or wave equation to an accurate numerical approximation that can be solved using a computer. The choice between many numerical methods to solve a particular problem depend on trade-off between accuracy, stability, and computation time. Thus, the type of the problem and required accuracy must be determined before choosing and implementing the numerical methods.

A description of the two methods used in this dissertation is shown below. The two methods are the Forward Euler (FE) method, and the fourth order Runge-Kutta (4RK) method. The FE method is a finite difference formula derived from a Taylor series expansion. For example, the approximation for a function of space, $f(x_i)$, at the next point (x_{i+1}) is:

$$f(x_{i+1}) = f(x) + (x_{i+1} - x_i)f'(x_i) + \frac{(x_{i+1} - x_i)^2}{2!}f''(x_i) + \dots$$

Assuming a fixed space step $\Delta x = (x_{i+1} - x_i)$ and rearranging the equation leads to the approximation of the function first derivative:

$$f'(x_i) = \frac{f(x_{i+1}) - f(x)}{\Delta x} + \frac{\Delta x^2}{2!}f''(x_i) + \dots$$

This method is called the Forward Euler since the derivative at certain point is determined by the value of the function at that position and the next position. The accuracy of the method is determined by the exponent of the leading form, which is $\frac{\Delta x^2}{2}f''(x_i)$. In general, the accuracy of the method with a leading term Δx^j is on the order of $j - 1$. Thus, the FE method is a first-order

accuracy scheme. A first-order scheme means if the step size is reduced by a factor of 10, the error will be also reduced by a factor 10. Thus, the choice of a reasonable step size is crucial for obtaining accurate results.

Furthermore, the same steps can be applied to the HH model. The HH model is represented as the following:

$$C \frac{dV}{dt} = I_{Na^+} + I_{K^+} + I_{leak} + I_{app}$$

Approximating the derivative using the FE method and rearranging the equation yields the following numerical scheme:

$$C \frac{V(t+1) - V(t)}{\Delta t} = I_{Na^+} + I_{K^+} + I_{leak} + I_{app}$$

$$V(t+1) = V(t) + \frac{\Delta t}{C} (I_{Na^+} + I_{K^+} + I_{leak} + I_{app})$$

This numerical scheme can produce very accurate results for the HH model, given a small-time step (Δt). One of the main advantages of the FE methods is that the numerical scheme is easy to implement and has a low computation cost. However, the low accuracy and limited stability of the method can be problematic when the model is modified to include another mechanism such as ion concentration, which increase the complexity of the model. Thus, a significant reduction in the time step is required to maintain the accuracy and stability of the results. However, with smaller Δt , the computation time will significantly increase, losing one of the main advantages of the FE method. Thus, the model should be solved using a more advanced numerical method.

The 4RK method is one of the widely used numerical schemes to obtain approximate solutions. The method includes the same steps as the Euler methods but adding intermediate points between x_i and x_{i+1} . The 4RK method uses four points (steps) to obtain the solution at the next step. For example, let assume that the initial value of the membrane potential $V(t_0)$ is V_0 . Solving

the HH model for next time step require 4 steps in the 4RK method. The first step of the 4RK method (k_1) is obtained using the initial condition and a fixed step size (Δt):

$$\frac{dV}{dt} = f(V, t)$$

$$k_1 = \Delta t f(V_0, t_0)$$

Now each step (k_i) in the 4RK method is based on the previous step (k_{i-1}). Therefore, the other points and final solution are as follows:

$$k_2 = \Delta t f\left(V_0 + \frac{1}{2}k_1, t_0 + \frac{\Delta t}{2}\right)$$

$$k_3 = \Delta t f\left(V_0 + \frac{1}{2}k_2, t_0 + \frac{\Delta t}{2}\right)$$

$$k_4 = \Delta t f(V_0 + k_3, t_0 + \Delta t)$$

$$V(t + 1) = V(t) + \frac{1}{6}(k_1 + 2k_2 + 2k_3 + k_4)$$

As can be seen by the multiple steps to obtain the next point solution, the 4RK method requires more computation time per step than the FE method. However, the 4RK method is fourth order accurate scheme and has a higher stability limit compared to the FE method. Also, it can provide a stable solution with a bigger time step, compared to the FE method. Therefore, the 4RK method is widely used with more complex models. For a further explanation on numerical analysis, see Parviz Moin book “Fundamentals of Engineering Numerical Analysis” [149].

Electrophysiological recordings sources

The following table shows a description of several databases for electrophysiological recordings.

Table F1: Electrophysiological recording and information databases

Database	Description
Allen Brain map (Link)	Intracellular recordings from different brain regions. The data are from normal or diseased human and mouse.
GIGADB (Link)	Data repository supporting scientific publications in the Life/Biomedical Sciences domain (cortical neurons recording was obtained from this database)
CRCNS (Link)	Intracellular and extracellular recordings from different brain regions, as well as shared stimuli and analysis tools. (hippocampal neurons recording was obtained from this database)
FigShare (Link)	A repository where many studies share their research results or tools available.
ModelDB (Link)	Database for computational neuroscience models
NeuroElectro (Link)	A Project to extract information about the electrophysiological properties from the literature